Protein interaction with polyelectrolytes and ligands: A structural and thermodynamic investigation

Dissertation
zur Erlangung des akademischen Grades

doctor rerum naturalium
(Dr. rer. nat.)

im Fach Physik

eingereicht an der
Mathematisch-Naturwissenschaftlichen Fakultät
der Humboldt-Universität zu Berlin

von
M.Sc. Physik Shun Yu

Präsidentin der Humboldt-Universität zu Berlin
Prof. Dr.-Ing. Dr. Sabine Kunst

Dekan der Mathematisch-Naturwissenschaftlichen Fakultät
Prof. Dr. Elmar Kulke

Gutachter:
1. Prof. Dr. Matthias Ballauff
2. Prof. Dr. Jürgen Rabe
3. Prof. Dr. Michael Gradzielski

eingereicht am: 07.03.2017

Tag der mündlichen Prüfung: 24.07.2017

... Daß ich erkenne, was die Welt
Im Innersten zusammenhält, ...

Faust, Goethe

List of publications

This thesis contains work from the following original papers and preprint:

Paper I: S. Yu, X. Xu, C. Yigit, M. v. Giet, W. Zidek, J. Jankowski, J. Dzubiella, M. Ballauff, "Interaction of human serum albumin with short polyelectrolytes: a study by calorimetry and computer simulations", *Soft Matter* (2015), **11**, pp. 4630-4639; published by RSC with open access license CC-BY

Paper II: S. Yu, M. Schuchardt, M. Tölle, M. v. Giet, W. Zidek, J. Dzubiella, M. Ballauff, „Interaction of human serum albumin with uremic toxins: A thermodynamic study", *RSC Advances* (2017), **7**, pp. 27913-27922; published by RSC with open access license CC-BY

Author's contributions to the joint paper and submitted paper:

Paper I: I performed all experiments carried out by ITC in this study including analysis and interpretation of these data. The computer simulations and theoretical considerations were conducted by X. Xu, he and Prof. Dzubiella contributed to the discussion and revision of the paper. Our collaborators M. v. Giet, W. Zidek and J. Jankowski contributed to the discussion and revision of the paper. This research study was supervised by Prof. Ballauff and Prof. Dzubiella.

Paper II: I performed all ITC measurements in this research including the data analysis and interpretation of the results. Prof. Dzubiella contributed to the theoretical considerations in the section "Influence of ionic strength on binding" of this paper. Our collaborators M. Schuchardt, M. Tölle, M. v. Giet and W. Zidek contributed to the discussion and revision of the paper. This research study was supervised by Prof. Ballauff.

Abstract

Understanding the interaction of proteins with charged molecules is of great importance in a wide field of health-related research topics. [1, 2] Nanoparticles coated with polyelectrolytes, interact with proteins once immersed in the human blood stream. A so called protein corona is formed and will modify the physical and chemical properties of nanoparticles, determining its path through the organism. [3] In the case of small, charged molecules, the uptake of toxins by proteins have a major influence on the efficiency of drugs on the one hand, and can hinder the proteins in their function, on the other hand. [4]

The first part of the thesis explores the charge-charge interaction between proteins and polyelectrolytes. Polyacrylic acid (PAA) is used as a short model polyelectrolyte with 25 negatively charged repeating monomers, thus aggregation effects are avoided. Its interaction with human serum albumin (HSA) is investigated in a comprehensive experimental and theoretical study. HSA is the most abundant protein in blood serum and is negatively charged at physiological pH. Computer simulation studies were performed by Xiao Xu within the framework of his PhD thesis. Thermodynamic data were collected by means of isothermal titration calorimetry (ITC) and structural analysis performed using small-angle neutron scattering (SANS). The interaction was analyzed by determining binding constants and related thermodynamic information through ITC as a function of ionic strength ($20 - 100$ mM) and temperature ($25\ ^\circ\text{C} - 37\ ^\circ\text{C}$). One to one binding is found and a positive patch on the protein was identified as binding site. Theoretical and experimentally determined free energies of binding ΔG_b are in excellent agreement. The entropic contribution due to the release of counterions upon binding is identified as main driving force for binding, whereby three ions are found to be released upon adsorption. Structural investigations give proof of the stability of the protein beside adsorption.

In the second part, the interaction of two uremic toxins, namely phenylacetic acid (PhAA) and indoxyl sulfate (IDS), with HSA is studied in aqueous solution. These molecules are known to accumulate in patients with declining renal function suffering from chronic kidney disease (CKD). [5] Again, thermodynamic analysis of data obtained by systematic ITC experiments reveal two binding sites for both of the two toxins, with different binding affinities and stoichiometry. The dependence of binding affinities on ionic strength is small in contrast to PAA adsorption to HSA. Thus, a key conclusion here is the identification of the favorable hydrophobic interaction as the driving contribution for adsorption and the enthalpy-entropy compensation (EEC) effect comes into play. SANS studies of high concentrated HSA-toxin solutions proofed the stability of the protein structure and shed light on the interparticle interaction of HSA-toxin complexes. Additionally, the effect of urea induced modification of HSA, as a known pathophysiological condition of CKD, on the binding of the two toxins was studied. Both thermodynamic and structural investigation evidenced only minor effects of the absorption behavior of the protein.

In general, HSA is structurally robust regardless of ligand uptake as revealed by SANS. This finding allows the interpretation of ITC data by confirming that the measured heat signals are purely associated to the binding process. The present thesis has demonstrated that a full thermodynamic analysis in combination with theoretical modelling can provide a comprehensive understanding of binding in terms of identifying driving forces and their contributions to protein ligand interaction.

Zusammenfassung

Die Wechselwirkung zwischen Proteinen und geladenen Molekülen spielt eine wichtige Rolle in vielen gesundheitsrelevanten Bereichen. [1, 2] Nanopartikel, die mit Polyelektrolyten überzogen sind, wechselwirken mit Proteinen sobald sie mit Blut in Kontakt kommen. Ein sogenannter Proteinkranz bildet sich und beeinflusst die physikalischen und chemischen Eigenschaften des Partikels, damit auch seinen Weg durch den Organismus. [3] Im Falle kleiner, geladener Moleküle, wie z.B. Toxinen, kann ihre Aufnahme durch Proteine einerseits die Effizienz von Wirkstoffen und andererseits die Funktionalität des Proteins beeinflussen. [4] Der erste Teil dieser Arbeit untersucht die Ladungswechselwirkung zwischen Proteinen und Polyelektrolyten. Dabei wird Polyakrylsäure (PAA) als kurzes Modell-Polyelektrolyt mit 25 negativ geladenen Wiederholeinheiten verwendet, sodass Aggregationen vermieden werden. Ihre Wechselwirkung mit Humanalbumin (HSA) wird in einer umfassenden experimentellen und theoretischen Studie untersucht. HSA ist das häufigste Protein im menschlichen Blut und ist bei physiologischem pH negativ geladen. Die Computersimulationen in dieser Arbeit wurden von Xiao Xu im Rahmen seiner Promotion durchgeführt. Thermodynamische Daten wurden mit Hilfe von Isothermer Titrationskalorimetrie (ITC) gesammelt und strukturelle Untersuchungen mit Hilfe von Neutronenkleinwinkelstreuung (SANS) durchgeführt. Durch die Analyse von Bindungsaffinitäten und weiteren thermodynamischen Daten bei verschiedenen Ionenstärken und Temperaturen, konnte die Wechselwirkung bestimmt werden. Das Ergebnis zeigte eine eins zu eins Bindung und die Bindungsstelle des Proteins konnte identifiziert werden. Die theoretisch und experimentell bestimmten Bindungsenergien ΔG_b stimmen sehr gut überein. Der entropische Beitrag, der durch die Freisetzung von Gegenionen im Bindungsprozess entsteht, konnte als treibende Kraft für die Bindung identifiziert werden, wobei drei Gegenionen freigesetzt wurden. Die strukturellen Untersuchungen weisen eine stabile Proteilstruktur unabhängig von der Adsorption durch PAA auf.

Im zweiten Teil der Arbeit wird die Wechselwirkung zweier uremischer Toxinen, nämlich Phenylessigsäure (PhAA) und Indoxylsulfat (IDS), mit HSA in wässriger Lösung untersucht. Diese akkumulieren im Körper von Patienten, die an chronischem Nierenversagen (CKD) leiden. [5] Auch hier wurden systematische ITC Experimente durchgeführt und die Analyse der erhobenen Daten weiste die Existenz von zwei unterschiedlichen Bindungsstellen mit unterschiedlicher Stöchiometrie für beide Toxine auf. Im Gegensatz zu PAA, hängen die Bindungsaffinitäten hierbei nur in geringem Ausmaße von der Ionenstärke des Systems ab. Eine wichtige Schlussfolgerung ist daher, dass begünstigende, hydrophobe Wechselwirkungen die treibende Kraft für die Adsorption von Toxinen an HSA sind, und dass hierbei die Enthalpie-Entropie-Kompensation (EEC) zu tragen kommt. Weiterhin zeigen SANS Untersuchungen an hochkonzentrierten HSA-Toxin Lösungen, dass die Proteinstruktur trotz Adsorption stabil bleibt und konnte außerdem über Interpartikulare Wechselwirkung von HSA-Toxin Komplexen aufklären.

Im Allgemeinen ist HSA strukturell unverändert durch die Adsorption von Liganden. Diese Feststellung erlaubt die Interpretation von ITC Daten, da damit gemessene Wärmeprozesse ausschließlich von Bindungsprozessen herrühren und nicht durch z.B. Entfaltungsprozesse beeinflusst sind. Die vorliegende Arbeit konnte zeigen, dass eine ausführliche thermodynamische Analyse durch Kombination von theoretischer mit experimenteller Arbeit, eine umfassende Einsicht in die Mechanismen von Bindungsprozessen ermöglicht.

Table of Contents

1 Introduction

The interaction between proteins and ligands is involved in many essential tasks vital to the survival of all organism and has gained even more significance with growing interest in biomaterials and medical devices. [3] Ligands can be small molecules, such as metabolites and pharmaceuticals, or larger molecules such as polyelectrolytes (PE) that form complexes with biological macromolecules such as proteins. [6] On the one hand, many processes in the human organism involve protein interaction to small, charged molecules, such as active agents, toxins and fatty acids and are therefore of obvious clinical importance. On the other hand, development of polymeric devices for potential biotechnological application has grown significantly in recent years. [7] Polyelectrolytes can be used to synthesize nanoparticles which have been invented as early as in the 1990's to enable a more efficient delivery of pharmaceuticals to their target site. [8, 9] However, once introduced into the blood stream, these particles face the problem of adsorption of proteins to the charged polymeric surface and immediately forming a so called protein corona. [10–12] These adsorbed proteins may trigger an immune response of the body [13, 14]. Hence, nanotoxicology [15] that deals with these unwanted side effects of nanoparticles must consider the interaction of proteins with polyelectrolytes.

In all the scenarios described above, interaction is governed by a complex interplay of different driving forces. A deeper understanding of these driving forces is crucial, but at the same time still represents a challenging task to accomplish. As a result, a lot of resources are put into the elucidation of different contributions in the process of protein adsorption. [16, 17] However, the shear number of different systems and conditions under which interaction takes place, has led to numerous protein and particle specific studies and thus it is impossible to come to general conclusions. Here, the choice of simple model systems studied by combining experimental and computational methods, can give insight into driving mechanisms.

An interesting model protein to study, when it comes to protein ligand/polyelectrolyte interactions, is human serum albumin (HSA), as it is the most abundant protein in blood. HSA is an important transport protein that interacts with substrates as e.g. fatty acids [18, 19] and pharmaceuticals in a specific manner. [20] Also, HSA is clinically relevant as it plays an important role in renal clearance, where uremic toxins accumulate in large numbers in the blood of patients suffering from chronic kidney disease (CKD). [21] They interact detrimentally with plasma proteins and lead to a high risk of cardio-vascular diseases. [5, 22, 23] High concentrations of toxins are reported in patients with end-stage CKD and thus their interaction with HSA needs to be understood in detail. [21, 24, 25]

In general, toxins are subdivided into three classes, namely 1) small molecular weight (MW) water-soluble compounds, 2) protein-bound compounds, and 3) larger MW compounds or "middle molecules", such as polyelectrolytes. [26] It has been recognized that several protein-bound toxins mainly bind to HSA. [22, 24, 27] When bound the the protein, these toxins will inhibit its drug binding ability and may even lead to structural modifications. [25, 27, 28] Removal of these small hydrophobic molecules by dialysis is difficult as they bind tightly to HSA. [29] Recently, Jankowski and coworkers [23, 30] have demonstrated that raising the ionic strength in the infusion fluid leads to an improved clearance of protein-bound toxins (PBT). Thus, raising the concentration of NaCl to 600 mM led to a significantly better removal of uremic toxins as, for instance, phenylacetic acid. [30] This result points clearly to the central importance of Coulombic interactions for the binding strength of such toxins to HSA and to proteins in general. Up to now, only a few studies have explored the dependence on temperature. [31–34] Much less is known about the dependence of the binding strength on ionic strength in detail. [33, 35] Thus, the insufficiency of conventional dialysis in the removal of protein-bound toxins presents a major challenge and improving renal dialysis by solving this problem is thus a central task of clinical nephrology [30, 36]. For this purpose a thermodynamic understanding of the interaction of toxins with HSA is absolutely necessary.

In the present thesis, the binding of two representative protein-bound uremic toxins to HSA is investigated. Both of them are small hydrophobic molecules bearing an ionic moiety (see Figure 1.1). Phenylacetic acid (PhAA) is a toxin that has not yet attracted much attention so far. However, quantitative experiments using equilibrium dialysis (ED) and chromatographic methods have shown that a considerable amount of PhAA is present in dialysis patients prior and after dialysis. [22, 29, 30] The importance of ionic contributions to the binding of this toxin is obvious from the fact that a more effective clearance of PhAA can be reached by raising the ionic strength. [30] Indoxylsulfate is studied as a second toxin because it bears a strong acidic (SO_4^-) group. Hence, a comparison of the thermodynamic data of PhAA bearing a weak acidic group (COO^-) with the ones obtained from IDS can reveal details of the ionic interaction and its relation to toxin binding.
It is furthermore known from literature that HSA is modified in pathophysiological conditions caused by chronic renal failure. [37] The concentration of urea is chronically elevated in patients with renal failure and the subsequent protein modification was identified as risk factor for mortality. [38] Urea-induced carbamylation of HSA on multiple lysine- and arginine-containing chains were found, but the mechanisms of how it contributes to disease is unclear. [39] A hypothesis to be investigated is that the modification of serum albumin might affect binding affinities of uremic toxins and therefore impair its dialysis condition and its subsequent chronically elevated plasma concentrations. The present study therefore explores the effect of urea-modification on binding affinities of PhAA and IDS to HSA and their structure upon complex formation.

Polyelectrolytes (PEs) can be seen as a model for larger MW and charged toxins interacting with proteins. [26] The interaction of long linear polyelectrolytes with proteins in aqueous solution has been the subject of long-standing research that has led to an enormous amount

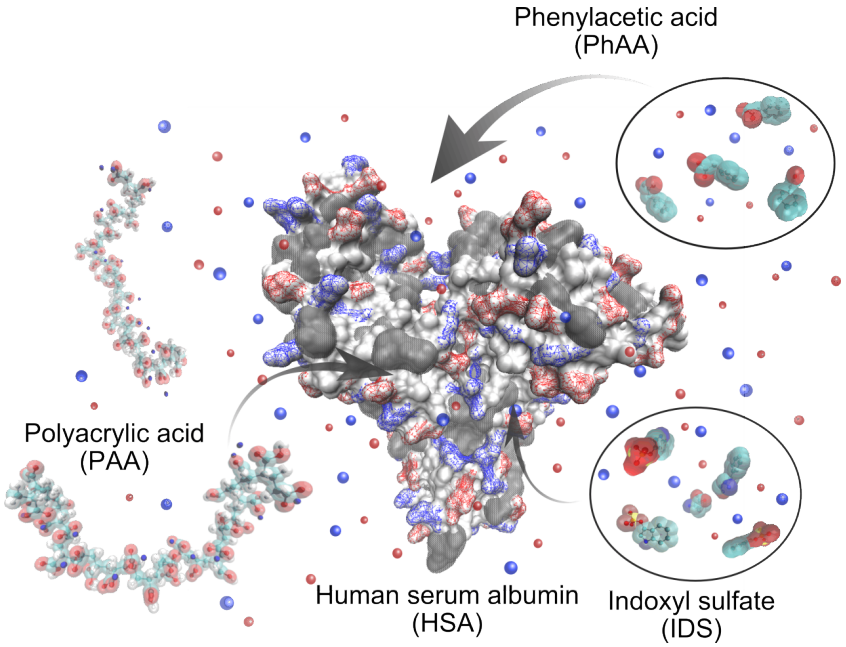

Figure 1.1: Pictural illustration of HSA interaction with different ligands. HSA crystal structure is shown in surface representation, with red being acidic and blue basic amino acids. Dark grey surface represent non-polar residues. PAA and IDS are represented using VDK spheres with equivalent colour coding.

of literature. [40–43] Protein can form complex coacervates with polyelectrolytes of opposite charges in aqueous solution and the strength of the interaction is mediated by the ionic strength in the system. [44] If the ionic strength of the system is low enough, interaction may take place even on the "wrong side" of the isoelectric point, that is, proteins associate with PEs of like charge. In many cases the formation of complexes between the protein and the polyelectrolyte is accompanied by multiple binding processes and can lead to aggregation. [16, 41, 45] This effect however, do not occur for short PEs with only 25 repeating units. Thus in the present thesis, the interaction of a low molecular weight polyanion, polyacrylic acid (PAA), with HSA of same net charge is analyzed (see Figure 1.1). PAA is a biocompatible polyelectrolyte and has been grafted onto planar or curved surfaces to form polyelectrolyte brushes to allow, for instance, enzyme immobilization. [46–48] Using this polyanion, the Coulombic interaction of a protein with charged molecules can be explored to understand the forces that overcomes the simple picture of monopole-monopole repulsion and consequently leads to binding. Furthermore, complementary computer simulations can give additional insight into the binding site and the free energy of binding that can then be compared to experimental results. The different binding contribution are better understood by varying ionic strength and temperature in the system.

A number of techniques have been applied to elucidate the interaction between proteins and ligands/polyelectrolytes. Often used methods to investigate binding affinities of protein-ligand and protein-polyelectrolyte interaction are, for instance, equilibrium dialysis (ED),

ultracentrifugation (UC) and calorimetric methods. [49] Among those, a technique that has been excessively applied to study protein uptake into nanoparticles in terms of binding affinity and thermodynamic signature, is isothermal titration calorimetry (ITC). [50, 51] The major advantage of ITC is that it can access crucial thermodynamic information such as enthalpy, entropy and binding free energy. [52] A first study of the interaction of polyelectrolytes with proteins by ITC has been presented by Schaaf et al. who demonstrated the general suitability of this method for the study of protein-polyelectrolyte interaction. [53] Henzler et al. have also used ITC to acquire thermodynamic information of protein binding to SPBs. [54] In a study of β-lactoglobulin adsorption to a SPB at different ionic strengths, they identified the driving force that overcomes charge repulsion between the like charged protein and SPB. Furthermore, a number of ITC-studies explore the dependence of the adsorption constant on ionic strength. [45, 50, 55, 56] Additionally, ITC has been recognized as an effective method to study protein-ligand binding and is seen as an important tool applied in the field of drug design. [57, 58] Thus, in the present thesis, ITC is used to obtain the binding constant and the number of bound ligands/polyelectrolytes per protein.

Calorimetry alone, however, does not reveal any structural information on the complex. Spatial information can be accessed by crystallography [58, 59], small-angle scattering (SAS) [60–62], Fourier-transformed infrared spectroscopy (FTIR) [63] and dynamic light scattering (DLS) [16]. SAS is a well suited technique to study complexation of macromolecules in solution, where experimental conditions closer to actual physiological conditions can be performed (e.g. physiological pH and temperature). [64–66] It is a technique widely used to elucidate spatial structure of e.g. protein polyelectrolyte complexes. [67–70]
Proteins in general have a good contrast to heavy water and thus neutron scattering is particularly useful to collect scattering data. The coacervation of protein-polyelectrolyte complexes has been investigated using small-angle neutron scattering (SANS), where different structures evolve by varying the pH of the solution and thus changing the effective net charge of both protein and PE. [71] In another study, the adsorption of bovine hemoglobin onto spherical polyelectrolyte brushes (SPB) was monitored by combining small-angle X-ray scattering (SAXS) with FTIR and the distribution of protein within the SPB were characterized. [63] In the present thesis, SANS is used to study protein complexation with ligands and PEs in solution by pushing the technique to its limits of resolution and thus investigating possible structural changes of the protein upon adsorption.

2 Objective of this thesis

The study presented in this thesis is dedicated to explore the binding contribution of ligand and polyelectrolyte (PE) binding to human serum albumin. A model polyelectrolyte and two small molecules were chosen to elucidate the Coulombic and the hydrophobic contribution to interaction. The short chained PE, polyacrylic acid (PAA) interacts attractively with HSA beside their negative charge at a pH above the pI of the protein. The ligands are two representative uremic toxins, which are small molecules composed of an aromatic hydrophobic moiety bearing an ionic group. While the first system explores the driving force that overcomes monopole-monopole repulsion, the second system is medically relevant and particularly interesting in the field of nephrology. Systematic investigations by combining thermodynamic analysis with spatial information of the complexation process allows an in-depth understanding of different contributions to interaction.
The thesis is organized as follows:
The subject of the present thesis is introduced in **Chapter 1** with respect to its general scientific relevance and a brief overview of related research is given.
Chapter 3 and 4 introduces basic physical principles and experimental methods used in this thesis and provides a brief review of literature on the system studied.
In **Chapter 5**, a thermodynamic study on the interaction between PAA and HSA is combined with SANS experiments to explore their structure in solution and compared to pure HSA structure under various conditions. The thermodynamic results are compared to computer simulation studies done by Xiao Xu, who uses a coarse-grained based model of both interacting partners in a dielectric background. The combination of experiment with theory gives an in-depth understanding of driving forces to binding.
Chapter 6 evaluates the binding of the uremic toxins to HSA by combining again thermodynamic studies with structural investigations. Calorimetric experiments comprising a series of temperature and ionic strength measurements were performed to explore different contribution to binding and main driving forces were identified. SANS experiments in high concentrated solutions reveal the impact of toxin adsorption on the interaction between the proteins in solution. Furthermore, the effect of modification of the protein, as is found in pathological conditions, on the binding affinities of the toxins were explored.
Finally, **Chapter 7** summarizes the results of the thesis and elaborates on the relevance of the present study for future developments.

3 Fundamentals

3.1 Protein - ligand/polyelectrolyte interaction

In the following chapter, reversible protein ligand/polyelectrolyte interaction will be discussed, where complex formation is noncovalent and the ligand associate and dissociate in a thermodynamic equilibrium. Ligands can be small molecules, such as metabolites or larger molecules, such as nucleic acids that form complexes with a biological macromolecule such as a protein. Proteins are macromolecules consisting of chains of amino acids with individual sequences that enable highly specific functionality. As such, proteins perform a vast array of functions within organisms. For instance, antibodies attach to viruses or bacteria to mark them for destruction. [72] Cellular signal cascades involve small molecular messengers, transmitted by receptors to finally reach the functional response of a series of molecular recognition processes. [73] The ability to selectively interact with high affinity to a ligand is a result of the sum of multiple interaction contributions, such as electrostatic, van der Waals and hydrophobic interactions. These interactions are enhanced by specific surface contours and conformation of a protein towards certain ligand molecular structures. However, complex formation in biological systems, can be driven by both specificity or affinity. Unspecific binding can occur for instance in pathological conditions, where small toxins in blood adsorb onto proteins and thus inhibiting their biological function. [26]

The protein under investigation in this study is Human serum albumin (HSA). The following chapters are dedicated to the functionality and importance of HSA in the human body and its interaction with various ligands and polyelectrolytes.

3.1.1 Human Serum Albumin (HSA)

Human serum albumin (HSA) is the most abundant protein in blood plasma, accounting for nearly 60 % of the total protein in blood serum and showing a typical concentration in blood of $30-50$ g/L. [74] Albumin, which is synthesized in the liver, is a soluble, monomeric, globular protein with a molecular weight (MW) of ≈ 64 kDa and an isoelectric point (pI) of 4.6. [19] HSA has an exceptional binding capacity for a wide variety of hydrophobic ligands and plays a key role in the transport of hormones, fatty acids, amino acids, metals such as Cu^{2+} and Zn^{2+}, metabolites and pharmaceutical drug compounds. It is therefore believed that HSA is the most essential carrier protein to transport water-insoluble solutes in the bloodstream to target organs such as the liver, intestine, kidney and brain. [75] Beside its role as a transport protein, HSA also contributes significantly to the pH regulation and

osmotic blood pressure. [76]

HSA has been subject to extensive investigations over several decades in terms of its physiological and pharmacological properties. [77, 78] A high resolution crystal structure (2.5 Å) of fat free HSA was published in 1999 by Sugio et al. and is available in the pdb-database (pdb-ID:1AO6). [75] HSA is a single polypeptide chain stabilized with 17 disulfide bridges between the total 585 residues. These form three homologous domains (I, II and III) with each domain made up by two separate helical subdomains (A and B), connected by random coil. The in total six subdomains assemble to form a heart-shaped molecule (see Fig. Figure 3.1). [74]

Albumin is known for its extraordinary capacity to reversibly bind different classes of ligands and toxins to multiple sites. [18, 19, 59, 79–81] Two most prominent binding sites are named Sudlow I and Sudlow II located in the subdomains II-A and III-A, respectively (see Fig. Figure 3.1). [82] Both sites contain deep pockets lined with hydrophobic side chains with their entrance surrounded by positively charged amino acid residues. [75] The interior of Sudlow I is predominantly apolar containing only two clusters of polar residues, both positively charged. Sudlow site II can be distinguished from Sudlow I, as it has a larger solvent accessibility area at its entrance and there is only one single main basic polar patch, located at one side of the entrance. As a result, bulky heterocyclic anions preferably bind to Sudlow I, whereas Sudlows II accommodates aromatic carboxylates or other aromatic compounds. [19, 82] At the same time, those binding sites are the most active and accommodating for drugs on HSA. [83]

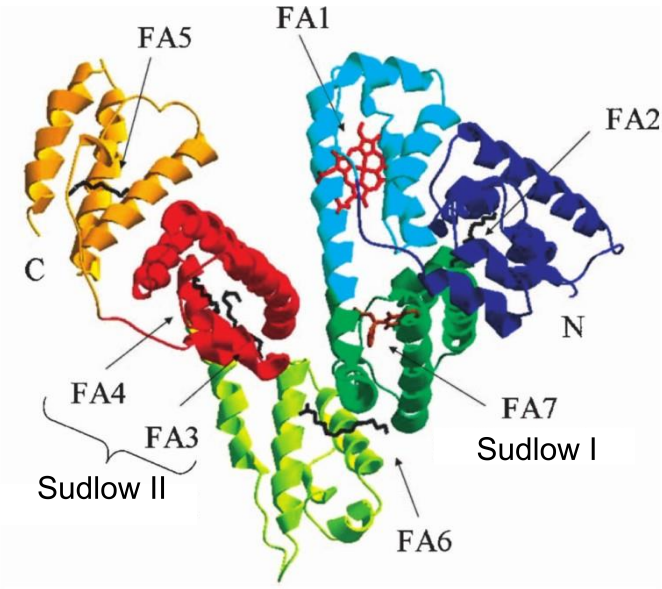

Figure 3.1: Crystallographic representation of HSA complexed with fatty acids/ligands. Adapted from [19].

3.1.2 HSA - ligand binding

Beside its capability to bind many different ligands, HSA is also known to adsorb small toxins, which occur in blood in pathological condition. [22, 24, 27] Among those, well studied toxins and their interaction to HSA are *p*-cresyl sulfate (PCS), hippuric acid (HA) and indoxyl sulfate (IDS). [25, 27, 28] Ghuman et al. have investigated drug-binding specificity of HSA using crystallographic analysis. [84] For several drugs and also uremic toxins, the group identified residues that are key determinants of binding specificity of the two Sudlow binding pockets. [84] Depending on the polarity and electrostatic properties of the ligand, hydrogen-bonds or salt-bridges can stabilize their binding to a protein. In the case of IDS, a total of four hydrogen-bond or salt bridges are formed during binding at Sudlow II, with its indole amide group interacting with the carbonyl oxygen of Leu430 (see Figure 3.2). Again, binding affinities for IDS to HSA are found to be rather strong $\sim 10^5 - 10^6$ mol^{-1}. [24, 85]

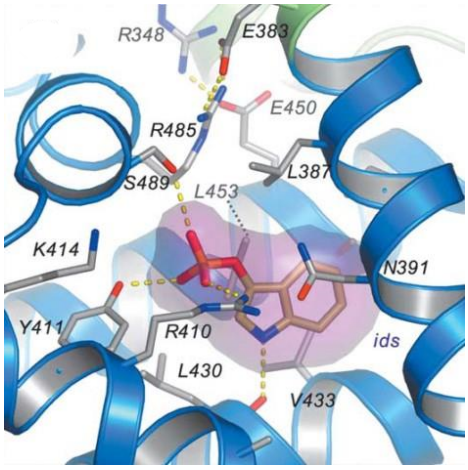

Figure 3.2: Binding sites of HSA complexed with IDS. The color code of the α-helices corresponds to different subdomains. IDS and selected side-chains are shown in stick representation with semitransparent van der Waals surfaces. The sticks are colour-coded by atom type: carbon - orange; oxygen - red; nitrogen - blue; chlorine - green. Yellow dashed lines indicate hydrogen-bonds. Adapted from [84].

There are a series of methods to study binding affinity between various ligands to HSA. [49, 86, 87] Yet, the results obtained by different methods can differ by orders of magnitude and care must be taken, when comparing binding affinities derived from different experiments. A set of well studied examples for the binding of common ligands to HSA investigated by different techniques is listed in Table 3.1. Typically, studies are conducted at either room (25 °C) or body temperature (37 °C) and pH 7.4. [27, 88]

The binding of uremic toxins have been investigated by different experimental techniques and a comparison of results is shown in Table 3.1. The interaction of IDS and PCS with HSA was studied using equilibrium dialysis (ED), ultrafiltration (UF), liquid chromatography (LC) and ultracentrifugation (UC). Different K_b were obtained depending on the experiment performed. These separative methods used are based on differences in molecular size and/or weight and thus they are very fast and easily performed. However, unwanted interaction of protein or ligand with the membrane necessary for these methods is unavoidable and protein leakage may arise. [89] Furthermore, physical phenomena such as back diffusion and viscosity effects may influence the determination of free ligand concentration and thus

significant discrepancies occurred when comparing results obtained by ED and UC. [90]

Another approach to analyze protein ligand binding using non-separative methods are spectroscopic techniques such as fluorescence spectroscopy (FS), nuclear magnetic resonance (NMR), circular dichroism (CD), and many more. These methods are based on the perturbation of the electronic energy levels of either the ligand or the protein upon binding. The adsorption of the uremic toxin hippuric acid (HA) to HSA was investigated comparing ITC and steady state fluorescence quenching (SSFQ). [31] The binding affinity obtained under different temperatures differ by about one order of magnitude (see Table 3.1). While ITC can detect two binding processes, only one binding site was detected by SSFQ. The authors remark that binding affinities obtained by SSFQ may be influenced by the quencher fluorophore and thus rely more on ITC in determining K_b. [31].
Two more examples of well studied anti-inflammatory drugs are ibuprofen and naproxen, both negatively charged at neutral pH [88] and reported to bind preferable to the Sudlow site II (see Table 3.1). [82, 84] Binding affinities of ibuprofen adsorption to HSA obtained by ITC from different authors are comparable in magnitude[88, 91], the values obtained by difference circular dicroism (DCD) and affinity capillary electrophoresis (ACE) are an order of magnitude smaller. [92, 93]

With a wide range of experimental possibilities, the selection of an appropriate method depends on the type of information desired. A comparison of the different ranges of K_b and information that can be accessed with some commonly used methods limitations and advantages are presented in Table 8.2 in the Appendix. Among these methods, ITC combine the ability to obtain reliable binding affinities with the benefit of providing information on enthalpy and entropy. Furthermore, both ionic strength and temperature were found to influence the interaction between protein and ligand. Thus, for a comprehensive thermodynamic understanding of the interaction, it is necessary to perform experiments combining a set of temperature and ionic strength measurements to explore different binding contributions.

Table 3.1: HSA interaction with different ligands, investigated by different techniques in the literature.

Ligand	Chemical structure	Methods*	T (°C)	I (mM)	K_{b1} (10^3 M^{-1})	N_1	K_{b2} (10^3 M^{-1})	N_2	Reference
Ibuprofen	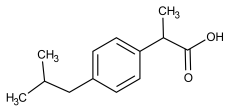	ACE	25	50	24	-	-	-	[92]
		FS	25	50	2.4	-	-	-	[94]
		ITC[a)]	25	50	900±100	0.84	-	-	[88]
		ITC[a)]	25	50	303	1.1	-	-	[91]
		DCD	37	50	14	-	36	-	[93]
		CE/FA	37	67	710	1.0	14	7.6	[95]
Flurbiprofen	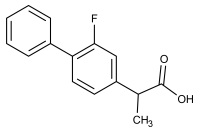	ITC	25	50	5000±3000	0.7	(60±40)	4.8	[88]
		CE/FA	25	50	-	-	35±3	5.0±0.1	[88]
		ED	37	66	1200	-	140	-	[96]
		ED	37	67	1380	1.19	8.98	7.7	[97]
Hippuric acid	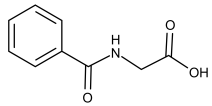	SSFQ	25	20	6.8±0.2	0.98	-	-	[31]
			30	20	3.1±0.2	0.99	-	-	[31]
			37	20	1.04±0.01	0.97	-	-	[31]
		ITC[b)]	25	20	28±0.5	1	2.8±0.5	1	[31]
			30	20	25±1	1	1.38±0.03	1	[31]
			37	20	15±1	1	1.29±0.07	1	[31]
Indoxyl sulfate	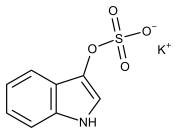	ED[c)]	25	67	910±290	1	8±4	3	[24]
		ED/UC[c)]	25	67	1610	1	8.3	3	[27]
		LC	30	150	57±2	-	-	-	[98]
		UF[c)]	25	150	98	1	8	1.6	[85]
		ED & UF[e)]	24	150	10.2	2.7	-	-	[25]
P-cresyl sulfate	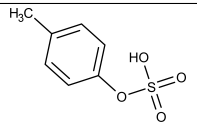	ED[c)]	25	67	910±290	1	8±4	3	[24]
		ED& UF[e)]	24 & 37	150	17.7	2.9	-	-	[25]

ACE: Affinity capillary electrophoresis, ED: equilibrium dialysis, CE/FA: capillary electrophoresis/frontal analysis, DCD: difference circular dicroism, FS: fluorescence spectroscopy, ITC: isothermal titration calorimetry, SSFQ: steady state fluorescence quenching, LC: liquid chromatography, UF: ultrafiltration, UC: ultracentrifugation.

Binding equilibrium data/isotherms were analyzed using a) model for one set of identical sites, b) sequential binding mode for two independent sites, c) a model of binding of two ligands to one protein with two different and independent sites m, d) an one site specific binding model, e) Hill analysis

All experiments listed here were performed at pH 7.4

3.1.3 Protein - polyelectrolyte interaction

Interactions of polyelectrolytes (PEs) with proteins and the formation macromolecular complexes is a subject extensively studied with a wide range of applicability in medical and pharmaceutical areas such as drug delivery [3, 99, 100], nanodevices and sensors [101, 102], protein purification [16, 43], and enzyme immobilization [56]. As proteins are charged colloidal particles, they can interact electrostatically with DNA, RNA and polyelectrolytes and thus forming soluble complexes. [17, 103, 104] An electrostatic picture of the protein will depend on solvent pH as many amino acid residues are zwitterions. Studies by Dubin et al. showed that complexation between synthetic polyelectrolytes and globular proteins show at least three different phases of interaction as a function of pH and salt concentration in the solution (see Figure 3.3). [42, 55, 105, 106] In the case of e.g. a negatively charged PE, at least three states: (i) above a critical pH_{crit}, electrostatic repulsion prevent interaction between protein and polyelectrolyte, (ii) below pH_{crit}, soluble aggregates are formed and (iii) a further decrease of pH will lead to macroscopic phase separation of an insoluble complex. In case of weak polyelectrolytes, an additional phase can occur for even lower pH, where the PE is neutralized. [107] The phase diagram sensitively depend on salt concentration in the system as an electrostatic screening comes into play with increasing salt. [108–110]

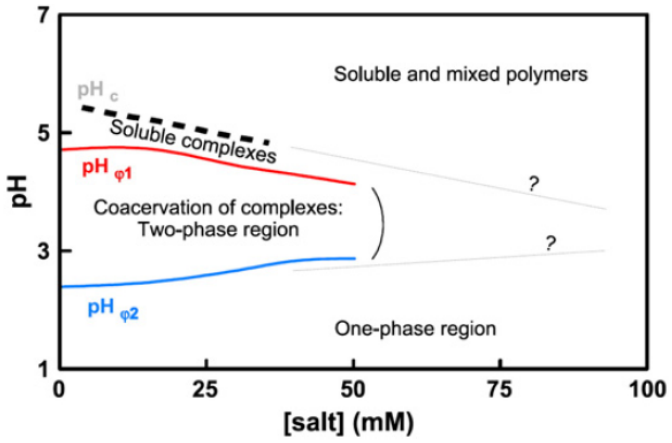

Figure 3.3: Phase diagram of weak polyacid interacting with globular proteins as a function of pH and salt concentration. More than three states of interaction can exist depending on the system: (i) absence of interaction above pH_{crit}, (ii) soluble complex formation, (iii) coacervation and an one-phase region coexist where the charge of the weak PE is neutralized. This phase does not exist for strong PEs. Adapted from [107].

It has also been recognized that interaction can occur at the "wrong side of pI", where proteins interact with polyelectrolytes while both bearing the same sign of charge (see Figure 3.3). [42, 111, 112] This means that attractive interaction exists that overcomes monopole-monopole repulsion of charges. An explanation is found in the heterogenous charge distribution of proteins, that is, for instance positive charges are assembled to patches on the protein, while the overall net charge is negative. These patches act as multivalent counterions to PEs and

thus overcome repulsion. [104, 113, 114] Upon interaction, counterions previously condensed on the PE chains are released and contribute significantly to a favorable change of entropy in the system. This effect is known as the *counterion release force* and has been observed for the binding of proteins onto spherical polyelectrolyte brushes. [17, 54, 115] In several studies on PE-protein coacervation and aggregation, binding processes were also entropically driven and considered as the main driving force for complexation at the "wrong side of pI". [16, 45, 110, 116] The release of ions involving polyelectrolyte association to form a complex is described by Record and Lohman and will be discussed in more detail in Section 3.2.3. [117]

Theoretical studies explore the interaction between a single, highly charged PE chain with like-charged patchy protein models and give clear proof of the *counterion release force*. [118] Snapshot of computer simulations by means of Langevin dynamics with implicit solvent and explicit ions is shown in Figure 3.4. [118] The protein is modeled as a charged patchy particle (CPPM) and is represented by a yellow sphere with a white patch in Figure 3.4. Negative charges are red and distributed over the CPPM and positive charges are blue and located within the patch. This patchy distribution leads to a dipole moment of the order of 10^2-10^3 Debye as typically found for proteins. The PE consists of 25 monomers, each bearing one negative charge, represented by orange beads. Positive ions represented as green beads are seen to be condensed on the PE prior to adsorption (Figure 3.4A). Figure 3.4B shows the PE chain adsorbed onto the positive patch of the protein as charge-dipole attractions dominate in short distances over the monopole repulsion, as seen by other studies. [119, 120] The main contribution originates from the counterions released upon binding, leading to an increase of the entropy in the system and a concomitantly negative contribution to the free enthalpy of binding.

To study the influence of charge-charge interaction experimentally, it is essential to explore the influence of salinity on binding. It has been argued that electrostatic interactions are completely screened under physiological condition where the ionic strength is of the order of 150 mM. However, binding may still prevail beside high salt concentrations and a central point of this thesis is to gain a detailed understanding of driving forces for binding by a direct comparison of experiments with simulations.

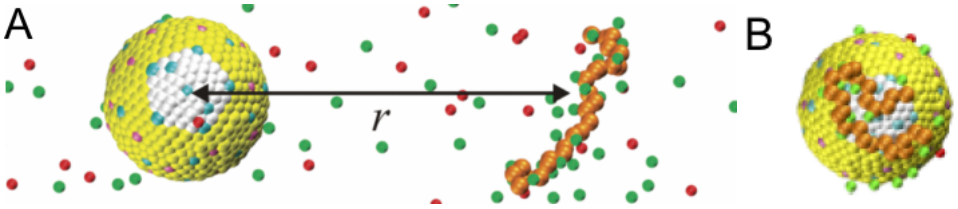

Figure 3.4: A) Exemplary snapshot of a CPPM with a highlighted white patch where blue spots mark the positive charges interacting with a negatively charged PE (orange beads) with explicit salt ions (green beads represent positively and red negatively charged ions) in a center-to-center distance r. B) Representative snapshot of a case where the PE chain is fully adsorbed onto the protein patch. Adapted from [118].

3.2 Binding thermodynamics of ligands to proteins

In the following section, a few of the physical models underlying the analysis of the ITC results collected in the present study will be presented, while details may be found in other literature. [72, 121–124]

3.2.1 Binding to a single set of identical sites (SSIS)

In the simplest case of a binding equilibrium, where the protein P has only one binding site and a single ligand L binds, the binding process can be expressed:

$$P + L \xleftrightarrow{K_b} PL \quad \text{with} \quad K_b = \frac{[PL]}{[P][L]} \tag{3.1}$$

where K_b is the binding constant and characterizes the affinity of binding. In experiments, binding isotherms are measured and a binding parameter b can be obtained either directly or indirectly. b is defined as the average number of ligand molecules that are bound per protein and covers a range from 0 to n, where n is the number of binding sites per protein, therefore yields:

$$b = \frac{[L]_b}{[P]_t} = \frac{[PL]}{[P] + [PL]} = \frac{K_b[L]}{1 + K_b[L]} \tag{3.2}$$

where $[L]_b$ is the concentration of bound ligand, $[L]$ the free ligand concentration, $[P]_t$ the total protein concentration, $[P]$ the free protein concentration and $[PL]$ the concentration of ligand-protein complexes. A different, experimentally accessible binding parameter (indirectly measured by e.g. ITC), is the saturation fraction Θ, which gives the fraction of binding sites occupied by a ligand. It is related to b by $\Theta = b/n$, where n is the number of free binding sites and ranges from zero to one at full occupancy. Equation (3.2) can then easily be extended for the case that n identical sites exists on the protein by multiplication with n and thus simply replacing b with Θ:

$$K_b = \frac{\Theta}{(1 - \Theta)[L]} \tag{3.3}$$

This is the **Langmuir adsorption isotherm** which describes the adsorption of gas molecules on surfaces. [121] In an ITC experiment, only the total concentration of ligand $[L]_t$ in the solution is known and the free ligand concentration $[L]$ is connected to $[L]_t$ as followed:

$$[L]_t = [L] + n\Theta[P]_t \tag{3.4}$$

Combining Equation (3.3) and Equation (3.4) gives:

$$\Theta^2 - \Theta + \left[1 - \frac{[L]_t}{n[P]_t} + \frac{1}{nK_b[P]_t}\right] + \frac{[L]_t}{n[P]_t} = 0 \tag{3.5}$$

The total heat of adsorption Q is measured in an experiment as a differential heat Q' divided by the moles of ligand in the j-th titrant injected $\mathrm{d}l_j$ with $\mathrm{d}l_j \approx V_t \cdot \mathrm{d}[L]_t$. The differential heat Q' can be expressed in general as a differential equation: [125]

$$Q' = \frac{\mathrm{d}Q}{V_t \cdot \mathrm{d}[L]_t} = \sum_{m=1}^{n} \Delta H_m \frac{\mathrm{d}[PL_m]}{\mathrm{d}[L]_t} \tag{3.6}$$

where n is the number of binding sites, V_t the cell volume and ΔH_m the molar heat of the reaction. For the SSIS model, the expression for Q reads:

$$Q = n\Theta[P]_t \Delta H_{ITC} V_t \tag{3.7}$$

with ΔH_{ITC} as the total enthalpy of the system measured by ITC. Solving the quadratic Equation (3.5) for Θ and substituting this into Equation (3.7), one obtains:

$$Q([L]_t) = \frac{n[P]_t \Delta H_{ITC} V_t}{2} \left[1 - \frac{[L]_t}{n[P]_t} + \frac{1}{nK_b[P]_t} - \sqrt{\left(1 + \frac{[L]_t}{n[P]_t} + \frac{1}{nK_b[P]_t}\right)^2 - \frac{4[L]_t}{n[P]_t}} \right] \tag{3.8}$$

In the continuum limit, the derivative $\mathrm{d}Q([L]_t)/\mathrm{d}[L]_t$ with respect to V_t is given by the following equation:

$$Q' = \frac{\mathrm{d}Q}{V_t \cdot \mathrm{d}[L]_t} = \frac{\Delta H_{ITC}}{2} \left[1 - \frac{-1 + \frac{[L]_t}{n[P]_t} + \frac{1}{nK_b[P]_t}}{\sqrt{\left(1 + \frac{[L]_t}{n[P]_t} + \frac{1}{nK_b[P]_t}\right)^2 - \frac{4[L]_t}{n[P]_t}}} \right] \tag{3.9}$$

The fitting of the experimental data is performed by calculating the incremental heat Q' released with each titration using manually set initial values and comparing these values with the measured isotherm. The initial values are then compared with the measured isotherm and improved by using the standard Marquardt method. These steps are repeated until a satisfactory fit is achieved. Q' is given by: [126]

$$Q'_i = Q_i + \frac{\mathrm{d}V_i}{V_t} \left[\frac{Q_i + Q_{i-1}}{2} - Q_{i-1} \right] \tag{3.10}$$

Manually set initial values are used to compare with the measured isotherm.

3.2.2 Binding to two sites

In the following, two models describing the binding of ligands to two independent binding sites with different affinities is presented.

3.2.2.1 Sequential binding to two different, independent sites (SBS)

In the sequential model, binding affinities are defined relative to the progress of saturation, that is binding at one site takes place relative to the progress of the other site. The model furthermore assumes that for each step, only one ligand is bound to the according site. There are two different but equivalent ways describe the binding process. [123] A schematic depiction is given in Figure 3.5 to illustrate the difference between the two approaches.

1. Binding takes place in two steps, where the first equilibrium process is the binding of one ligand to one site of the protein, described by the binding constant k_{b1}. The second step is the binding of a second ligand to the second site (accordingly described

by k_{b2}) thus achieving saturation. For each equilibrium step, a binding constant can be defined:

$$P + L \xleftrightarrow{k_{b1}} PL \qquad PL + L \xleftrightarrow{k_{b2}} PL_2 \tag{3.11}$$

$$k_{b1} = \frac{[PL]}{[P][L]} \qquad k_{b2} = \frac{[PL_2]}{[PL][L]} \tag{3.12}$$

2. Binding equilibrium exists between both free and bound ligand with either one or two bound ligand molecules. The equilibrium formula for this case is related to the one above as follows:

$$P + L \xleftrightarrow{\beta_1} PL \qquad P + 2L \xleftrightarrow{\beta_2} PL_2 \tag{3.13}$$

$$\beta_1 = \frac{[PL]}{[P][L]} = K_{b1} \qquad \beta_2 = \frac{[PL_2]}{[P][L]^2} = K_{b1} \cdot K_{b2} \tag{3.14}$$

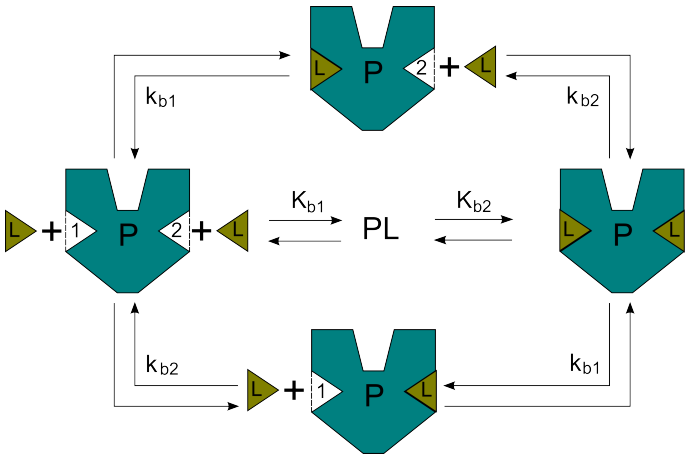

Figure 3.5: Schmatic depiction of the sequential binding model. The binding of two ligands (brown triangles) to the protein (turquoise forms) incorporating two different binding sites can be described following two approaches. The steps labeled with k_{bi} are described in the first and the binding equilibrium labeled with K_{bi} in the second point above.

The total ligand concentration $[L]_t$ in Equation (3.4) introduced in the SSIS model becomes:

$$[L]_t = [L] + [P]_t \left(\underbrace{\frac{[L]k_{b1}}{1 + k_{b1}[L] + k_{b1}k_{b2}[L]^2}}_{F_1} + \underbrace{\frac{2k_{b1}k_{b2}[L]^2}{1 + k_{b1}[L] + k_{b1}k_{b2}[L]^2}}_{F_2} \right) \tag{3.15}$$

defining the two sums in the brackets as F_1 and F_2 accordingly, it follows for the total heat Q:

$$Q = [P]_t V_t \left(F_1 \Delta H_1 + F_2 [\Delta H_1 + \Delta H_2] \right) \tag{3.16}$$

3.2.2.2 Binding to two sets of independent sites (TSIS)

A different formalism to describe a two-sites model compared the approach above, is to define two sets of parameters for each site, namely two binding numbers n_i, enthalpies ΔH_i and microscopic equilibrium constants k_{bi}. Binding is described by the following reaction:

$$P + (n_1 + n_2)L \xleftrightarrow{k_{b1}k_{b2}} PL_{n_1+n_2} \tag{3.17}$$

each binding constant is defined as in Equation (3.3):

$$k_{b1} = \frac{\Theta_1}{(1-\Theta_1)[L]} \qquad k_{b2} = \frac{\Theta_2}{(1-\Theta_2)[L]} \tag{3.18}$$

and the binding parameter is expressed as:

$$b = n_1\Theta_1 + n_2\Theta_2 = \sum_{i=1}^{n=2} \frac{n_i k_i \cdot [L]}{1 + k_i \cdot [L]} \tag{3.19}$$

In contrast to the SBS model introduced in Section 3.2.2.2, k_{b1} and k_{b2} are microscopic binding constants describing the binding affinity of a ligand to the corresponding site. In this model, six free parameters are involved. Namely for each site two enthalpies ΔH_i^{ITC}, binding numbers N_i and binding constants k_{bi} respectively. Thus fitting must be carried out carefully with respect to using to many free parameters.

3.2.3 Basic thermodynamic relationships

ITC can provide a full set of thermodynamic information, such as binding affinity K_b, stoichiometry n and the change of enthalpy (ΔH_b), entropy (ΔS_b) and free energy (ΔG_b) of interaction. While ΔH, n and K_b are directly measured quantities, the Gibbs free energy ΔG_b can be calculated as follows: [72]

$$\Delta G_b = -RT \cdot \ln K_b \tag{3.20}$$

where R is the universal gas constant. Another fundamental equation linking free energy, enthalpy and entropy is:

$$\Delta G_b = \Delta H_b - T\Delta S_b \tag{3.21}$$

The dependence of the binding free energy on temperature is given by:

$$\Delta G(T) = \Delta H(T_0) + \int_{T_0}^{T} \Delta C_p \mathrm{d}T - T\Delta S(T_0) - \int_{T_0}^{T} \Delta C_p \mathrm{dln}T \tag{3.22}$$

where T_0 is an appropriate reference temperature and ΔC_p is the heat capacity change that is derived by the partial derivative of enthalpy with respect to temperature at constant pressure:

$$\Delta C_p = \left(\frac{\partial \Delta H}{\partial T}\right)_p \tag{3.23}$$

For the case where ΔC_p is constant in the temperature range of interest, Equation (3.22) simplifies to:

$$-RT\ln K_b = \Delta G(T) = \Delta H(T_0) - T\Delta S(T_0) + \Delta C_p \left[T - T_0 - T\ln\left(\frac{T}{T_0}\right)\right] \tag{3.24}$$

Here, both enthalpy and entropy depend on temperature through the change of heat capacity. Dividing Equation (3.24) by T and taking the derivative with respect to $1/T$ yields the van't Hoff analysis:

$$-R\frac{\partial \ln K_b}{\partial(\frac{1}{T})} = \Delta H^0_{vH} + \Delta C_p(T - T_0) \tag{3.25}$$

where we define $\Delta H^0_{vH} = \Delta H_b$ as binding enthalpy. In many systems, ΔC_p can be diminishing, such that the approximation $\Delta C_p \approx 0$ holds and the van't Hoff relation yields:

$$\left(\frac{\partial \ln K_b}{\partial T^{-1}}\right)_p = -\frac{\Delta H_b}{R} \tag{3.26}$$

From this equation, ΔH_b can be obtained from the slope of the linear fit and ΔS_b from the intercept of the integrated form:

$$\ln K_b = -\frac{\Delta H_b}{RT} + \frac{\Delta S_b}{R} \tag{3.27}$$

In Section 3.1.3, the entropic contribution of the *counterion release force* was discussed, as observed in polyelectrolyte complexation with proteins. This phenomenon was considered many years ago by Record and Lohman who predicted a linear correlation between the logarithms of binding constant K_b and salt concentration in solution c_s: [117]

$$\frac{\mathrm{d}\ \ln K_b}{\mathrm{d}\ \ln c_s} = -\Delta N_{ion} \tag{3.28}$$

where ΔN_{ion} is the number of ions released into bulk upon binding. In the case of a positive protein patch interacting with a negative polyelectrolyte, negative and positive counterions $\Delta N_{\pm}$ can be released respectively. This favorable entropic contribution leads directly to a negative contribution to the free energy of binding and the according change ΔG_{cr} is given by: [54]

$$\Delta G_{cr} = \frac{\Delta N_-}{kT}\ln\left(\frac{c_s}{c_{patch}}\right) + \frac{\Delta N_+}{kT}\ln\left(\frac{c_s}{c_{PE}}\right) \tag{3.29}$$

where c_{patch} is the concentration of negative counterions accumulated on the positive patch and c_{PE} the surface concentration of positive condensed ions of the PE. Depending on the ratio between the counterion concentrations of PE and protein, and the total salt concentration, the free energy contribution can be significantly large.

3.3 Small-angle neutron scattering (SANS)

Small-angle neutron scattering (SANS) is a non-destructive technique to characterize structures with sizes varying from several Ångströms to a few hundreds of nanometers. Thereby, one takes advantage of the fact that changes in the scattering angle of the neutron are related to structural properties of the sample. In the following chapter, a brief summery of the basics of small-angle scattering is given. [127–129]

3.3.1 General theory

Figure 3.6 shows a scheme of a scattering experiment. An incident beam of neutrons with the wave vector $\mathbf{k}_i$ and the wavelength $\lambda = 2\pi/|\mathbf{k}_i|$ is scattered in a single and elastic process such that $|\mathbf{k}_i| = |\mathbf{k}_s|$ holds. The scattered wave $\mathbf{k}_s$ is emitted with a fixed phase relationship to $\mathbf{k}_i$ with an angle of 2θ. The resulting scattering vector $\mathbf{q}$ is defined as:

$$\mathbf{q} = \mathbf{k}_i - \mathbf{k}_s \quad \text{and} \quad |\mathbf{q}| = \frac{4\pi}{\lambda}\sin(\theta) \tag{3.30}$$

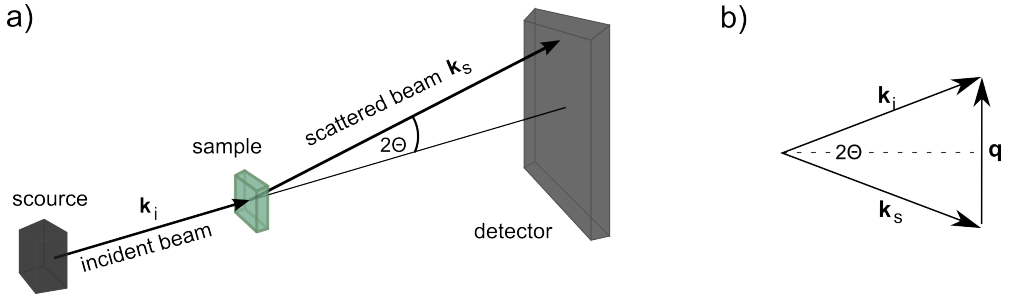

Figure 3.6: Schematic depiction of a small-angle scattering experiment. (a) The geometrical representation of the experiment shows an incident beam $\mathbf{k}_i$ that is scattered by a sample and arrives at the detector as $\mathbf{k}_s$ under the scattering angle 2θ. (b) The difference of incident and scattered wave gives the scattering vector $\mathbf{q}$.

The common way to describe the scattering is to start with the incoming wave with the amplitude A_0 that is scattered by a particle i at the location r_i. The emitted wave $A(\mathbf{q})$ is then the sum over all amplitudes scattered by the particles in solution:

$$A(\mathbf{q}) = A_0 \cdot \sum_i b_i e^{-i\mathbf{q}\mathbf{r}_i} \tag{3.31}$$

where b_i is a value depending on interaction between the radiation and the scattering particle and will be specified later. The discrete scattering centers can be approximated by a continuous scattering length density (SLD) function $\rho(\mathbf{r})$ within the sample volume V with the assumption of small scattering angles and thus transfer the above sum into an integral over V.

$$A(\mathbf{q}) = \int_V \rho(\mathbf{r}) e^{-i\mathbf{q}\mathbf{r}} d\mathbf{r} \tag{3.32}$$

This integral can be identified as the Fourier transform of the SLD function $\rho(\mathbf{r})$, which can be split into a sum of a constant mean value $\langle\rho\rangle$ and a location-dependent part:

$$\rho(\mathbf{r}) = \langle\rho\rangle + \delta\rho(\mathbf{r}) \tag{3.33}$$

The scattering of $\langle\rho\rangle$ contributes only in the forward direction $\mathbf{q} = 0$ and therefore is experimentally not detectable. Finally, the experimentally accessible quantity is the number of detected neutrons that are scattered into a solid angle $d\Omega$ around a given direction which gives the differential cross section $\frac{d\sigma}{d\Omega}$. This quantity is related to the scattering intensity

$I(\mathbf{q})$ (i.e. the squared scattering amplitude), which in combination with Equation (3.32) and Equation (3.33) yields:

$$\frac{d\sigma}{d\Omega} \equiv I(\mathbf{q})/V = |A(\mathbf{q})|^2 = \frac{1}{V}\left|\int_V \delta\rho(\mathbf{r}) e^{-i\mathbf{qr}} d\mathbf{r}\right|^2 \tag{3.34}$$

Normalizing $I(q)$ to the sample volume V establishes the differential cross section in units of so-called macroscopic cross sections cm^{-1} independent of the instrument and its sample geometry.
For neutrons, the scattering length introduced in Equation (3.31) as b_i, consists of a coherent and an incoherent contribution:

$$\frac{d\sigma}{d\Omega} = b_{coh}^2 \cdot \sum_{ij}^{N} \langle e^{-i\mathbf{q}(\mathbf{r}_i - \mathbf{r}_j)} \rangle + N \cdot b_{inc}^2 \tag{3.35}$$

$$= \left(\frac{d\sigma}{d\Omega}\right)_{coh} + \left(\frac{d\sigma}{d\Omega}\right)_{inc} \tag{3.36}$$

with the number of scatterers N at positions $\mathbf{r}$. This equation demonstrates that the information about form and spatial correlation of the scatterers is only contained in the first term, while the second term only arises from fluctuations in scattering length b and is independent of $\mathbf{q}$. Again going to a continuous distribution of scatterers, we can write the coherent SLD as:

$$\rho_{coh}(\mathbf{r}) = \sum_i \rho_i(\mathbf{r}) b_{coh}^i \tag{3.37}$$

In the following equations, we assume an isotropic system in recognition of the fact that the system contains a large number of particles oriented in random directions. It follows that the intensity $I(\mathbf{q})$ can be obtained by averaging the absolute square of $A(\mathbf{q})$ over all possible orientations of the particle and the vector $\mathbf{q}$ can be replaced by a scalar q.

3.3.2 Scattering of particles in solution

In a dilute system consisting of N particles in a volume V, the particles do not "sense" their neighbors. Their positions are therefore uncorrelated without any fixed phase relation between waves scattered by different particles. Thus, the overall intensity is simply the sum of all particle scattering and normalized to the sample volume:

$$I(q) = (\Delta\rho)^2 \cdot \frac{N}{V}\left\langle \left[\int_{V_P} e^{-i\mathbf{qr}} d^3r\right]^2 \right\rangle = (\Delta\rho V_P)^2 \cdot \frac{N}{V}\left\langle [F(q)]^2 \right\rangle \tag{3.38}$$

where V_P is the particle volume, V the illuminated sample volume as defined before and the contrast $\Delta\rho = \rho_p - \rho_s$ as the difference between SLD of particle and solution. Here, we assume constant scattering length densities ρ_p for identical particles dispersed in a continuous matrix of solution with ρ_s. $F(q)$ can be identified as the particle form factor, which contains information about the geometry of the individual scatterer.
In a more dense system of scatterers however, the positions of individual scatterers are no longer independent and interference between waves scattered from neighboring particles

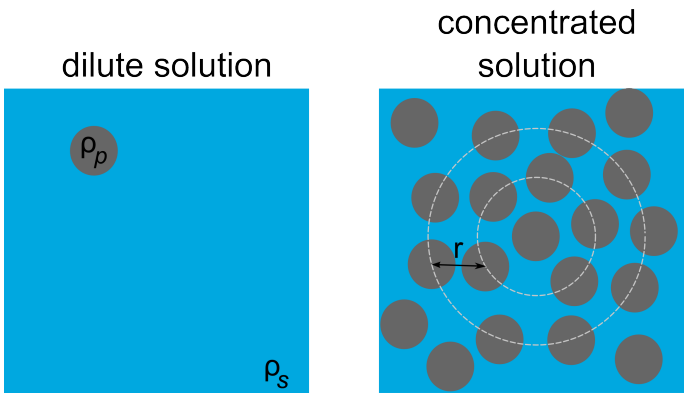

Figure 3.7: Schematic comparison of scattering from dilute and concentrated solutions with ρ_p and ρ_s as the scattering length densities of particle and solution respectively.

can occur. The difference compared to a dilute system is illustrated in Figure 3.7. As a result, the above Equation (3.38) becomes:

$$I(q) = (\Delta\rho V_p)^2 \cdot \frac{N}{V} \left\langle [F(q)]^2 \right\rangle S(q) \tag{3.39}$$

where in experiments, a particle scattering term is often defined as $P(q) = \left\langle [F(q)]^2 \right\rangle$. $S(q)$ is the structure factor, which describes the spatial correlation of N particles separated by the distance r. $S(q)$ is defined as:

$$S(q) = 1 + \frac{N}{V} \int 4\pi r^2 [g(r) - 1] \frac{\sin qr}{qr} dr \tag{3.40}$$

with $g(r)$ as the pair correlation function.
A total correlation function can be defined $h(r) = g(r) - 1$ which describes the influence of a particle 1 on a second particle 2 with a distance r in between them. The total correlation function can be divided into a sum of a direct and an indirect part:

$$h(r) = \underbrace{c(r)}_{\text{direct part}} + n \underbrace{\int c(R)h(r-R)dR}_{\text{indirect part}} \tag{3.41}$$

This equation is also known as the Ornstein-Zernike (OZ) integral, where the direct correlation function $c(r)$ needs to be determined. In the first term, $c(r)$ yields the direct influence of two neighboring particles and thus only depends on a short ranged interaction potential. The second term gives the indirect interaction of a particle at position r via an intermediary third particle at the distance R, given by the integral.

3.3.2.1 Structure factor for charged particles in solution

An analytical structure factor to describe the correlated scattering of macroions in solution was developed by J.B. Hayter and J. Penfold in the early 1980's. [130] The present paragraph aims to define basic principles and equations underlying the Hayter-Penfold

Mean-Spherical-Approximation (HPMSA) that is used in this thesis to analyze interparticle interaction between proteins in solution.
The macroion system by Hayter and Penfold is based on the following assumptions: (i) the properties of macroions dominate the contribution towards interaction in solution and (ii) the macroions can be described as charged spheres with a finite volume and interact via a screened Coulomb pair potential. In such a case, the weak Van-der-Waals interaction can be safely neglected. [130]

The Mean-Spherical-Approximation (MSA) [131] is based on the Debye-Hückel theory but takes into account volume exclusion effects. Instead of a point mass, the spherical macroions in solution have a diameter d and interact via the repulsive potential:

$$U(r) = \frac{\pi\epsilon_0\epsilon d^2\psi_0^2}{r} \cdot e^{[-\kappa_D(r-d)]}, \quad r > d \tag{3.42}$$

where r is the distance between the macroions, ψ_0^2 the surface potential, ϵ the dielectric constant of the solution and κ_D the above mentioned inverse Debye length. ψ_0^2 depends on the charge z_m of the macroions and is given in good approximation by:

$$\psi_0 = \frac{z_m}{\pi\epsilon_0\epsilon\sigma(2+\kappa d)} \tag{3.43}$$

In the following, we shall keep the notation Hayter and Penfold and define the dimensionless variables:

$$x = r/d, \quad k = \kappa d, \quad K = Qd \tag{3.44}$$

The macroions are treated as hard spheres and the interacting potential can be written as follows:

$$\beta U(x) = \begin{cases} \gamma/xe^{-kx}, & x > 1 \\ \infty, & x < 1 \end{cases} \tag{3.45}$$

where $\beta = 1/k_bT$. $\gamma e^{-k} = \epsilon\psi_0^2$ can be identified as contact potential between two ions in units of k_BT (this expression is true for $k \lesssim 6$).
Finally, using closure relations:

$$c(x) = -\beta U(x), \quad x > 1 \tag{3.46}$$

$$h(x) = -1, \quad x < 1 \tag{3.47}$$

the structure factor follows from the Fourier transform of the OZ equation

$$S(K) = 1/\left[1 - 24\phi a(K)\right] \tag{3.48}$$

with the volume fraction ϕ of the proteins in solution and the dimensionless quantity $K = qd$. $a(K)$ is a rather complicated term depending on K and the details can be found in the original publication. [130] The free fitting parameters are ϕ, the ionic strength in the system I, the charge Z and the effective diameter of the protein d. These values are linked to the structure factor by the following equations:

$$\phi = \frac{\pi n d^3}{6} \tag{3.49}$$

$$\gamma = \frac{z_m^2}{(2+\kappa d)} e^{\kappa d} \tag{3.50}$$

with n as the density of macroions in solution and the charge valency $z_m = Z \cdot e$.

Examples of structure factors and the effect of the two most interesting quantities for the present study are given in Figure 3.8. Here, the diameter d and the volume fraction ϕ are set at fixed values of 50 Å and 0.02, respectively. The influence of effective charge Z of the proteins in solution is shown in the top figure, where a correlation peak evolves with increasing Z. This same peak (fixed to $Z = 40$ for the bottom panel) is suppressed by an

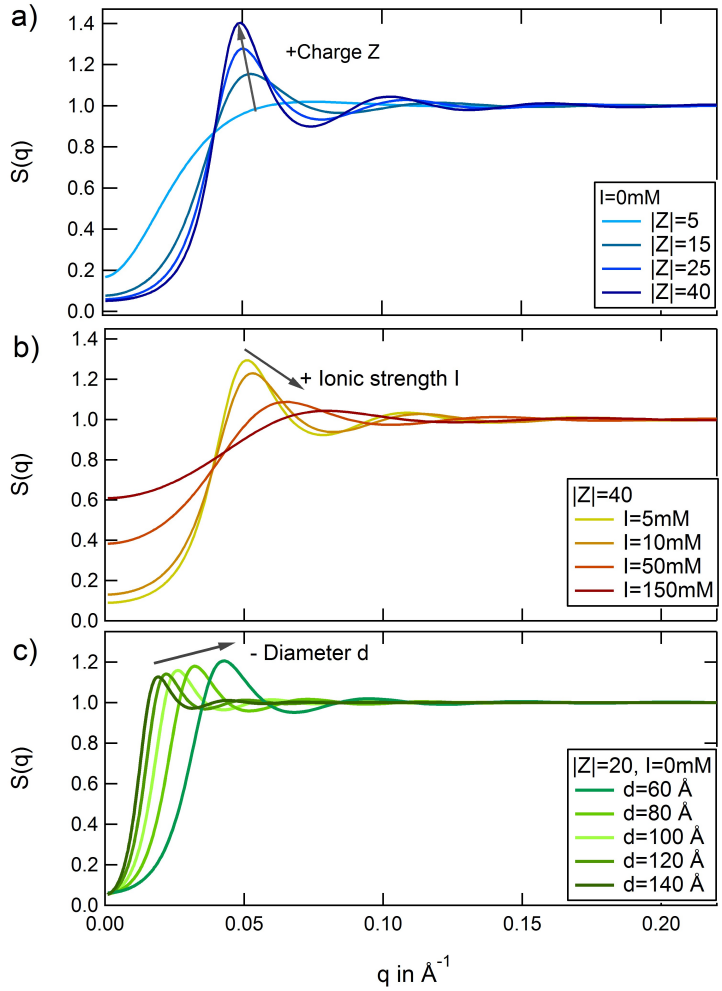

Figure 3.8: Effect of the parameters charge $|Z|$, ionic strength I and the diameter d on the Hayter Penfold structure factor (HPMSA). In (a) the increase of $|Z|$ from 5 to 40 is reflected in the increase of the first maximum. (b) High ionic strength (150 mM) leads to a decrease of the first maximum, as the interactions are screened. (c) A decrease of d from 140 Å to 60 Å shifts the first maximum to larger q, which equals smaller dimensions in real space.

increase of ionic strength. Moreover, the increase of ϕ will result in an increase and shift of the first peak towards higher q and inversely, the increase of d will shift the peak towards lower q values.

3.3.2.2 Guinier Law for dilute solutions

A general approach to characterize single particles in dilute solution without any prior knowledge of the shape or regularity of a particle, is given by the *Guinier Law*. In the limit of small q, the scattering function follows a certain universal form derived from the Taylor expansion of the form factor term e^{-iqR} and is described by:

$$I(q) \approx N(\Delta\rho V_p)^2 \exp\left(-\frac{1}{3}q^2 R_g^2\right) \tag{3.51}$$

The Guinier Law is valid for (i) scattering vectors $qR_g < 1.3$, (ii) a dilute system of independently scattering particles and (iii) an isotropic system of randomly orientated particles with centers of symmetry. The above equation allows the determination of the radius of gyration R_g of any particle and of the particle volume V_P as demonstrated in Figure 3.9. R_g gives the effective size of a scattering particle, irrespective of its geometry or shape.

The Guinier analysis is demonstrated on the example of scattering spheres with radius $R = 50$ Å in Figure 3.9. The inset shows the logarithm of the intensity $\ln(I(q))$ over q^2 and the Guinier regime is indicated by a dotted line. The slope of the linear fit using Equation (3.51), gives a radius of gyration $R_g = 38.9$ Å. In the present case of homogeneous spheres, $R_g = \sqrt{3/5}R$ is valid and well obtained by the fit.

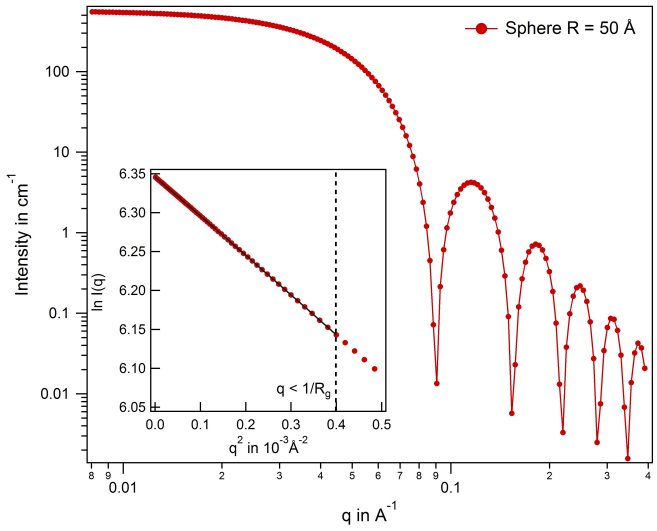

Figure 3.9: Theoretical scattering of spheres in solutions. The hardsphere form factor with $R = 50$ Å is plotted as an example for the Guinier analysis. The inset shows a linear fit for the Guinier regime of low scattering vectors in a $\ln(I(q))$ over q^2 plot.

The Guinier analysis is also a method to determine the forward scattering $I(0)$ of a sample and subsequently can be used to calculate the molecular weight of the protein, as the following holds:

$$I(0) = N(\Delta\rho V_p)^2 = \frac{c\Delta\rho^2\nu^2 MW}{N_A} \tag{3.52}$$

where c is the macromolecule concentration in g/cm^3, ν the specific volume and N_A the Avogadro's number.

3.3.3 Contrast variation

As briefly mentioned above, contrast variation is a powerful tool, first introduced by Stuhrmann and Kirste in 1965. [132, 133] The scattering length of the solution is varied, thus changing the contrast Δb of the scattering particles in the matrix. As a consequence, two border cases exist, namely infinite contrast ($\Delta b = \infty$) and vanishing contrast ($\Delta b = 0$). The scattering length density (SLD) function defined in Equation (3.38) can be replaced by an excess SLD function $g(r, \rho_s)$. This function is split into a term depending on contrast $\bar{\rho} - \rho_s$ and an independent term $\Delta\rho(r)$: [134]

$$g(r, \rho_m) = \Delta\rho(r) - \rho_s = F(r)[\bar{\rho} - \rho_m] + F(r)\delta\rho(r) \tag{3.53}$$

where $F(r)$ is the form factor as introduced in Equation (3.38) and $F(r)\delta\rho(r)$ describes the deviation of the particle's SLD from its mean value. The average SLD $\bar{\rho}$ is defined as:

$$\bar{\rho} = \frac{1}{V_p}\int_0^\infty F(r)\rho_p(r)dr \tag{3.54}$$

combining Equation (3.53) and (3.54), it is evident that:

$$\int F(r)\Delta\rho(r)dr = 0 \tag{3.55}$$

The total scattering intensity $I(q)$ is then calculated to:

$$I(q) = (\bar{\rho} - \rho_m)^2 I_S(q) + 2(\bar{\rho} - \rho_m)I_{SI}(q) + I_I(q) \tag{3.56}$$

where $I_S(q)$ is the scattering contribution of a particle for infinite contrast, $I_{SI}(q)$ is a cross term and $I_I(q)$ comprises inhomogeneities of the scattering length within a particle. An analogous Guinier analysis can be performed here for $q \to 0$ as in Equation (3.51). Equation (3.55) in conjunction with Equation (3.56) leads to: [135]

$$nI_0(q) = n(\bar{\rho} - \rho_{sol})^2 \cdot V_p^2 = \phi(\bar{\rho} - \rho_{sol})^2 \cdot V_p \tag{3.57}$$

with the Guinier approximation:

$$\frac{I(q)}{\phi} \approx n\Delta(\bar{\rho} - \rho_{sol})^2 \cdot \exp\left(-\frac{1}{3}q^2R_g^2\right) \tag{3.58}$$

where n is the number density of monodispersed objects in the solution and V_p the volume of that object. Thus, the volume fraction ϕ can be written as $\phi = nV_p$.

Furthermore, the radius of gyration R_g depends equivalently on contrast. Here, the radius of gyration at infinite contrast $R_{g,\infty}$ corresponds to the radius of gyration of the pure form factor $F(r)$. The dependency of R_g on the contrast for a centrosymmetric object is given by: [132, 136]

$$R_g^2 = R_{g,\infty}^2 + \frac{\alpha \cdot \bar{\rho}}{\bar{\rho} - \rho_s} \tag{3.59}$$

with

$$R_{g,\infty} = \frac{1}{V_p} \int_0^\infty F(r) r^2 dr \tag{3.60}$$

The coefficient α may be regarded as a measure for the spacial distribution of the inhomogeneity of the particle scattering length distribution. A positive value for α indicates a higher SLD in the periphery of the particle while lower on the inside, and vice versa for negative α values.

4 Experimental

4.1 Isothermal Titration Calorimetry (ITC)

Calorimetry is a sensitive technique to obtain thermodynamic information on binding affinity, enthalpy and entropy simultaneously. Practically all biomacromolecular interactions such as protein/ligand, protein/protein, and protein/nanoparticle are accompanied by heat exchange. Isothermal titration calorimetry (ITC) can very precisely monitor this change of heat under a constant temperature and adiabatic conditions in the range from $\sim 10^3 - 10^9$ mol^{-1}. The following Section discusses the basic principles of an ITC instrument and presents an overview of its strengths and weaknesses in comparison to other techniques that are employed to characterize ligand binding to proteins.

Experiments are performed using a VP-ITC instrument (MicroCal, GE Healthcare) by stepwise addition of a ligand solution into the cell containing the protein solution. A schematic representation of the ITC setup is shown in Figure 4.1. It consists of two identical and thermally conducting cells enclosed in an adiabatic jacket and a stirring syringe reaching into one of the cells. The ligand solution stored in the syringe is titrated subsequently under constant stirring into the sample cell filled with protein solution.

The two cells are made of a highly efficient thermal conductive material that is inert to many solvents. The sample cell has a working volume of 1.4 mL and the high-precision stirring syringe can hold 280 μL of reactant, which can be injected in steps of few μL under stirring at 307 rpm into the cell. Typical equilibration time intervals between each injection are $\sim 280 - 350$ s.

The heat evolved or taken up in the mixing process is then detected by the sensitive thermocouple circuits as a change of temperature compared to the reference cell, which is kept constant at a certain temperature. This temperature change is calibrated to power units and observed as a time-dependent input giving an incremental heat change $\mathrm{d}Q/\mathrm{dt}(Q')$ in μcal/sec. To keep the temperature of the sample cell constant relative to the reference cell, an either positive or negative change in the differential power (DP) feedback system is necessary, depending on the temperature change ΔT in the system. An exothermic process will for instance decrease the applied power, as heat is released and less power needed to keep the temperature constant. A titration peak after each injection is observed and drops back to a constant baseline after the system in the sample cell recovers equilibrium (Figure 4.2 top). The integral over time of each titration peak then gives the incremental enthalpy ΔQ of adsorption in cal/mol as a function of the molar ratio x between titrant

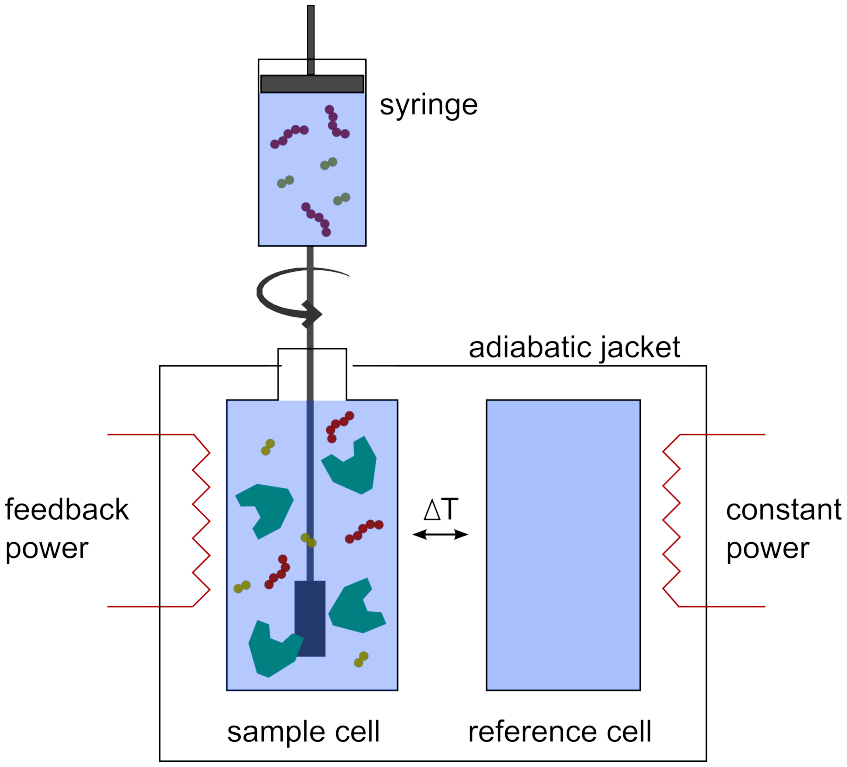

Figure 4.1: Schematic depiction of isothermal titration calorimeter (ITC). Screened from the environment by an adiabatic jacket are a sample cell filled with proteins and a reference cell containing pure millipore water. Both cells are highly thermally conducting, thus temperature can be precisely controlled and measured. A stirring syringe filled with ligand solution injects the titrant in steps of several μL into the sample cell under constant stirring. As interaction in the sample cell can cause either an exothermic or endothermic signature, the feedback circuit will adjust heating of the sample cell in order to maintain the reference temperature. The temperature difference resulting from such injection is then measured as difference to the reference cell by thermocouples. The direct observable signal of the ITC is the heat flow per unit of time dQ/dt.

and protein solution (see Figure 4.2 bottom).

Sample preparation and experiments were conducted as follows:
Stock solutions of 10 mM MOPS [1] buffer were prepared with pH 7.2 and according amounts of NaCl added to adjust ionic strength of the solution. These buffer solutions were used to prepare both protein and ligand solution and were also used for dilution experiments. For the polyacrylic acid (PAA), stock solutions of PAA were dialyzed for several days against buffer solution to match pH[2]. HSA was equally dialyzed and the concentration measured afterwards using UV-vis (see Appendix Figure 8.2). The dialysis-system used was the Float-a-Lyzer by Spectrum Labs with molecular weight cut-off (MWCO) of $500 - 1000$ Da

[1] MOPS: 3-(N-morpholino)propanesulfonic acid
[2] This procedure was used to avoid the necessity of adding too much salt and thus change the ionic strength of the ligand solution.

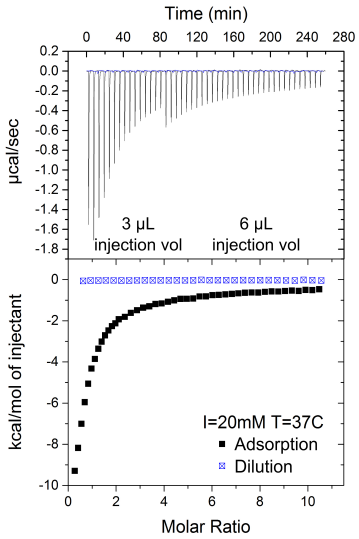

Figure 4.2: Raw ITC data on the example of IDS adsorption to HSA. Top panel shows titration peaks measured as heat flow over time dQ/dt in μcal/mol. Two injection volumes 3 μL and 6 μL are used in the present case to increase resolution at the critical part of the reaction. Blue lines are dilution measurements conducted by titrating IDS into according plain buffer solution. Bottom panel shows the integrated incremental enthalpy ΔQ divided by the moles of injected ligand where black symbols are adsorption and blue symbols dilution heats.

for PAA and MWCO 20 kDa for HSA, respectively. For the uremic toxins, minor amounts of NaOH was added to adjust the pH of the ligand solution to 7.2.

Prior to experiments, all samples were degassed for 10 min at the experimental temperature using the ThermoVac degassing and thermostatting station.[3] Samples were then thermostatted and the instrument stabilized for 1 h to ensure thermal equilibrium and stability of the system. Finally, a total of 298 μL ligand solution was titrated, using either two different injection volumes of 20 successive 3 μL followed by 36 successive 6 μL titrations for the uremic toxins or 70 successive 4 μL injections for the polyelectrolyte. The equilibration time interval between each injection was between $280 - 350$ s depending on the system.

For each set of condition, e.g. for a certain temperature and ionic strength, dilution of the ligands/polyelectrolyte were obtained by measuring the titrant heat when injected to pure buffer solution without protein. This heat of dilution was then subtracted from the according heat of adsorption. An example of such an experiment for IDS adsorption to HSA is shown in Figure 4.2, where black lines and symbols represent the adsorption and blue the dilution experiment. After correction, the resulting binding isotherm is fitted using the ITC module of the Origin® 7.0 software supplied by Microcal. [126] The fitting algorithm is described below and the models applied for analysis are described in detail in Section 4.1. An overview of the experiments performed at the VP-ITC is shown in Table 4.1.

4.1.1 Challenges and pitfalls of ITC

In an ITC measurement, the shape and quality of the isotherms are influenced by the choice of experimental conditions and especially sensitive to absolute concentrations of protein

[3] This step is important, as bubbles during the titration can distort the measurement.

Table 4.1: Overview of ITC experiments. Ionic strengths were adjusted by adding according amounts of NaCl to 10 mM MOPS buffer solution at pH 7.2.

System	Ionic strength in mM	Temperature in K	c(HSA) in mM	c(ligand) in mM
PAA + HSA*	20; 50	298; 300.5; 303; 306; 310	0.02	0.5
	70; 100	310	0.02	0.5
PhAA + HSA*	20; 150	298; 303; 310	5.88	0.015
	50; 70; 100;	310	5.88	0.015
PhAA + HSA-Urea	20; 150	298; 303; 310	5.88	0.015
IDS + HSA*	20; 150	298; 303; 310	1.99	0.015
IDS + HSA-Urea	20; 150	298; 303; 310	1.99	0.015

* HSA without further specification relates to native HSA while HSA-Urea relates to urea modified HSA as specified in Section 8.1 of the Appendix.

and ligand. The optimal concentrations depend on the mechanisms of binding and the binding affinities K_b. A quantitative way to approximate the shape is given by the following equation:

$$c = NK_b[P]_{tot} \tag{4.1}$$

where N is the number of ligands bound to protein, K_b the binding affinity and $[P]_{tot}$ the total concentration of protein in the cell. Figure 4.3 demonstrates different shapes of isotherms depending on the choice of concentrations and thus the effect of the parameter c. [137] As the simulated curves demonstrate, both too large or too small values for c

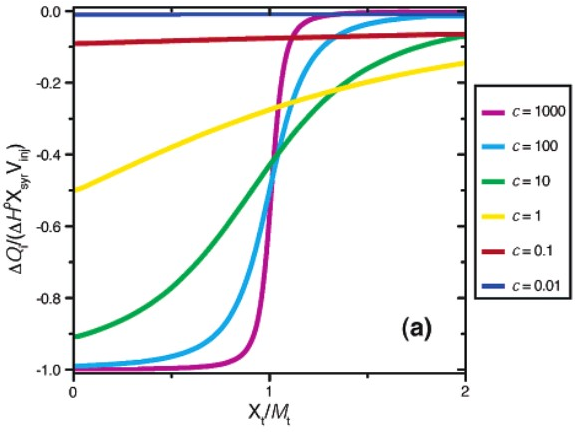

Figure 4.3: The shape of simulated ITC curves with varying parameter c. Adapted from [137].

will lead to increased errors in ΔH_{ITC} and K_b in the fitting procedure. ΔH_{ITC} is well

defined if a plateau is measured, as in cases of $c < 50$. Furthermore, an accurate fitting of the binding constant K_b requires $c < 500$, because only then enough data points are measured to describe the curvature of the inflection point. Thus, an ideal ITC experiment is carried out using concentrations matching c values between 50 and 500. However, some systems cannot fulfill this requirement, as is the case with PAA. As will be shown in the following, the dilution heat of PAA is exceptionally large, such that experiments can only be performed at low concentrations. As a consequence, concentrations for HSA are equally low to reach an equilibrium at the end state of the experiments.

The heat of dilution of the ligand into buffer solution can in some cases deviate from the simple case, where it shows only a small and constant heat contribution independent of molar ratio. For a more complex case, the heat of dilution ΔH_{dil} depends on an activity coefficient of the i-th solute γ_i: [138]

$$\Delta \mathrm{H}_{dil} = \sum_i \upsilon_i RT \ln \gamma_i \left(1 + \frac{T \partial \epsilon}{\epsilon \partial T}\right) \tag{4.2}$$

where υ_i is the stoichiometric coefficient and ϵ the permittivity. For dilution of PAA, the amount of heat generated after each injection is non-constant, as the activity coefficient for already dissolved ions changes with each titration of ligand. Moreover, water-related effects such as solvation and reorganization of water upon PAA dilution can lead to varying of ΔH_{dil} with molar ratio. A typical measurement of PAA titration in plain buffer solution at

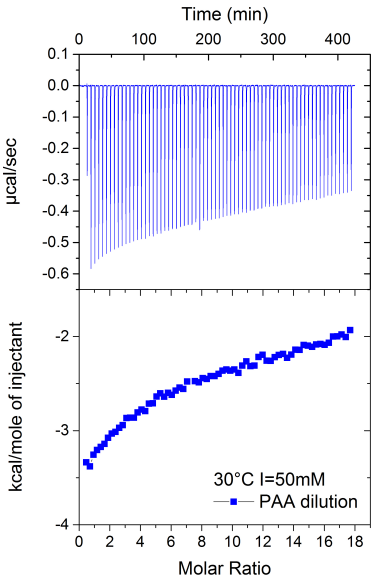

Figure 4.4: Raw ITC data of PAA titration into buffer solution at 30 °C and I = 50 mM.

30 °C and I = 50 mM is shown in Figure 4.4. The heat of dilution for PAA was measured at all conditions separately and subtracted from the heat of adsorption to obtain reasonable isotherms of binding.
However, the concentrations of the protein and PAA are small and the evolved heat will be concomitantly small. Hence, all effects leading to spurious heat signals must be considered

in detail and carefully excluded. The main problem is the adjustment of the same pH and ionic strength in both the solution of the protein and of the polyelectrolyte. This is done by extensive dialysis which turned out to be decisive for obtaining meaningful ITC-data.

A further aspect that can influence the measured isotherm, are structural changes of the protein induced by ligand binding. Unfolding or reorientation of the secondary structure of a protein will be accompanied by an enthalpy change and falsify derived binding affinities. Furthermore, the stability of the protein and the complex formed are important prerequisites to fulfill the thermodynamic equilibrium condition. Aggregation and dimerization of proteins under e.g. certain pH or high ionic strength will give an extra ΔH_{ITC} and thus influence the fitting of K_b.

4.2 Small-angle neutron scattering (SANS)

This chapter resumes the basics of neutron scattering experiments and fundamental concepts required to follow the interpretation of the performed experiments. The used instruments are briefly presented through the example of the SANS instrument V16 [139], located at the BER-II facility at Helmholtz-Zentrum Berlin (HZB), Germany and the D11 located at the Institut Laue-Langevin (ILL) in Grenoble, France. [140] For detailed information on instruments and experimental details, the reader is referred to the homepage of the institutes. [141–143]

Neutrons are uncharged spin-1/2 particles with a magnetic moment of $\mu = -1.923$ nuclear magnetons. As such, they interact directly with the atomic nucleus (via the strong nuclear force) and via a magnetic moment. The range of the nuclear force is orders of magnitude smaller than the neutron wavelength and therefore the scattered wave is isotropic with its amplitude being proportional to the so-called scattering length b. The value of b does not only depend on the element but also on its isotope and the spin-state of the neutron-nucleus system. In the absence of a theory for nuclear forces b is an experimentally determined quantity. Depending on their energy, neutrons can be classified as hot, thermal or cold. Their average energy corresponds to about k_BT with temperatures between 6000 K $-$ 1 K, respectively. Neutrons can be described either classically as particles with a mass of $m = 1.675 \cdot 10^{-27}$ kg or via the *de Broglie* equation with a wavelength λ of:

$$\lambda = \frac{2\pi}{|\mathbf{k}|} = \frac{h}{m|\mathbf{v}|} \tag{4.3}$$

and a wavevector $|\mathbf{k}|$, a velocity $|\mathbf{v}|$ and the *Planck constant* h. The energy E of a free neutron is:

$$E = \frac{1}{2}mv^2 = \hbar\omega = hv \tag{4.4}$$

$$= \frac{\hbar^2 k^2}{2m} = \frac{h^2}{2m\lambda^2} \tag{4.5}$$

Neutrons used for structural investigations by SANS usually have a wavelength in the range $3 - 10$ Å, corresponding to the magnitude of the particle of interest. Thus, they belong to

the class of cold neutron. Some of the biologically relevant elements and their according scattering lengths of both neutrons and X-rays are listed in Table 4.2 for comparison.

Table 4.2: Scattering lengths and cross sections for X-ray and cold neutrons of biologically relevant elements. [129, 144]

Elements	Atomic number	b_{coh} in 10^{-12} cm	σ_{coh} in 10^{-12} cm	σ_{inc} in 10^{-24} cm^2	$b_{\text{X-ray}}$ in 10^{-12} cm^2
^{1}H	1	−0.374	1.76	79.9	0.38
^{1}D (^{2}H)	1	0.667	5.59	2.04	0.38
C	6	0.665	5.55	<0.01	0.168
N	7	0.936	11.01	0.49	0.197
O	8	0.580	4.23	<0.01	0.225
P	15	0.513	3.31	<0.01	0.423
S	16	0.285	1.02	<0.01	0.450

Neutrons: b_{coh} coherent scattering length
σ_{coh}, σ_{inc} coherent and incoherent scattering cross section
X-Rays: $b_{\text{X-ray}}$ scattering length for small angles

4.2.1 SANS instruments

Neutron experiments were performed at the SANS instruments V16 and V4 of the Helmholtz-Zentrum Berlin's BER-II reactor in Berlin, Germany [139, 143, 145], at the KWS-II of the FRM-II reactor at the Maier-Leibnitz Zentrum (MLZ), Garching, Germany [141] and at the D11 of the Institut Laue-Langevin in Grenoble, France [142]. While the details of each instrument can be found at the according websites of the institutes, the following chapter intents to briefly summarize the basic principles and also differences between a time-of-flight (TOF) instrument and a monochromatic instrument. Thereby, the main focus will be to elucidate the general instrument design of the V16, as the principles underlying all instruments are similar.

The V16 employs the TOF method to take advantage of a broad spectrum of neutrons. [139] In contrast to monochromatic instruments that use velocity selectors, a combination of choppers is used at the V16 to tune the width and range of the continuous neutron flow from the reactor. A scheme of the instrument V16 is shown in Figure 4.5, where the neutron beam first reaches the four choppers with flexible rotation frequencies and maximum speed of 3000 rpm. The chopper configuration can be adjusted to the individual needs of an experiment in terms of wavelength band of the neutrons. In experiments, where the q-resolution plays a minor role, a setup with a broad neutron band, high flux but lower resolution $\Delta q/q$ between 5 % − 18 % can be chosen.

After the last chopper, a low efficiency detector, the monitor, is installed to detect the count rate of incoming neutrons for data normalization. Afterwards, the neutrons pass a standard collimation system with adjustable distances up to 12 m. Before reaching the

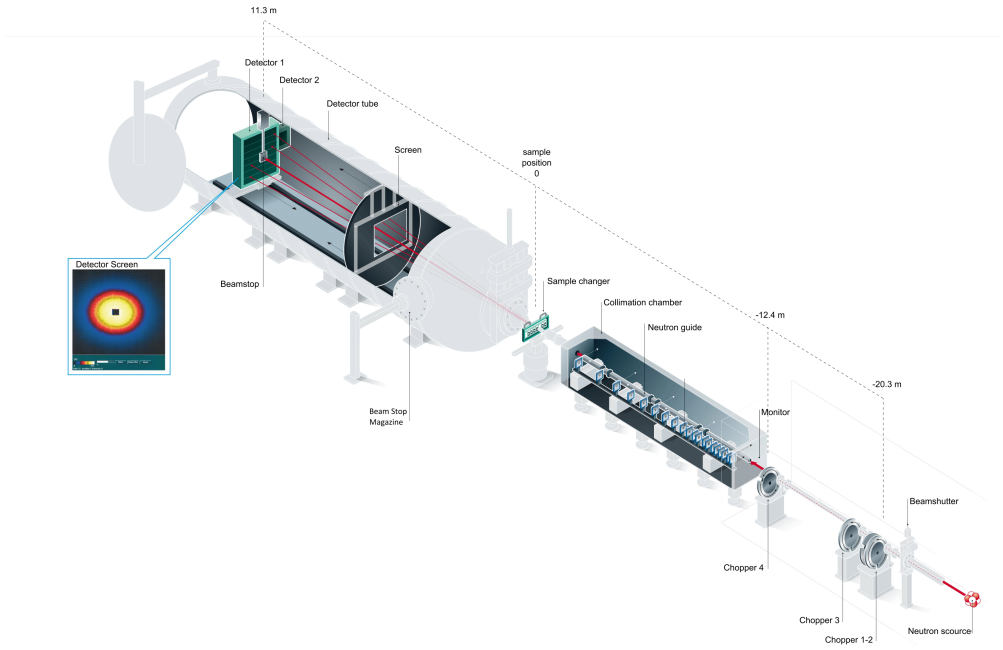

Figure 4.5: Schematic depiction of the instrumental set-up of V16. Adapted from [143].

sample, the neutrons pass an aperture of 40×40 mm to reduce divergence of the beam and to increase q accuracy. After being scattered by the sample, the neutrons pass an evacuated detector chamber with a 2D ^{3}He detector with an area of 100×100 cm^2. The detector can be moved along the beam direction to achieve sample-to-detector distances of $1.7 - 12$ m and thus covering different spatial angles. A combined choice of detector distance and wavelengths between 2.5 Å $\leq \lambda \leq 18$ Å gives access to a q range between 0.002 Å$^{-1} - 0.8$ Å^{-1}.

A monochromatic instrument follows very much the same layout as the TOF instrument described above. However, these instruments only uses one wavelength with a certain distribution $\Delta\lambda/\lambda$ depending on the instrument. The neutrons are mono-chromatized by a velocity selector, which consists of a rotating drum with helically curved absorbing slits at its surface. The desired wavelength or equivalently the velocity of neutrons is determined by choosing the appropriate rotation speed similar to the working principle of choppers. An overview of instrumental settings for experiments performed at different beamlines is listed in Table 4.3.

4.2.2 Primary data reduction

The 2D signal measured by the detector has to be corrected in many steps and averaged over the whole azimutal angle to obtain a normalized differential cross section usable for data analysis (see Section 3.3.1). A detailed description of the extensive data reduction can be found in [146, 147]. However, a rough overview of the reduction steps are presented in the following as key points:

Table 4.3: Overview of experimental setups for all experiments performed at different instruments.

Detector distance in m	Collimation in m	Frequency in rpm (ϕ in °) Chopper 1	Chopper 3	Chopper 4	$\lambda_1 \pm 10$ % in Å	$\lambda_2 \pm 10$ % in Å
Instrument V16 @ HZB, Berlin						
1.7	6	3000 (0)	3000 (−5)	3000 (−90)	1.8	3.2
12	12	770 (0)	770 (−3)	770 (−50)	2.8	8
Instrument V4 @ HZB, Berlin		Selector frequency in rpm			$\lambda \pm 10$ % in Å	
1	2	21000			4.5	
1	2	28300			6	
8	4					
Instrument KWS-II @ MLZ, Garching					$\lambda \pm 10$ % in Å	
1.12	8	- - - -			5.27	
3.73	8					
5.73	8					
19.73	20					
Instrument D11@ ILL, Grenoble		Selector frequency in rpm			$\lambda \pm 10$ % in Å	
1.2	4	28070			4.6	
8	8					
1.2	4	12910			10	
8	8					

V16: Chopper 2 was not used for all experiments, ϕ denotes the phase shifts
KWS2: The selector velocity is unknown

1. Determination of the beam center.
2. Creation of a detector mask to avoid beam-stop effects or border effects of the detector.
3. Normalization for incoming flux measured by the monitor.
4. Transmission correction.
5. Subtraction of not experimental related signals (e.g. electronic noice, background radiation). For this, scattering and transmission are measured using an absorber material for neutrons like boron carbide (B_4C).
6. Subtraction of scattering form the sample vessel (usually quartz cuvette).
7. Radial averaging.
8. Normalization to absolute intensity. Taking advantage of the fact that water scatters predominantly incoherently and thus uniformly over the whole q-range, it is used as reference measurement.
9. Rebinning to constant q-spacing according to specific requirements of the data.

Finally, the absolute scattering cross section independent of instrumental and experimental set-up $\frac{d\sum}{d\Omega} = I(\mathrm{cm}^{-1})$ is obtained. These reduction steps are carried out using the free software MANTID [148] with an internally developed algorithm. [139]

4.3 Simulation methods

Computer simulations were performed by X. Xu from the group of Prof. Dr. J. Dzubiella. The following chapter shall give a brief overview of the conditions of the simulation and according parameters used. Details can be found in [149].

4.3.1 Computer simulation model and parameters

To model the interaction between polyacrylic acid and HSA, Langevin dynamics simulations were employed using an implicit-water coarse-grained (CG) model. [150] Similar methods have been used repeatedly to study e.g. protein folding [151] and the pair potential [152] between proteins. Each amino acid of the protein, PAA monomer, and salt ions is explicitly represented by a single interaction bead, while the water is implicitly modeled by a dielectric background continuum.

The protein sequence for the HSA is provided by PDB database [4]. [153] The native structure of the protein is maintained by a Go-model like force field. [154, 155] All beads corresponding to basic and acidic amino acids are assigned with a positive or negative charge, depending on their dissociation state at physiological pH = 7.4, resulting in a net charge of HSA of $-1e$. The short polyelectrolyte chain is modeled as a flexible sequence of $N_{\mathrm{mon}} = 25$ freely jointed beads with a radius σ_{LJ} and an electric charge of $-1e$. The PAA monomers are connected by a harmonic bond potential and the flexibility of the PAA chain is defined via a harmonic angle potential. The dynamics of the beads is governed by Langevin's equation of motion. [156] Coulomb interactions govern the electrostatic pair potential between all charged beads.

One HSA and several PAA chains are simulated in a cubic box with side lengths of $L = 30$ nm and periodically replicated walls to generate a quasi-infinite system in the canonical ensemble. For the continuous water background, a static dielectric constant is set to $\epsilon_r = 73.4$ and 78.2 for temperatures $T = 25$ °C and 37 °C, respectively. Molar ratios $x = c_{PAA}/c_{HSA}$ ranging from 1 to 10 were simulated to elucidate the effect increasing PAA chains in the solution. Salt concentration c_{salt} range from 20 to 100 mM to compare with experimental conditions.

4.3.2 Binding and free energy calculations

The stoichiometry that is the average number of bound PAA chains on one HSA, can be determined through a calculation of the normalized density distribution function $g(r) =$

[4] PDB ID=1N5U

$c(r)/c_{PAA}$, where r is the distance between the centers-of-mass (COM) coordinates of the HSA and PAA and c_{PAA} is the PAA bulk concentration. Integration of $g(r)$ leads to the PAA coordination number

$$n(r) = 4\pi c_{PAA} \int_0^r g(r')r'^2 dr'. \tag{4.6}$$

which describes how many PAA chains are bound on average at a distance r. To quantify the number of bound and released ions upon complexation, the average number of ions N_i, $i = \pm 1$ bound (*condensed*) to the PAA chain or to the positive protein patches, is count respectively. An ion is defined as 'condensed' if it is located in the first binding layer, with a cut-off distance $r_s = 0.5$ nm from the charged bead, thus double-counting in overlapping volumes is avoided. The number of released ions is obtained by a comparison before and after PAA/HSA association.

The potential mean force (PMF) between HSA and PAA was calculated using steered Langevin Dynamics simulations. [150] Here, the center of mass of the PAA is restrained in space by an external time-dependent force. This force is applied as a constraint, i.e. harmonic potential, and moved with a constant pulling velocity v_p to steer the particle in the prescribed direction (see Figure 4.6). [157] The binding affinity of the PAA can be defined as the free energy value at the global minimum of the PMF in the stable complex.

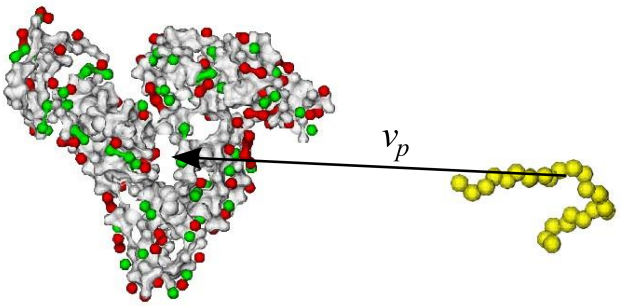

Figure 4.6: Simulation snapshot of a pulling experiment with velocity v_p. The amino acid beads of HSA is illustrated as a transparent surface plot where neutral beads are colored white, positive and negative beads are green and red, respectively. PAA is represented as a yellow string of beads.

However, before making a comparison with the experiment, it has to be taken into consideration that ΔG_b^{exp} provided by the experiment is defined as a standard free energy, which refers to the standard binding volume $V_0 = 1/C^0$ of one liter per mol. [158] Hence, the standard binding free energy from the simulation can be obtained as:

$$\Delta G_b^{sim} = \Delta G^{corr} + \Delta G^{sim}, \tag{4.7}$$

with a term $\Delta G^{corr} = -k_B T \ln(C^0 V_b)$ that is the entropy correction arising from the accessible volume of the COM of the PAA in the bound state.

5 Interaction of polyelectrolyte with HSA

The first part of this thesis presents the interaction between the model polyelectrolyte polyacrylic acid (PAA) and HSA from a thermodynamic and structural point of view. The binding is analyzed experimentally by varying ionic strength and temperature as crucial parameters that influence the interaction. The results obtained by ITC are then compared to computer simulations of the same system. In a second part, spatial studies on the PAA-HSA complex are conducted by detailed characterization of the pure protein solution to observe possible structural changes upon complexation.

5.1 Thermodynamic analysis of binding

A systematic series of ITC experiments was performed, comprising four ionic strengths and five different temperatures ranging from room temperature (25°C) to the physiological temperature (37°C) in buffer solution of pH 7.2. All experiments were performed with PAA solution as injectant that was titrated into the protein solution in the cell.

Figure 5.1 displays the raw ITC-signals of PAA onto HSA (black lines and points) as well as the heat of dilution of PAA (blue lines and symbols). The signal is weakly endothermic at I = 20 mM but exothermic at I = 50 mM (see Figure 5.1a) and b). Dilutions are in all cases exothermic and the effect becomes stronger with increasing salt content as expected (blue curves and points). For higher ionic strength, the heat of dilution has a dominant effect on the overall signal and determines the sign of the signal at I > 20 mM. For data analysis, the heats of dilution are subtracted from the heats of adsorption prior to fitting. Attention must be paid to this step, as for some cases a constant residue remains after subtraction of the heat of dilution. Even though this offset signal is very small and usually less than 0.1 kcal/mol, it cannot be neglected due to the small overall heat. This offset can be assigned to a slight mismatch of the pH or salt between the titrant and the solution in the cell. In order to take this effect into account, a flat background was fitted to all isotherms after the first step of subtraction and used to correct the data in the second step.

The panel on the right-hand side of Figure 5.1 displays a set of typical results obtained. Evidently, the heat of adsorption is positive and is found for all conditions under consideration here. Hence, the driving force for the process of adsorption must be entropic. This point will be discussed in more detail below and is well borne out from the simulations, too.

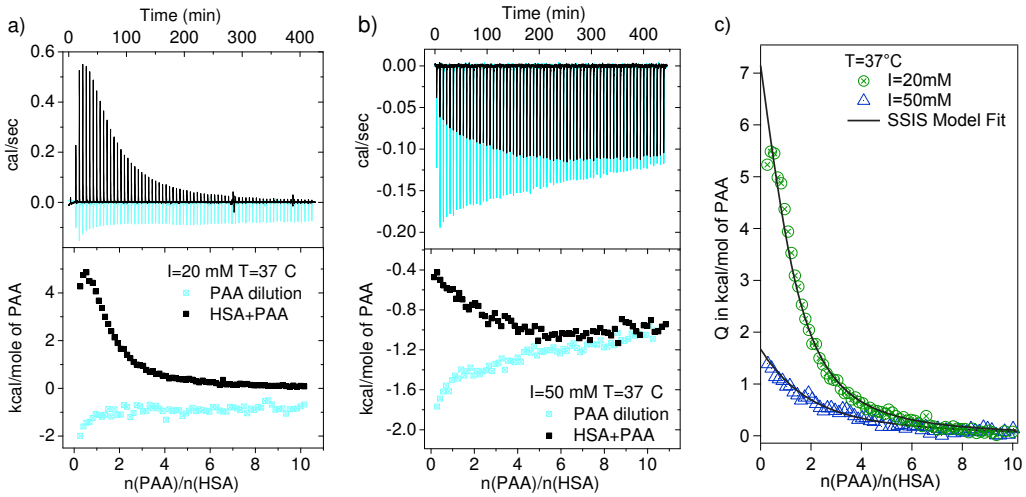

Figure 5.1: ITC data of binding of PAA to HSA at pH = 7.2, T = 37 °C and a) I = 20 mM, b) I = 50 mM. Top panels show raw titration peaks of adsorption (black lines and points) and dilution (blue lines and symbols) of PAA and bottom panels show corresponding integrated heats as a function of molar ratio n(PAA)/n(HSA). c) Binding isotherm corrected for the heat of dilution at 37°C and I = 20 mM (green circles) & 50 mM (blue triangles) with corresponding fits (black line). Reprinted with permission from [149]. Copyright 2015 RSC Soft Matter.

In order to obtain the number N of PAA-molecules bound to one HSA-molecule, the data were first fitted using the SSIS model as described in Section 3.2.1 and the algorithm described in Section 4.1. The binding number N, binding affinity K_b and the overall enthalpy change measured ΔH_{ITC} can be obtained by fitting the isotherm. Figure 5.2 shows a comparison of the parameter N for the two data sets as in Figure 5.1. The colored curves showing different fixed values of N reveal that the data clearly justify $N = 1$ as the best choice for fitting. This observation is true for any other data sets. Deviations from $N = 1$ are not significant and $N = 1$ can safely be assumed in all subsequent analysis. This leaves only K_b and ΔH_{ITC} as free fit parameters and thus giving reliable results for both parameters.

5.1.1 Strength of interaction as a function of temperature

Figure 5.3a) and (b) each presents a series of measurements conducted at two ionic strengths I = 20 mM and 50 mM to study the dependence of binding on temperature. For better clarity, only three temperatures are displayed in these graphs. The data for two more temperatures are displayed in Figure 5.3c) and (d). The data taken at both ionic strength reveal a significant increase of enthalpy with increasing temperature from 25°C to 37°C. This effect is more pronounced for I = 20 mM than at I = 50 mM.

Additionally, the overall enthalpy of adsorption becomes weaker with increasing salt content, which points directly to the importance of electrostatic interaction on the binding of PAA

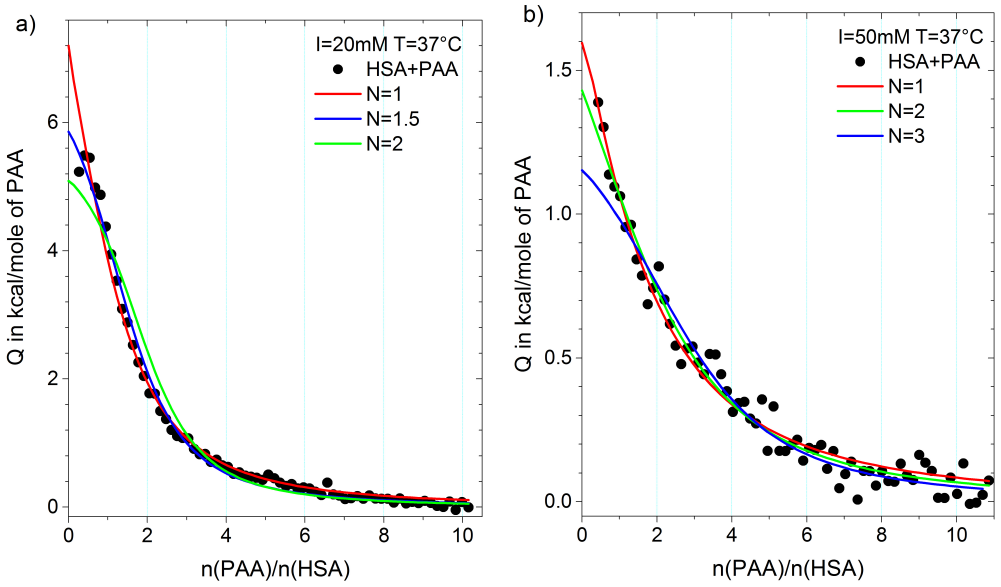

Figure 5.2: Determination of the parameter N, i.e., the number of PAA molecules adsorbed on HSA molecule is shown for one temperature $37°C$ at a) I = 20 mM and b) 50 mM. Each line shows a fit with different values of fixed N marked by different colors. Reprinted with permission from [149]. Copyright 2015 RSC Soft Matter.

onto HSA. All data are very well described by the model assuming $N = 1$. Data taken at higher salinity are more noisy but the raise of the signal with temperature is clearly discernible. Since there is no plateau in the ITC signal, the parameter ΔH_{ITC} might be overestimated by the fits.
The results of these fits are listed in Table 5.1 with ΔH_{ITC} and K_b as fit parameters, N being fixed to unity (see above). The free energy of binding ΔG_b was calculated from the fit parameter K_b using Equation (3.20).

The strength of binding as a function of temperature can now be analyzed according to van't Hoff's law (see Equation (3.26) in Section 3.2.3). Figure 5.4 shows the resulting van't Hoff plot. A linear correlation between logarithm of the binding constant K_b and the inverse temperature is seen within the limits of errors. The binding enthalpy ΔH_b can be obtained from the slope of the linear fit and ΔS_b from the intercept. The resulting data are gathered in Table 5.1. In general, the values of ΔH_{ITC} are larger than the data resulting from the van't Hoff analysis. Similar findings have been made in a recent study of the interaction of proteins with charged microgels. [159] Reasons may be sought in additional processes as e.g. the hydration of freed counterions that are not directly coupled to the process of binding (see below). Also, the heat of adsorption taken directly from the ITC data might be slightly overestimated (see above).

In literature, the distinction is usually made between an "observed" or "apparent" enthalpy measured by the ITC, defined as ΔH_{ITC} in the present thesis and the van't Hoff enthalpy

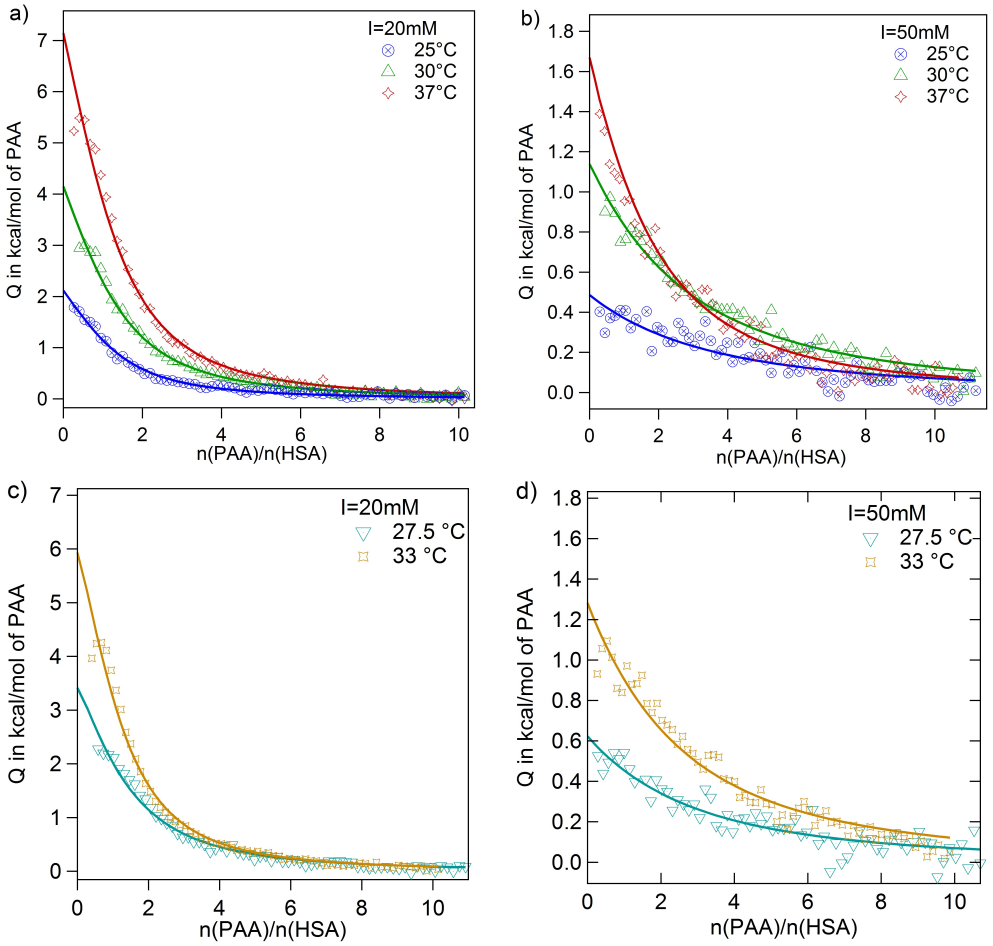

Figure 5.3: Effect of temperature. The integrated heats Q for adsorption of PAA on HSA at temperatures of 25°C, 30°C and 37°C and the corresponding fits are displayed at the top panels for (a) I = 20 mM and (b) I = 50 mM. For better clarity, isotherms at 27.5°C and 33°C are displayed separately in the bottom panel for (c) I = 20 mM and (d) I = 50 mM. Reprinted with permission from [149]. Copyright 2015 RSC Soft Matter.

ΔH_b determined by the temperature variation of K_b as described above. [160–162] The frequently observed difference between both enthalpies cannot only be attributed to a lack of experimental precision as in some distinct cases [163, 164], but may persists beside proper error propagation. This finding is demonstrated on a standard ITC test reaction, namely the complexation of Ba^{2+} with 18-crown-6 ether. [161] In a study on this system, Mizoue and coworkers evaluated different assumptions of error and concluded that the discrepancy between ΔH_{ITC} and ΔH_b are statistically significant. [161] Other authors likewise believe that additional effects, not directly associated with binding, contribute to ΔH_{ITC}, such as buffer ionization and protonation effects of proteins. [124, 159] Furthermore, the linkage of buffer interactions with binding can result in nonconventional and nonlinear ΔH_b profiles,

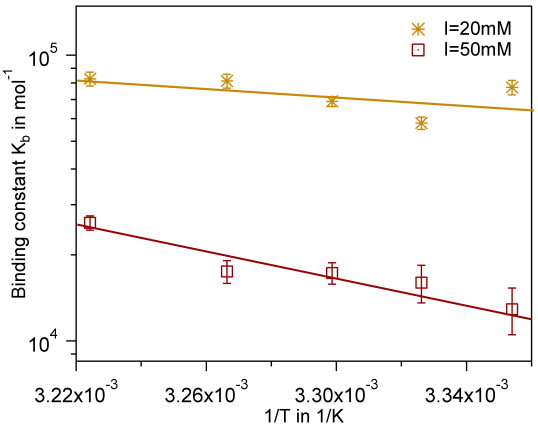

Figure 5.4: Van't Hoff analysis of the dependence of the adsorption constant on temperature. Data points are derived from the fits of the ITC-data shown in Figure 5.3a) and b). The crosses correspond to I = 20 mM and the open squares to I = 50 mM.

thus complicating data analysis. [124, 164] The proton transfer reaction can be written as follows: [165]

$$\Delta H_{ITC} = \Delta H_b + n_{H+}\Delta H_{ion} \tag{5.1}$$

where ΔH_{ion} is the heat of ionization of the buffer and n_{H+} either the number of protons taken up ($n_{H+} < 0$) or released ($n_{H+} > 0$). This enthalpy becomes apparent, when the same two interaction partners are placed in different buffer solutions. [159] The effect of ionization and more specifically protonation is moreover experimentally observed by Niedzwiecka et al. as a constant discrepancy between ITC enthalpy and van't Hoff enthalpy. [166] Further unspecific heat contributions such as conformational changes, can additionally add to the heat measured by ITC, hence it is reasonable to define a residual heat ΔH_{res}, which links ΔH_{ITC} and ΔH_b: [56]

$$\Delta H_{ITC} = \Delta H_b + \Delta H_{res} \tag{5.2}$$

An alternative to the simple approach of assuming $\Delta C_p = 0$ is to fit ΔC_p and $\ln K_b$ using Equation (3.24) and then take this value into account when estimating a temperature dependent ΔH^0_{vH} as given by Equation (3.25). The data shown in Figure 5.3 are thus reevaluated and a representative fit is shown exemplarily for each ionic strength at one temperature (298 K) in Figure 5.5a). After obtaining the new van't Hoff enthalpies ΔH^0_{vH} at each reference temperature T_0, the values are compared to measured enthalpies ΔH_{ITC} as depicted in Figure 5.5b).

The recalculated van't Hoff enthalpies ΔH^0_{vH} are in accordance with ΔH_{ITC} within the limits of error for low temperatures (see Figure 5.5b). The difference ΔH_{res} of recalculated enthalpies at 298 K, for instance, have decreased to ≈ -6 kJ/mol, compared to ≈ -30 kJ/mol for the standart van't Hoff analysis. For increasing temperature, the uncertainties are rather large and more experiments in smaller temperature steps are necessary to obtain a more reliable fit than shown in Figure 5.5a). For the low ionic strength however, the discrepancies between fit and data $\ln K_b$ are too large and yield non-physical results.

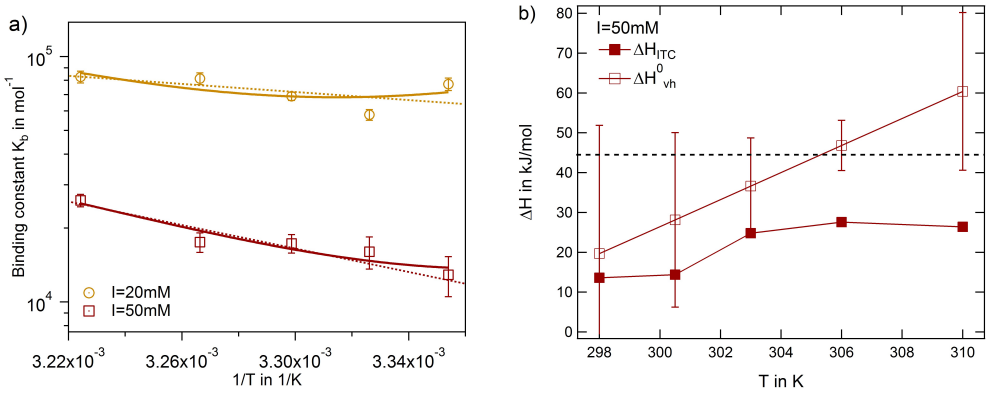

Figure 5.5: Reevaluated van't Hoff analysis assuming nonzero Δc_P. (a) The new fit (solid line) uses Equation (3.24) to reevaluate the data from Figure 5.4 with $T_0 = 25°C$ as reference temperature (fits with other reference temperatures do not deviate significantly from the shown one). The linear van't Hoff fit from Figure 5.4 is shown for comparison as dashed lines. (b) According van't Hoff enthalpies were calculated for each temperature as T_0 using Equation (3.25) (open symbols) and compared to measured enthalpies ΔH_{ITC}. The dotted line marks the enthalpy calculated by the simple van't Hoff Equation (3.26).

5.1.2 Dependence on ionic strength

To study the dependence of the binding process on ionic strength, two more experiments at 37°C and I = 70 mM and 100 mM were conducted (raw data are shown in Figure 8.8 in the Section 8.3 of the Appendix). With increasing ionic strength, the measured enthalpy approaches zero and the ITC method reaches its instrumental limits. As described above, the parameter N was fixed for both salt concentrations to unity. Table 5.1 gathers all data obtained from these experiments.

The data exhibit a very consistent decrease of binding constant K_b with increasing salt concentration (see Table 5.1). This observation combined with the fact that only about one PAA molecule is adsorbed on the HSA leads to the conclusion that the driving force of the interaction is an attractive electrostatic potential between the negative PAA with patches of positive charge on the surface of HSA molecule. As discussed in Section 3.1.3, these patches are known to act as multivalent counterions for the polyelectrolyte and binding between PAA and such a patch thus leads to a release of its counterions. [54, 115, 159] A linear relationship between the logarithms of binding constant and salt concentration was considered many years ago by Record and Lohman (see Equation (3.28)). [117] This behavior is observed for the present data as well if the ionic strengths is above 20 mM (see Figure 5.6). Application of Equation (3.28) to the data in Figure 5.6 yields $\Delta n_{ion} \approx 2.9 \pm 0.5$, that is, approximately 3 ions are released upon binding of one PAA-molecule to a HSA molecule. The deviation from linearity for low ionic strength has been observed as well by Dubin et al. for the interaction between Bovine Serum Albumin and the polyanion Heparin at pH 6.8. [55] Here, electrostatic interactions become long-ranged and the relative contributions

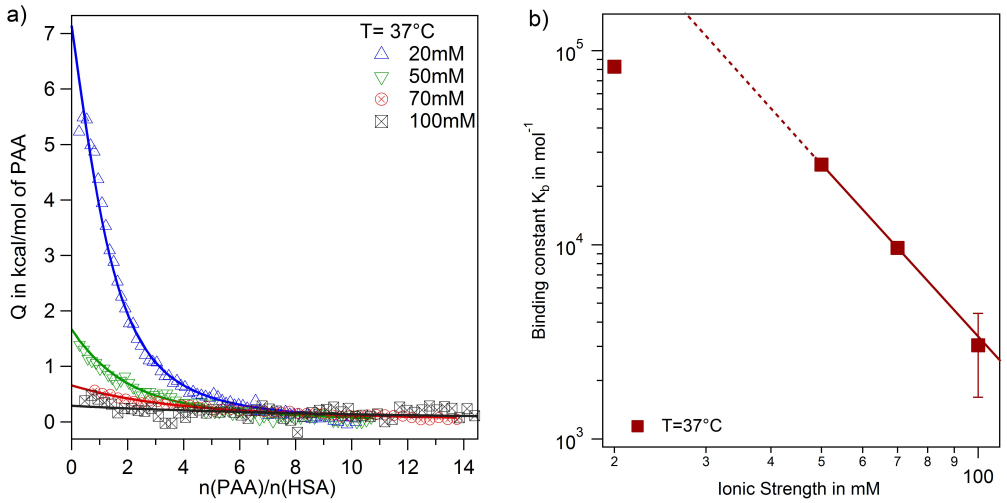

Figure 5.6: Effect of ionic strength. (a) Isotherms are shown for a series of ionic strengths ranging from I= 20 − 100 mM at 37°C. All fits have been done with $N = 1$. (b) Linear dependence of the binding constant versus ionic strength as listed in Table 5.1 are depicted in logarithmic scales according to Equation (3.28). [117] Reprinted with permission from [149]. Copyright 2015 RSC Soft Matter.

of the counterion release mechanism significantly decrease.

Extrapolation of the linear fit reveals that interaction still persists at physiological ionic strengths and temperature. At I = 150 mM and 37°C, a finite binding free energy of around -17 kJ/mol can be derived from the plot and it only decays to small values at around 750 mM. This concentration has been found to be necessary in dialysis to remove protein-bound uremic retention solutes. [30] Evidently, there is still some binding under physiological conditions and much higher salt concentrations are needed to remove the toxins from the surface of HSA. These results show also that ITC-experiments can be deceptive when enthalpies of different reaction in the system compensate in such a way that they vanish. Thus, in the present case interaction still exists under physiological conditions but does not lead to measurable enthalpies.

5.1.3 Comparison to theoretical modeling of binding

Implicit-water, coarse-grained (CG) and structure-based computer simulation are presented in the following to gain additional insight, such as kinetic information on the binding between polyelectrolyte and protein that can not be obtained by ITC alone. This type of simulation provides a full microscopic picture of the interaction of PAA with HSA, in particular the identification of the sites where PAA docks on. Moreover, the simulations can be used to obtain realistic free enthalpies of binding as will be further shown below.

The computer simulations demonstrate that HSA binds only one PAA chain, independent of temperature, salt concentration, and molar ratio in the considered parameter ranges.

Table 5.1: Overview of thermodynamic parameters for all fitted isotherms for the temperature series between 25°C-37°C and ionic strengths between I = 20 mM - 100 mM. As discussed in Section 3.2.1, all data were fitted with fixed $N = 1$. ΔG_b^{exp}, ΔS_b and ΔH_b were calculated according to Equation (3.20) and Equation (3.26) respectively. Entropy for 70 mM and 100 mM were calculated using Equation (3.21) at 37°C.

Ionic strength in mM	T in °C	ΔH_{ITC} in kJ/mol	$K_b \cdot 10^4$ in mol^{-1}	ΔG_b^{exp} in kJ/mol	ΔS_b in kJ/mol/K	ΔH_b in kJ/mol
	25	16.4±0.3	7.7±0.5	-27.9±1.3		
	27.5	32.8±0.6	5.8±0.3	-27.4±1.4		
20	30	34.0±0.5	6.9±0.3	-28.1±1.1	0.17±0.01	15±4
	33	45.6±0.9	8.1±0.5	-28.8±1.6		
	37	53.4±1.0	8.3±0.5	-29.2±1.5		
	25	13.6±1.1	1.3±0.2	-23.4 ± 0.5		
	27.5	14.4±0.9	1.6±0.2	-24.2 ± 0.3		
50	30	24.8±0.7	1.7±0.1	-24.6 ± 0.1	0.27±0.02	44±8
	33	27.6±0.9	1.8±0.2	-24.9 ± 0.2		
	37	26.4±0.6	2.6±0.1	-26.2 ± 0.1		
70	37	21.9±0.7	1.0±0.1	-23.6 ± 0.5	0.12 (37°C)	
100	37	8.5±2.8	0.3±0.1	-20.7 ± 1.2	0.10 (37°C)	

Hence, it reconfirms the result obtained previously by ITC. A representative simulation snapshot of the bound complex with one PAA is presented in Figure 5.7. From a thorough screening of the simulation trajectories, it emerges that this is a highly reproducible and stable configuration which is assumed in 80 % of the simulation time. Figure 5.7b) reveals that the PAA chain spans the sub-domains II A, III A, and III B, involving the Sudlow II binding site. As expected for a negatively charged polyelectrolyte, it favorably binds to positively charged amino acids (highlighted as green opaque spheres in Figure 5.7b).

It is furthermore interesting to see the temporal evolution of the complex of HSA with PAA. The PAA chain slides along the Sudlow II site much in a way of a threading through an orifice. On the one hand, this fact demonstrates the strong binding of PAA by this side. On the other hand, the threading through this site leads to a strongly increased number of configurations of the complex and thus increases the entropy of the complex. This fact certainly leads to the binding of the PAA-chain at the Sudlow II site and not on other positive patches on the surface of HSA.

A further aspect that can be compared to experimental results is the binding free energy that can be determined through the free energy profiles (potential of a mean force) (see Sec-

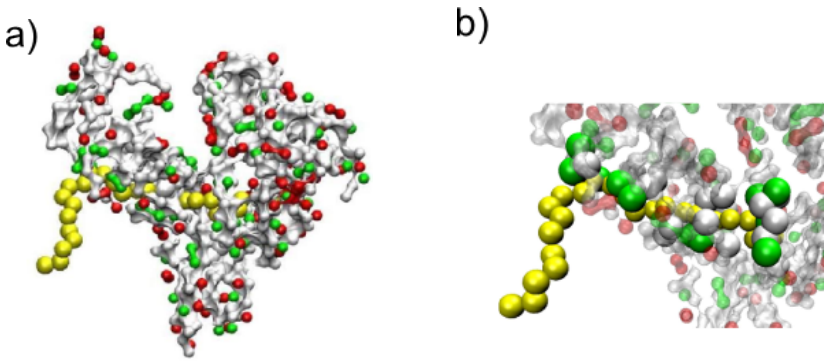

Figure 5.7: (a) Representative computer simulation snapshot of the total HSA-PAA complex. (b) Magnification of the binding site: the PAA (yellow string of beads) is bound near the Sudlow II site. The amino acid beads that directly participate in the binding (defined by being within 0.5 nm distance to the PAA on average) are depicted by the opaque spheres. The rest of the HSA structure is distinguished by a transparent surface plot. Electrostatically neutral HSA beads are colored white, positive beads are green, and negative beads are red. Reprinted with permission from [149]. Copyright 2015 RSC Soft Matter.

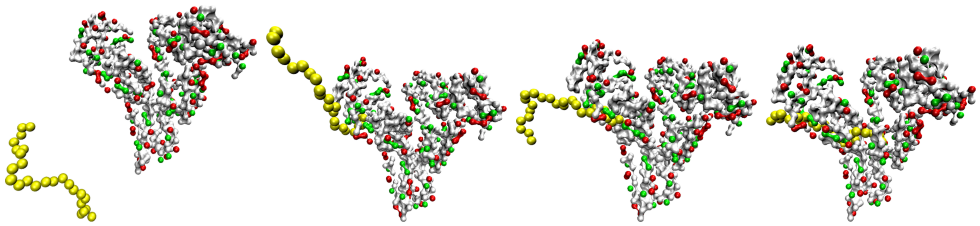

Figure 5.8: A series of snapshots depict the binding process.Reprinted with permission from [149]. Copyright 2015 RSC Soft Matter.

tion 4.3.2). Examples for this interaction free energy $G(r)$ between a single uncomplexed HSA and one PAA at two salt concentrations is presented in Figure 5.9 along the HSA-PAA distance coordinate. At about $r \simeq 6$ nm the onset of a strong attraction takes place until a global minimum is observed at closer approach at about $r = 2$ nm. Adsorption of a second PAA chain onto HSA is never observed in the simulations. This is due to a too strong monopole charge repulsion and the covering of the high-potential binding spot by the firstly bound PAA. The binding free energy ΔG^{sim} can be calculated from the difference of the global minimum and the reference free energy at large distances (horizontal lines in Figure 5.9).

The values of the simulation binding free energy, corrected to yield the standard free energy of binding from the simulations ΔG_b^{sim} (see Section 4.3.2), are summarized in Table 5.2 for various salt concentrations and temperatures. Good agreement is found for all systems and the same influence of salt and temperature are observed by simulations as by experiments. However, it is somewhat surprising that the highly quantitative description by simulations

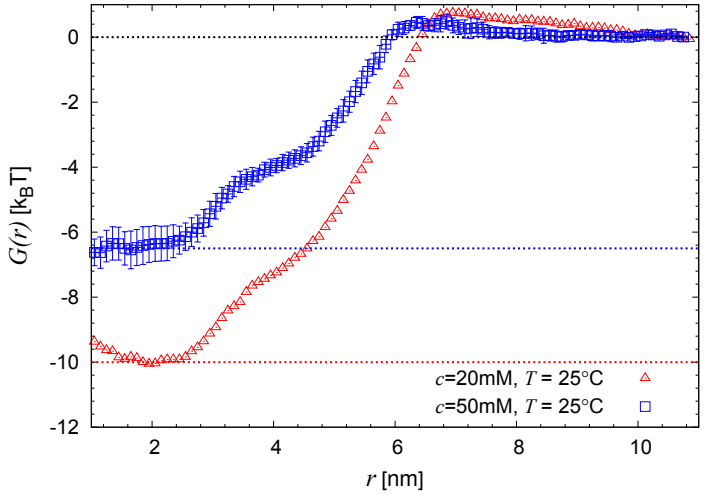

Figure 5.9: Free energy profile (or potential of mean force) $G(r)$ between the PAA and the HSA versus their centers-of-mass distance r at a temperature of 25 °C and for 20 mM (red) and 50 mM (blue) salt concentrations. The binding free energy ΔG_{sim} derived from the simulation can be read off as the difference between the zero free energy reference state at far separation (horizontal black dotted line) and the global minimum representing the bound state (horizontal blue and red dotted lines). Reprinted with permission from [149]. Copyright 2015 RSC Soft Matter.

Table 5.2: The calculated standard binding free energy from the simulations ΔG_b^{sim} in comparison with the experimental ones ΔG_b^{exp} for various salt concentrations and temperatures in units of kJ/mol. ΔG^{sim} is the direct output from the simulations which has to be corrected by ΔG^{corr} for the binding volume V_b to obtain the standard free energy of binding.

Conditions	ΔG^{sim} (kJ/mol)	V_b (nm^3)	ΔG^{corr} (kJ/mol)	ΔG_b^{sim} (kJ/mol)	ΔG_b^{exp} (kJ/mol)
20 mM, 25 °C	-24.8 ± 4.0	3.0	-1.5	-26.3 ± 0.5	-27.9 ± 0.2
20 mM, 37 °C	-25.1 ± 3.6	5.9	-3.1	-28.2 ± 3.6	-29.2 ± 0.2
50 mM, 25 °C	-16.1 ± 1.0	16.0	-5.7	-21.8 ± 1.0	-23.5 ± 0.5
50 mM, 37 °C	-18.9 ± 0.5	7.5	-3.9	-22.8 ± 1.5	-26.2 ± 0.2

coincide so well with experiments, given the simplicity of the underlying model and the neglect of hydration effects. While the results should be discussed with caution, they can be taken as a strong indication that relatively generic electrostatic interactions rule the complexation process and hydration contributions (such as hydrophobic or van der Waals (vdW) attractions) are rather small.

In order to access the contributions of the counterion release force as suggested by the experimental results, the number of released ions upon complexation is counted (Plot showing the number of ions versus distance is given in Figure 8.9 of the Appendix). An

ion is defined as condensed, if it is located in the first bound layer near a charged HSA or PAA monomer, with a cut-off radius of 0.5 nm (density profiles of positive salt ions around the PAA monomers are shown in Figure 8.10 of the Appendix). For a temperature of 25 °C and 20 mM and 50 mM salt concentrations, an average of 2.5 condensed ions are diluted away into the bulk upon complexation. This is indeed in good agreement with the Record-Lohman-analysis of the experiment data discussed above.
Deeper inspection shows that two of those ions come from the PAA, which leads to an average concentration in the bound state of $c_{dense} \simeq 1.5 \pm 0.5$ mol/l. This implies that a favorable entropy contributions of about $\simeq k_B T \ln(c_{dense}/c_s) = 4.3 \pm 0.4$ and 3.4 ± 0.4 $k_B T$ is gained per ion upon its release into 20 mM and 50 mM bulk concentrations, respectively. The total released free energies estimated by this analysis are thus roughly -21 ± 2 and -17 ± 2 kJ/mol for 20 mM and 50 mM salt, respectively, which is close to the binding free energies from both experimental data and simulations.

Hence, the binding of PAA is to a great part ruled by a counterion release mechanism and entropy. However, the matching of these numbers may be fortunate since other non-negligible interactions such as (repulsive) chain entropy, vdW attractions, and multipolar charge interactions beyond the bound ion layer (that is from screening ions), all present in both simulation and experiment, have been neglected in this simple counterion release concept. The present comparison with experimental data, indicates nonetheless that these contributions are of comparable magnitude and cancel each other out roughly for the present system.

5.2 Structural characterization of HSA in solution

The following Chapter addresses the question, whether polyelectrolyte adsorption to the protein has an impact on the protein native structure. SANS experiments clarify this question by comparing results from pure HSA measurements in solution with varying salt concentrations, to experiments on the PAA-HSA complex. Furthermore, different HSA samples were studied comparing size and molecular weight, namely (i) purchased HSA powder from Sigma-Aldrich, (ii) isolated HSA samples from healthy patients and (iii) isolated HSA from pathological patients, suffering form chronic kidney disease (CKD).

5.2.1 Data treatment and analysis

Prior to data analysis, SANS data have to be reduced and corrected by background scattering. While the basic reduction steps were presented in Section 4.2.2, the following chapter will briefly elaborate on the background subtraction procedure and the analysis of the corrected data by the ATSAS package[1].

The q-independent buffer solution scattering is subtracted to obtain otherwise invisible structural information of the protein. Representative raw neutron scattering data is shown

[1] ATSAS package is provided by the EMBL Hamburg and can be downloaded from [167].

in Figure 5.10a). A 4.7 g/L HSA solution in 10 mM MOPS buffer with 10 mM NaCl (brown symbols) and according buffer solution (blue symbols) are prepared in 100 % D_2O. As expected, the D_2O buffer solution scatters uniformly with an intensity of approximately 0.05 cm^{-1} as reported in literature. [144] At high q values, HSA scattering converges towards buffer intensities. Figure 5.10b) depicts the HSA scattering after buffer subtraction (brown circles). However, an incoherent scattering part is still seen in the data that is owing to hydrogen in the protein, which exchanges with the surrounding solution during solvation. [168] A constant value is fitted using the high q range of the data after the first correction step, as indicated by the dotted line, and the intensities were corrected for this value. The final result (green triangles) is compared to theoretical scattering intensities calculated from the crystal structure of HSA [2] (solid line).

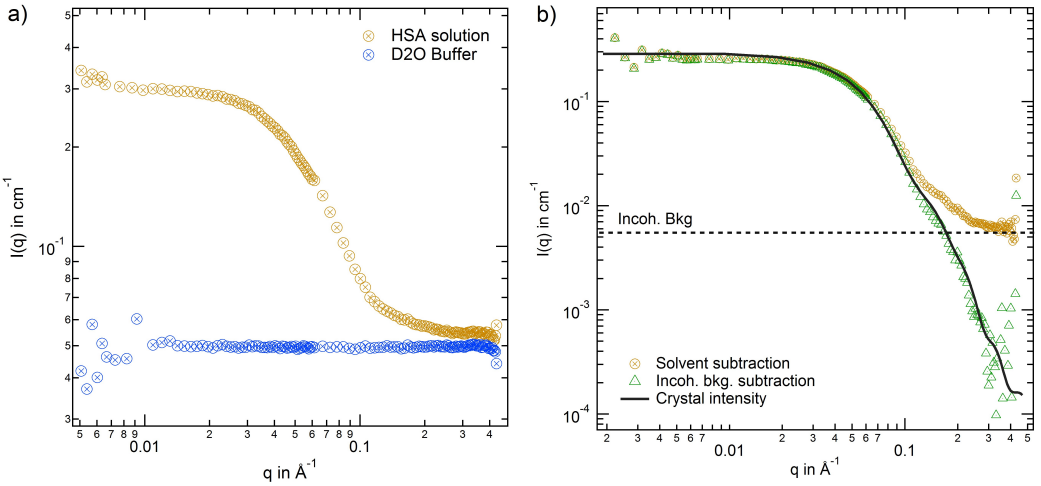

Figure 5.10: Background correction demonstrated on scattering of HSA in D_2O buffer solution. (a) Raw scattering data of 4.7 g/L HSA in buffer solution (brown) and buffer solution in D_2O with I = 20 mM (blue). (b) After subtraction of the buffer scattering from the HSA data (brown spheres), a constant incoherent background is fitted (horizontal dotted line), and subtracted from the solution corrected data. The result (green triangles) coincide well with a theoretical scattering curve calculated from the crystal structure of HSA (black solid line).

In the following, only solution background and incoherent background corrected data will be shown, following the same procedure as described above. For parts of the evaluation of scattering data from HSA, software from the program suite for SANS data analysis ATSAS, developed by Petoukhov et al., was used. [170] While the mathematical basics underlying the software are described in publications [171–173], the following section aims at describing the use of the specific software for the presented study.

[2] PDB ID: 1AO6 taken from [169].

Gnom [171] was used to calculate the particle distance distribution function $P(r)$ (PDDF) by an indirect Fourier transform of the intensity $I(q)$ to determine the radius of gyration, and the forward intensity $I(0)$ extrapolated to $q = 0$. The PDDF is defined as: [174]

$$P(r) = 4\pi \int_0^\infty I(q) \frac{sin(qr)}{qr} dr \tag{5.3}$$

Thus, using the full q-range, $P(r)$ can be an alternative to determine $I(0)$ and R_g (see Equation (3.51) and Equation (3.52) from Section 3.3.2) applying the following formalism:

$$R_g^2 = \frac{\int P(r) r^2 dr}{2 \int P(r) dr} \tag{5.4}$$

$$I(0) = 4\pi \int_0^{D_{max}} P(r) dr \tag{5.5}$$

These calculations rely on the assumption that $P(r = 0) = 0$ and on a good approximation for D_{max}, the maximum protein diameter. The quality of D_{max} crucially depends on the quality of the measured data. One criteria is $q < \pi/\mathrm{D}_{max}$ to accurately determine the largest dimension of the protein. [171]

Another useful software of the ATSAS package is CRYSON. This program evaluates neutron scattering intensities of a protein in solution with known atomic structure. [173] Crystallographic data of a protein (such as obtained from the protein database PDB [169]) typically determined by X-rays or NMR, is used to calculate scattering amplitudes. The hydration shell is taken into account by varying the border layer of solution scattering density, which can differ from bulk scattering density. Svergun et al. have shown with small-angle X-ray scattering (SAXS) experiments that the hydration shell has typically 1.05-1.25 times the density of bulk water. [173] Furthermore, theoretical curves can be calculated for different D_2O/H_2O fractions, as well as pre-deuteration of the molecule. For given SANS experimental data, the program can fit the theoretical scattering curve to measured data by smearing it, using the resolution specifications of the instrument and then minimizing discrepancy (chi-square value). More details on the software can be found in Section 8.2 of the Appendix.

5.2.2 Structure of native HSA in solution

HSA was dissolved in buffer solution using either PBS or MOPS as buffer and NaCl added as salt to adjust ionic strength. The reduction of the raw SANS data is described in Section 4.2.2 and henceforth, only the background corrected intensities in absolute units are shown. As described in Section 5.2.1, a set of tools from the SANS analysis software package ATSAS was used. In Section 8.2 of the Appendix, a more detailed description of the applied software is performed and the effect of different input parameters is analyzed. Following this analysis, Gnom and Cryson were applied to an example of actual scattering data of HSA in 25 mM PBS solution and the differences between the fit results compared.

In Figure 5.11a) experimental intensities of HSA in solution are evaluated against theoretically calculated data (blue line). Furthermore, two fitting approaches are compared: (i)

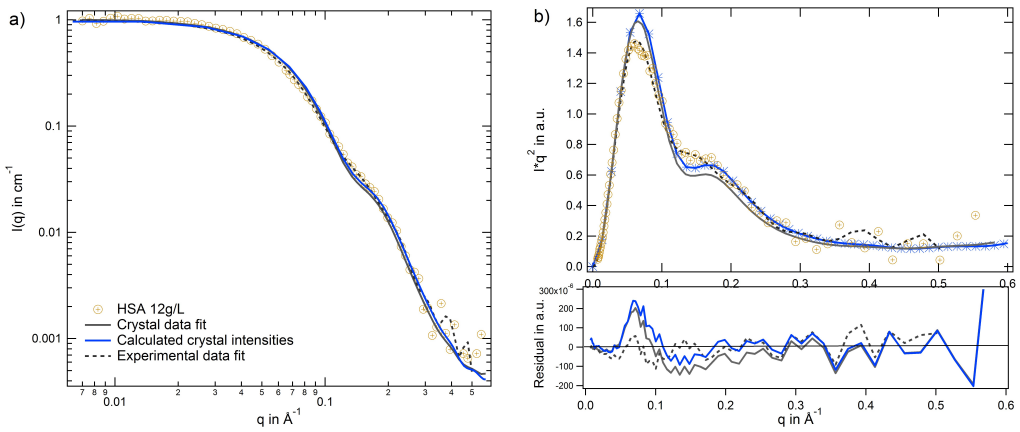

Figure 5.11: Comparison of different fit methods. (a) Experimental data of 12 g/L HSA in 25 mM PBS buffer solution is evaluated using different approaches and compared to theoretically calculated scattering data using crystal structure information (blue line). Grey solid line represents a fit by Cryson[173] and the dotted line is calculated using Gnom [171]. (b) Kratky plot of the profiles from the left panel with according residuals in the bottom panel.

the fit *Crystal-Data Fit* (grey line) is obtained using Cryson, while (ii) *Experimental Data Fit* is calculated using Gnom. Cryson smears the theoretical curves (blue line), using the resolution function to take the instrumental distortion into account. Also, it accounts for the hydration shell by surrounding the protein in solution with a border layer of variable scattering density. [173] As the differences are not clearly visible in the standard representation, a Kratky plot is shown in Figure 5.11b). $I(q) \cdot q^2$ is plotted over q and a typical bell-shaped peak followed by convergence towards the q-axis is observed for all curves. However, significant deviations of the experimental data to the cryson fit are evident.

The conclusion is that the structure of HSA in solution is indeed different to its crystal structure and not only an effect of instrumental smearing. This observation can reasonably be explained by the use of different techniques. To obtain crystal data, crystallization of the protein prior to measurement are necessary, which may alter its structure in comparison to the dissolved state. The best curve describing the data is the fit by Gnom, where no crystal data is used as an input. Thus, further evaluation of scattering data in the thesis is performed by Gnom.

The effect of different buffer and ionic strength on the structure of HSA in solution was studied and representative results are presented in Figure 5.12. Panel a) shows intensities of HSA for ionic strengths I = 20 mM and 150 mM and two different buffers MOPS and PBS. The inset exhibit PDDFs calculated using Gnom[3]. [171] The theoretically calculated intensity from crystal data is plotted as a dotted black line. Although the difference between each sample is not apparent in the standard intensity plot, it is marginally reflected in the $P(r)$ functions and in the first maximum of the Kratky plot (Figure 5.12b). However, these

[3]A more detailed explanation of the software is given in Section 5.2.1

findings are not systematically reflected in the radius of gyration R_g obtained by Gnom (see Table 5.3).

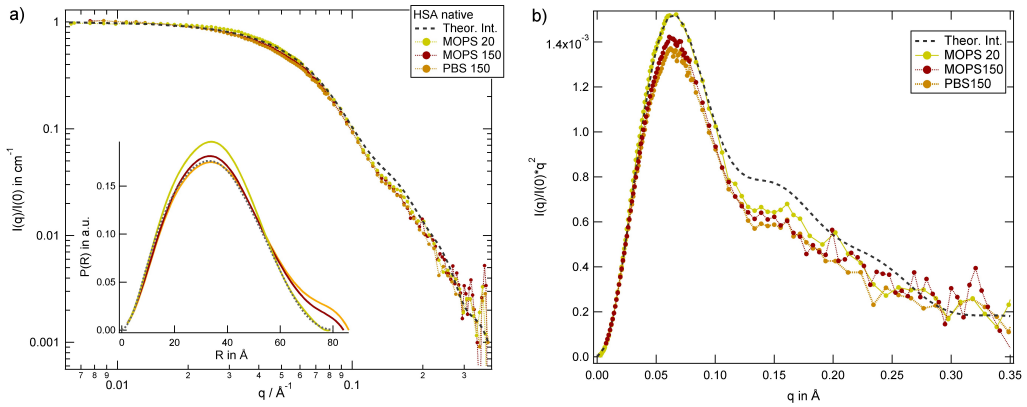

Figure 5.12: Comparison of native HSA in different buffer solutions with different ionic strengths. Dotted line is a theoretical intensity calculated from crystal data. The inset of a) shows PDDF profiles $P(R)$, which reveal a slightly different shape and D_{max}. (b) A difference between high and low ionic strength is also visible in the first maximum in the Kratky plot.

Nevertheless, this observation has been made by other authors, studying the structure of Bovine serum albumin (BSA) under different salts and ionic strengths. [168] While the authors interpret the impact of salt as negligible, the Kratky plot does exhibit similar features as in the present study (see Figure 5.13 bottom panel). [168] Thus, there are indications that a minor effect of salt concentration on the HSA structure in solution is present. These differences are, however, difficult to quantify as they are at the margins of resolution of the method.

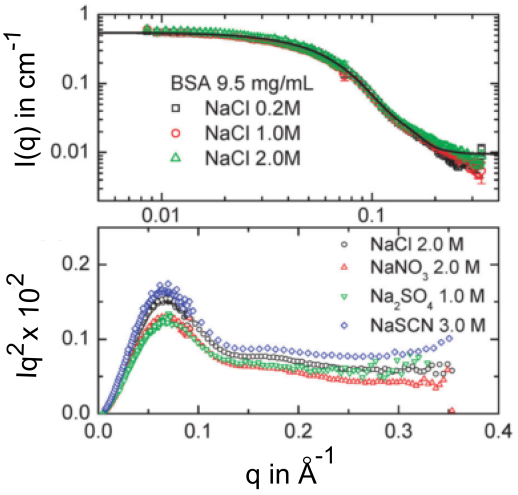

Figure 5.13: Scattering of BSA in solution adapted from [168]. Top panel shows BSA intensities measured at different NaCl concentration. Kratky plots of BSA profiles in the present of different salts and salt concentrations are presented in the bottom panel. A deviation in the first maximum can clearly be observed.

In general, both fit parameters I_0 and R_g obtained from the two different instruments are in good agreement, with an average value of ~ 27 Å. Leggio and coworkers have found in a

SAXS study, very similar values for a HSA of the purity > 96 % that is $R_g = 30.2 \pm 0.4$ Å. The derivation of 3 Å can be explained by the difference in protein, as the present study uses HSA with a purity > 99 %. Additional fatty acids adsorbed on the protein would lead to an increased R_g. While the values for I_0/ϕ are consistent, molecular weights (MWs) determined from the forwards scattering deviate significantly from the theoretical value of the HSA monomer (≈ 66.3 kDa). The calculation of MW, is proportional to the square of scattering length density contrast $\Delta\rho$ as seen in Equation (3.52), which in turn depends on the hydration state of the protein. When using D_2O as a solvent, H-D exchange will occur and the extent of exchange depends on protein concentration in solution. $\Delta\rho$ can vary between $3.59 \times 10^{10} - 3.30 \times 10^{10}$ cm^{-2} with increasing hydration of 90 % −70 %. The values given in Table 5.3 are calculated supposing roughly an average hydration of 80 %. The uncertainty given for MW in the table only accounts for errors in I_0 and protein concentration. Thus, it is difficult to determine MW of the protein from the SANS experiment, as also found by Zhang et al.. [168] Further studies on the state of hydration of HSA will be performed in the following.

Table 5.3: Overview of results obtained for native HSA scattering in solution. R_g and I_0 were obtained using GNOM. [171] MW was calculated according to Equation (3.52) The forward intensity I_0 in the last column is divided by the concentration and relative constant values as expected are obtained. A plot showing the relation between I_0 and concentration is given in Figure 8.5 in the Appendix.

Instrument	Buffer	I in mM	ϕ(HSA)±0.08 in %	$R_g \pm 0.8$ in Å	$I_0/\phi \pm 0.04$ in cm^{-1}	MW±1 in kDa
V16	PBS	25	1.15	27.2	0.63	46
	PBS	100	0.92	26.5	0.71	51
	MOPS	150	0.86	26.2	0.60	43
KWS-2	MOPS	20	0.36	26.7	0.71	51
	PBS	150	0.35	28.8	0.71	50
	MOPS	150	0.36	27.2	0.70	50

To summarize, the size and shape of HSA monomers in solution can be well characterized by SANS experiments. Deviations are observed between the crystal structure and HSA in solution. By closer inspection, the shape is weakly influenced by ionic strength and choice of buffer. R_g and I_0 are both reproducible quantities, where the first parameter reflects minor structural changes as induces by different salt concentration.

5.2.2.1 Contrast variation

By varying the D_2O to H_2O fraction, the scattering length density of the solution can be changed and thus different contrasts of protein to solvent $\Delta\rho$ is created. Inhomogenous domains within the protein with possibly different scattering lengths can then contribute

differently to scattering, depending on the protein. Basic principles of this technique are summarized in Section 3.3.3.
Contrast variation experiments were performed in buffer solutions containing native HSA at two ionic strengths 20 mM and 150 mM. Absolute intensities of scattering at ionic strengths 25 mM and 150 mM at three contrasts 100 %, 80 % and 70 % D_2O content are depicted in Figure 5.14 a) and b). Hereby, the intensities in Figure 5.14 b) are divided by corresponding volume fraction for better comparison of the data.[4]

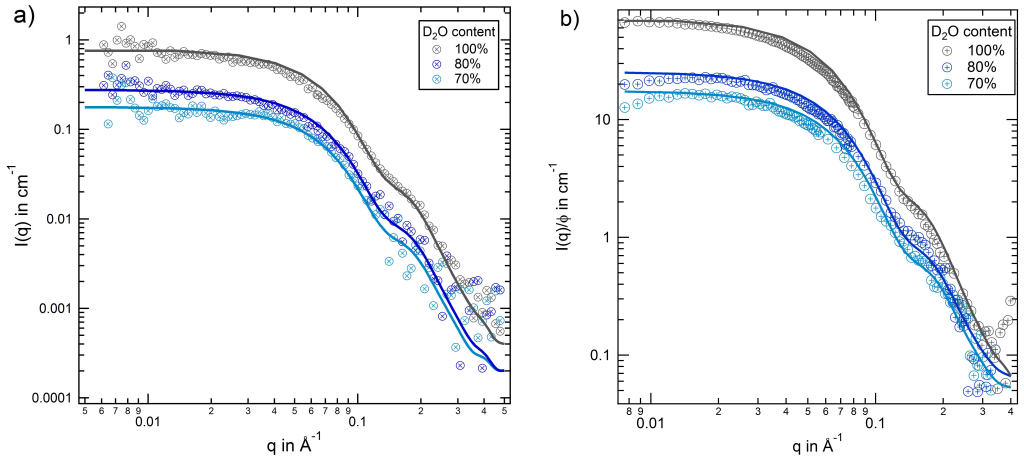

Figure 5.14: Series of contrast variation measurements of purchased native HSA in solution with I = 25 mM (a) and (b) I = 150 mM. D_2O/H_2O fractions vary from 100 % (grey), 80 % (dark blue), 70 % (light blue). Intensities in (b) are divided by corresponding volume fraction of HSA and theoretically calculated data using crystal structure [173] is scaled and plotted as lines on top for comparison. Derived values for $I(0)$ and R_g fitted by analyzing the Guinier regime are listed in Table 5.4.

The forward scattering intensity in both series of measurements changes with contrast, as expected (see Equation (3.57)). The calculated theoretical intensities by Cryson are plotted on top of the experimental data and show good agreement with the experiments. Further analysis by determining the forward scattering I_0 (see Guinier analysis Equation (3.51)) allow the calculation of the average scattering length $\bar{\rho}$ as defined in Section 3.3.3. Guinier fits are shown in Figure 8.6 of the Appendix and according results are listed in Table 5.4.

A plot of the squared $I(0)$ values with according sign of the respective contrast versus solvent scattering length density ρ_s allows the derivation of $\bar{\rho}$ and V_p (see Figure 5.15). The average contrast scattering length density is derived from the intersection of the fit with the x-axis and the particle volume from the slope according to Equation (3.57). Additionally, with the known density of the protein $\rho = 1.3$ g/cm^3, the molecular weight (MW) of HSA can be calculated from its particle volume by $\mathrm{MW} = \rho \cdot V_p N_A$. The fits for the two series of

[4] This step was not necessary for the I = 25 mM measurements, as all experiments were performed with the same HSA concentration of 12 g/L.

Table 5.4: Overview of contrast variation experiments performed on native HSA. Values R_g and I_0 are derived using GNOM [171].

Sample description	D_2O fraction	Buffer in mM	ϕ(HSA)±0.08 in %	R_g in Å	$I_0 \pm 0.02$ in cm^{-1}
HSA native*	100	PBS 150	0.35	28.8 ±0.5	0.25
	80		0.38	27.4 ±0.5	0.105
	70		0.42	25.8 ±0.7	0.067
HSA native†	100	PBS 25	0.92	27.2 ±0.5	0.85
	80	PBS 25	0.92	25.8 ±0.6	0.316
	70	PBS 25	0.92	24.4 ±0.8	0.168

Experiments were performed at KWS-2* and at V16†, respectively.

measurements at 25 mM and 150 mM are shown in Figure 5.15 and results for $\bar{\rho}$, V_p and MW are listed in Table 5.5

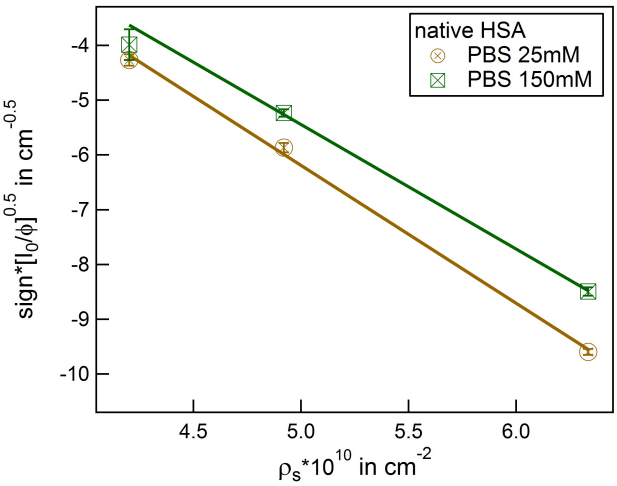

Figure 5.15: Analysis of the forward scattering in dependency on contrast. In the y-axis is plotted the square root of $I(0)$ derived by a Guinier fit shown in Figure 8.6 of the Appendix and normalized to respective volume fraction. According sign derived from the scattering length particle to solvent contrast is multiplied to the root of I_0. On the x-axis is plotted the solvent scattering length density ρ_s. A linear fit following Equation (3.57) yields average scattering length densities of $\bar{\rho}(I = 25\text{ mM}) = (2.58 \pm 0.15) \cdot 10^{10}$ cm^{-10} and $\bar{\rho}(I = 150\text{ mM}) = (2.60 \pm 0.18) \cdot 10^{10}$ cm^{-10} for 25 mM (brown) and 150 mM (green), respectively.

The average SLD $\bar{\rho}$ obtained for both ionic strengths are around $\sim 2.6 \times 10^{10}$ cm^{-2}. A theoretical SLD for HSA can be calculated and corresponds to 1.846×10^{10} cm^{-2}, not accounting for any H-D exchange. However, H-D exchange is a well known phenomena for proteins dissolved in D_2O [133], and there are 1048 exchangeable hydrogens in one

HSA molecule. [175] Upon solvation in D_2O, up to 90 % of them can be replaced by deuterium. [175] The SLD value obtained here would correspond to a theoretical H-D exchange of ∼60 %, which calculates to $\rho_{theo}(60\ \%) = 2.65 \times 10^{10}\ \mathrm{cm}^{-1}$. [176, 177] The particle volume derived from the fit however, is significantly lower than a calculated volume. Based on the primary sequence of HSA and its sum of constituent amino acid volumes, the theoretical volume is 81000 nm^3 and 20 % larger, than found in experiments. Accordingly, the MW values calculated by experiments of ∼ 50 kDa are significantly lower than theoretical MW (≈ 66.3 kDa) as also deduced previously in Section 5.2.2. Certainly, uncertainties in $\bar{\rho}$ are higher here, as only three contrasts were available for fitting. The present study is nonetheless comparable to results found by Zhang et al. in a combined SAXS/SANS study of BSA solution. Instead of using contrast variation, they deduced the size and SLD of BSA by fitting a form factor to single scattering intensities. A H-D exchange of ≈ 70 % and scattering particle volumes with about 13 % deviation from calculated BSA volumes were found. [168]

It is further known that the radius of gyration also depends on contrast, as discussed in Section 3.3.3. Stuhrmann et al. have shown that the radius of gyration $R_{g,\infty}$ at infinity contrast can be determined by contrast variation. [132, 133] In Figure 5.16 is depicted a Stuhrmann plot with a linear fit according to Equation (3.59). A linear dependence of the square of R_g on contrast is indeed observed and the fits yield $R_{g,\infty} = 29.2 \pm 0.9$ Å and $R_{g,\infty} = 32.2 \pm 1$ Å for 25 mM and 150 mM, respectively. These values are slightly larger than the experimentally found radii at maximum contrast of 28.8 Å and 27.2 Å.

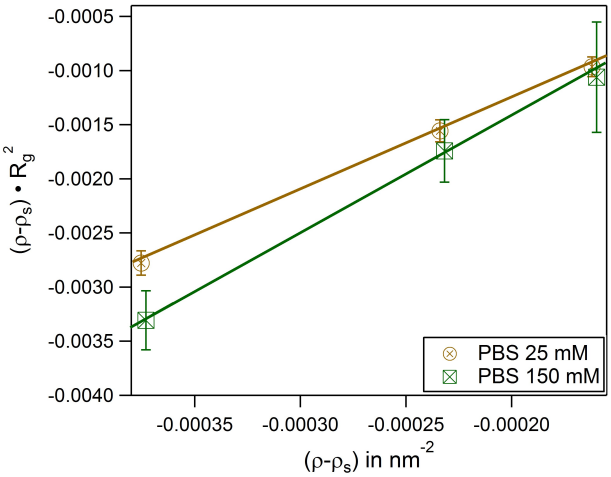

Figure 5.16: Stuhrmann plot of the two contrast series of HSA in solution with I = 25 mM (brown) and I = 150 mM (green). A linear fit using Equation (3.59) was performed and the according $R_{g,\infty}$ obtained are listed in Table 5.5.

In conclusion, minor difference in size, MW and SLD of HSA in 25 mM and 150 mM is seen in the performed experiments. However, the deductions obtained here contain relatively

Table 5.5: Fit parameters derived from $I(0)$ analysis in Figure 5.15 and the Stuhrmann plot in Figure 5.16.

Ionic strength in mM	Average SLD $\bar{\rho}$ in 10^{10} cm^{-2}	Particle volume V_p in nm^3	MW in kDa	Radius $R_{g,\infty}$ in Å
25	2.58 ± 0.15	65.000 ± 5000	51 ± 2	29.2 ± 0.9
150	2.60 ± 0.18	52.000 ± 5000	49.8 ± 2	32.2 ± 1

large errors and more experiments at different contrasts are necessary to improve precision of the obtained values. The extend of H-D exchange of the protein in D_2O solution could be determined to 60 %, which is similar to what has been found for BSA. [168] In general, all results are in accordance with expected parameters of HSA known from the crystallographic structure and a deviation from such structure after solvation is thus reasonable.

5.2.3 Structural investigation of patient HSA

Another interesting aspect to study with regards to the clinical question of how the pathological condition of patients influence the albumin structure is addressed by SANS. The aim was to investigate whether HSA isolated from pathological patients suffering from chronic kidney disease (CKD) is modified in a structural way in comparison to samples obtained from healthy control patients. Thus, proteins were isolated from different subjects and additionally compared to purchased samples under different ionic strength conditions.

Scattering intensities of isolated HSA samples obtained from healthy control patients and pathological patients, suffering from CKD, are plotted in Figure 5.17. The intensities of the samples were divided by $I(0)$ (obtained from a fit by GNOM, see Section 5.2.1) for better comparison. Native HSA sample in solution is plotted as a reference (brown line). Two control samples C-A and C-B were isolated from different healthy individuals (green circles and triangles). All samples referring to CKD patients originate from HSA isolated from the same pathological patient, including the complexed HSA sample with 1 g/L PAA.

The main observation here is made for the low q-regime, where scattering of all profiles differ significantly from the intensity scattered by the purchased HSA sample. An upturn of intensity is especially pronounced for the CKD sample at I = 20 mM (blue) and for the complexed HSA-PAA sample (violet). As the scattering profile at intermediate and high q still follows the native HSA profile, it is save to assume that the form of the protein is unchanged. Thus, the upturn in the low q range points towards larger particles in the solution. A possible explanation is the existence of agglomerations of HSA in solution. The magnified view on the low q-regime in Figure 5.17b) reveal that the difference to native HSA is more pronounced in the pathological samples (blue symbols) rather than the control samples (green symbols). Thereby complexation with PAA does not seem to have an additional effect on the pathological HSA samples.

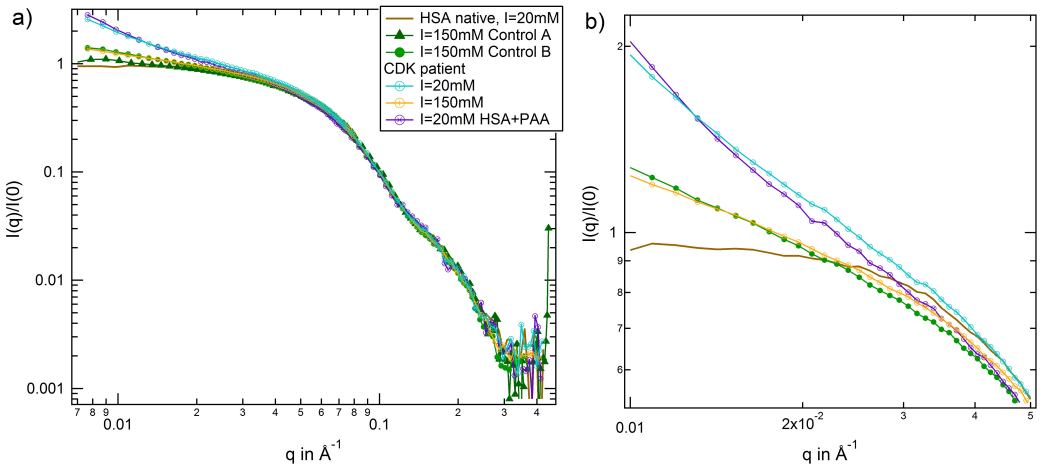

Figure 5.17: Scattering intensities of HSA isolated from pathological CKD (open blue and yellow circles) and healthy control patients (full green circles and triangles) at different ionic strengths are shown. Control A and B were obtained from two different healthy individuals. Scattering profile from purchased HSA at 20 mM ionic strength is plotted as a comparison (brown line). One complexed HSA-PAA sample using HSA from CKD patient is shown for I = 20 mM (open violet circles). All intensities were divided by their forward scattering intensity $I(0)$ for better comparison. Panel (b) shows a magnified view of the scattering in low q-range.

All scattering data were fitted using Gnom to determine the radius of gyration R_g and results are summarized in Table 5.6. The R_g values obtained from the control samples C-A and C-B coincide well within the limits of error. In the case of pathological samples, the coexistence of another scattering species leads to larger uncertainties of R_g. Thus, the difference seen in R_g between different salt concentrations and after PAA complexation cannot be interpreted explicitly. Additionally, a Krakty plot reveals possible tertiary structure changes which would be reflected in the first maximum (see Figure 5.18). However, no significant structural differences can be detected between all studied samples. Only a minor difference is seen between samples with different ionic strength, independent of the complexation state.

Table 5.6: Overview of samples and experimental conditions with corresponding results of radius of gyration R_g obtained from the fits.

Sample	C-A	C-B	P-HSA	P-HSA	P-HSA + PAA
Ionic strength in mM	150 PBS	150 PBS	150 PBS	20 MOPS	20 MOPS
Radius $R_g \pm 1$ in Å	29.4	28.8	27.6	29.7	30.3

C-A and C-B samples corresponds to HSA isolated from two different healthy individuals as control samples. P-HSA samples corresponds to HSA samples that were isolated from one individual of pathological condition (suffering from CKD) in a single experimental procedure.

To conclude this section, it can be stated that the tertiary structure of HSA is preserved for all protein samples analyzed in the present study. A clear difference emerges in the low q-regime of HSA isolated from pathological patients to native HSA that might indicate

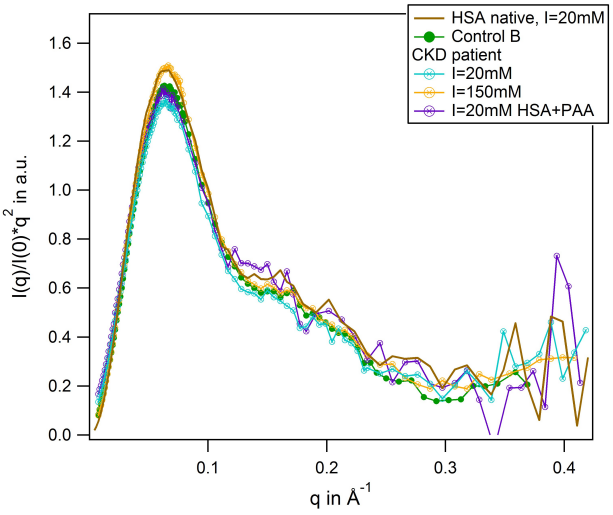

Figure 5.18: Kratky plot of the normalized intensities shown in Figure 5.17. The profile of Control A was left out for better clarity, as no large difference is seen to Control B scattering profile.

the presence of larger agglomerates that is not present in the native HSA solution. Indeed, modifications of HSA have been found in the blood of patients suffering from CKD, but the consequences of these modifications on the interaction of HSA with other proteins or ligands are unclear. [178] It is therefore possible that these modifications might change the protein surface charge distribution and thus leading to aggregation. Unfortunately, the SANS experiments performed give no direct proof of such an effect and more studies are necessary to confirm this assumption.

5.3 Structure of the protein-polyelectrolyte complex

The next step in spatial characterization of the system is to investigate, whether structural changes due to adsorption of PAA is induced to the native HSA structure. PAA concentrations were adjusted relative to the HSA concentration with molar ratios 8:1 and 2:1 of PAA to HSA, respectively. The scattering of higher concentrated, pure PAA solution in 20 mM MOPS buffer was measured as reference. The higher concentration was chosen to achieve acceptable scattering intensities, as PAA is a rather small molecule and scatters only weakly. The total concentrations were 4.7 g/L of HSA for all samples and 1 g/L and 0.25 g/L PAA for the two different molar ratios, respectively. Two ionic strengths 20 mM and 150 mM were adjusted using 10 mM MOPS buffer and additional NaCl. Additionally, the effect of divalent ions, namely $MgCl_2$ and $CaCl_2$, on the complexation of PE-protein was studied at a total ionic strength of 20 mM. [5] All experiments were performed at 37 °C.

Raw scattering data (prior to background correction) of pure HSA solution, pure PAA solution and HSA-PAA complex with molar ratio 1:8 and ionic strength I = 150 mM are shown in Figure 5.19a). A noticeable observation is the forward scattering of free PAA molecules in solution. This is due to the polyelectrolyte effect as observed in literature. [179] In the high q-regime, an almost constant scattering intensity of ≈ 0.058 cm^{-1} is found.

[5] The ionic strength were achieved with 1 mM $MgCl_2$ + 2.5 mM $CaCl_2$ + 10 mM MOPS = 20 mM

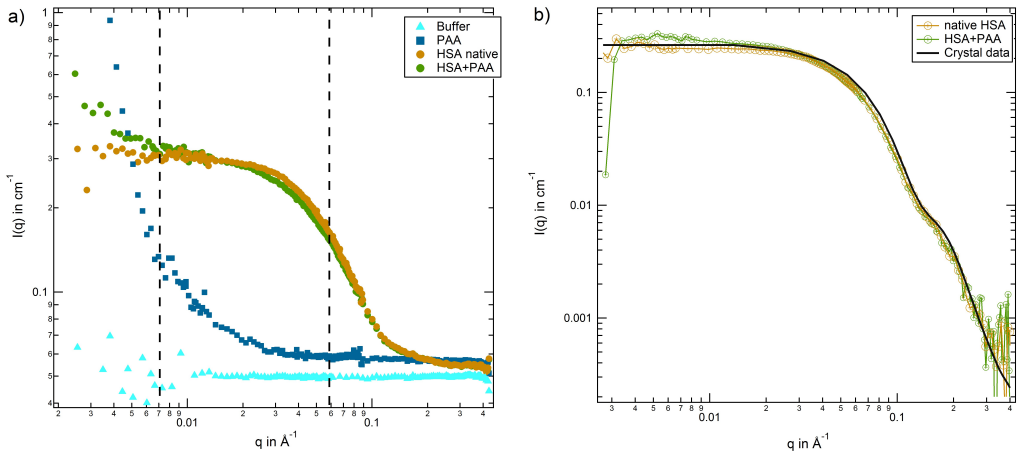

Figure 5.19: Structure of HSA complexed with PAA in comparison with HSA in solution. (a) Raw scattering data without background correction are shown for buffer (blue triangles), PAA scattering in solution (blue rectangles), native HSA (brown circles) and HSA complexed with PAA (green circles). Vertical dashed lines indicated the combination q ranges measured at different detector distances (20 m, 6 m and 1 m). (b) Background corrected scattering profiles from native and complexed HSA are compared to the theoretical crystallographic profile. The intensities of the complex are corrected for scattering of free PAA in the solution.

Subtracting the intensity of buffer scattering (≈ 0.049 cm^{-1}), the resulting intensity corresponds very well with a theoretically approximated forward scattering intensity $I_0 \approx 0.01$ of PAA molecules calculated using Equation (3.52). [6] The scattering contribution of free PAA in the solution is also observed in the raw scattering data of HSA-PAA complex solutions in Figure 5.19a) and needs to be subtracted when analyzing the scattering contribution of the complex. The intensity of that contribution thus calculates to:

$$I_{\text{HSA-PAA}}(q) = \underbrace{[I_{\text{tot}}(q) - (1-\phi_{\text{HSA}})I_{\text{buffer}}(q)]}_{\text{total measured scattering intensity}} - \underbrace{\frac{c_{\text{PAA}}}{c_{\text{ref}}}\,[I_{\text{PAA}} - (1-\phi_{\text{PAA}})I_{\text{buffer}}(q)]}_{\text{scatteing of free PAA in solution}} \quad (5.6)$$

where the first term describes the buffer corrected total scattering intensity and the second term accounts for the buffer corrected scattering of free PAA molecules in solution. The free PAA concentration is calculated based on the previous findings by ITC and computer simulation that binding occurs at a 1:1 ratio. Thus, the scattering of free PAA I_{PAA} is scaled from the reference concentration c_{ref} to the calculated free PAA concentration c_{PAA}. The result is shown in Figure 5.19b) as green data points. After correction, the scattering of the complex hardly differs from the scattering profile of native HSA at I = 20 mM and all curves overlap with theoretically calculated intensities (solid line).

This procedure was applied to each data set. Due to limited experimental time, low q-regime measurements were conducted only for two more samples, namely the native HSA sample

[6] Equation (3.52) is used to calculate the forward scattering $I(0)$ of PAA with $\nu \approx 0.71$, MW = 1800 g/mol, c = 8 g/L and $\Delta\rho \approx 2.93\text{cm}^{-1}$.

and a HSA-PAA complex sample with molar ratio 1:2. An overview of all scattering curves is given in Figure 5.20a). Reliable scattering data can be obtained up to q ≈ 0.4 Å^{-1}. In the intermediate and high q-range, no significant difference to the native HSA data (brown circles) is observed after complexation. For a molar ratio of 1:2 HSA-PAA and I = 150 mM, signatures for aggregation are present, even after the subtraction of free PAA scattering. It is possible that higher salt concentration in the solution leads to an increased screening of the repulsive charges of the complex and thus enables an attractive interaction.

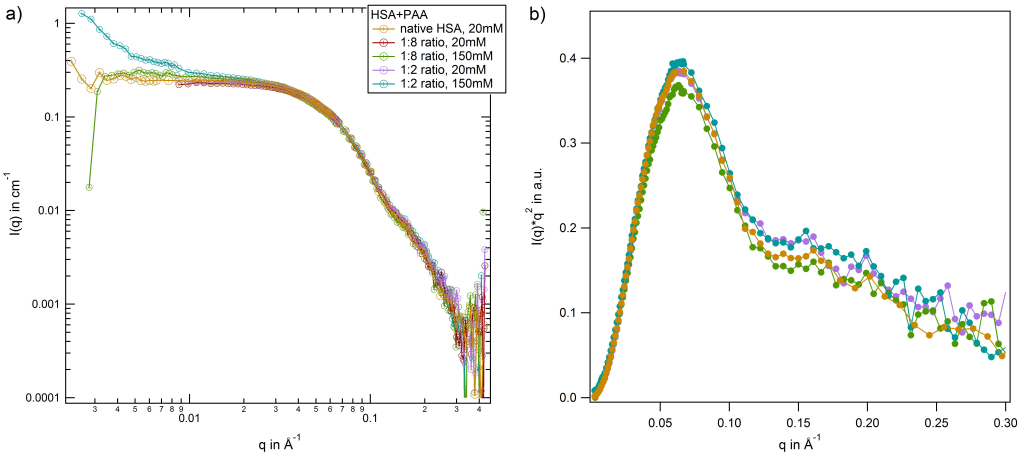

Figure 5.20: Structure of HSA-PAA complex in comparison to HSA in solution. (a) Scattering data taken at 37 °C and I = 20 mM. (b) Kratky plot of the scattering data shown in a).

Table 5.7: Overview of neutron experiment and corresponding fit results for HSA complexation with PAA at two ionic strengths using different salts. All experiments were carried out at 37 °C with 10 mM MOPS as buffer solution.

HSA:PAA ratio	Ionic strength in mM	c(HSA) in g/L	c(PAA) in g/L	$R_g \pm 0.8$ in Å	$I_0 \pm 0.01$ in cm^{-1}
1:0	20	4.7	0	26.7	0.26
1:0	150	4.75	0	27.2	0.26
1:8	20	4.7	1	26.5	0.25
1:8	20†	4.7	1	26.4	0.26
1:8	150	4.7	1	28.4	0.26
1:2	20	4.7	0.25	27.3	0.26
1:2	150	4.7	0.25	28.1	0.28

† This sample contains divalent ions $MgCl_2$ and $CaCl_2$ that was added to the MOPS buffer solution

The tertiary structure of the HSA-PAA complex is investigated in a Kratky plot (see Figure 5.20b). For clarity, only selected profiles are shown.[7] It is quite evident that binding of

[7]The data not shown here are depicted in Figure 8.7 in the Appendix.

PAA to HSA does not effect the protein structure significantly. A minor difference is only seen between different high ionic strength measurement. This finding is reflected in the fitted radius of gyration R_g as well, which are listed in Table 5.7. Here, neither molar ratio nor the valency of the salt seems to have an impact on R_g. A difference of about $1.5-2$ Å^{-1} enlargement of R_g is found for the increase of ionic strength in the solution. However, this difference is at the margin of resolution and interpretation must be conducted with care.

Another fit parameter of interest is the forward scattering intensity I_0, as it gives the molecular weight of the complex according to Equation (3.52). For the scattering of pure HSA in solution, one obtains MW(60 %) = 45 kDa for 60 % of H-D exchange and MW(90 %) = 56 kDa for 90 % exchange respectively. These values are in line with the MW values determined by contrast variation in Section 5.2.2.1 and Table 5.5. Nonetheless, no change in I_0 with adsorption of PAA is found in the present study. This is a reasonable finding, as contribution of free PAA to scattering is only about 0.01 cm^{-1} and thus the adsorbed PAA intensity with much lower concentration can be approximated by ≈ 0.0013 cm^{-1}. This intensity is within the margins of error of $dI_0 = 0.01$ cm^{-1}. As a result, it can be concluded that HSA structure is not altered upon PAA adsorption and the interpretation of ITC data in the previous Sections are valid.

6 Binding of uremic toxins to HSA

The second part of this thesis explores the uptake of two uremic toxins by HSA. These toxins are small, hydrophobic molecules and thus other contributions to interaction can be explored. Beside the verification of the stability of HSA upon adsorption, SANS studies of high concentrated solutions were carried out to investigate the interparticle interaction between proteins loaded with toxins.

6.1 Thermodynamic analysis of binding

Systematic series of ITC experiments were performed with high (I = 150 mM) and low (I = 20 mM) ionic strengths and three different temperatures comprising room temperature 25 °C, a intermediate temperature 30 °C, and the physiological temperature 37 °C. The experiments were performed at pH 7.2 in buffer solution. Finally, the aspect of protein modification on the binding affinity of toxins is evaluated.

6.1.1 Binding of Phenylacetic acid (PhAA) to native HSA

Typical raw data with ITC titration peaks for adsorption (black curves and points) and dilution (blue curves and points) is shown exemplarily for the adsorption of PhAA to native HSA in Figure 6.1a). The integrated isotherms were fitted after subtraction of dilution with either a *Single set of independent sites* (SSIS) model, *Sequential binding sites* (SBS) model or *Two set of independent binding sites* (TSIS) model [1] in Figure 6.1b).

All measured signals were weakly exothermic and exhibit similar monotonic curve progression as shown in Figure 6.1b). This result is typically observed in the adsorption of small hydrophobic molecules to HSA in other studies as well. [31, 87, 180] Because the overall heat is rather small, dilution must be subtracted carefully as an additional heat signal may affect the results of the fits.

6.1.1.1 Evaluation of ITC data

The evaluation of ITC data is demonstrated on the example of PhAA adsorption to native HSA. In Figure 6.1c) a binding isotherm is shown for adsorption at 25°C and 20 mM salt and corresponding fits with the two models described in Section 3.2 to evaluate the quality of the fits. Two fit curves for fixed $N = 1$ and $N = 2$ (dotted and dashed line respectively)

[1] All models were fitted using the implemented ITC Data Analysis software for Origin by MicroCal.

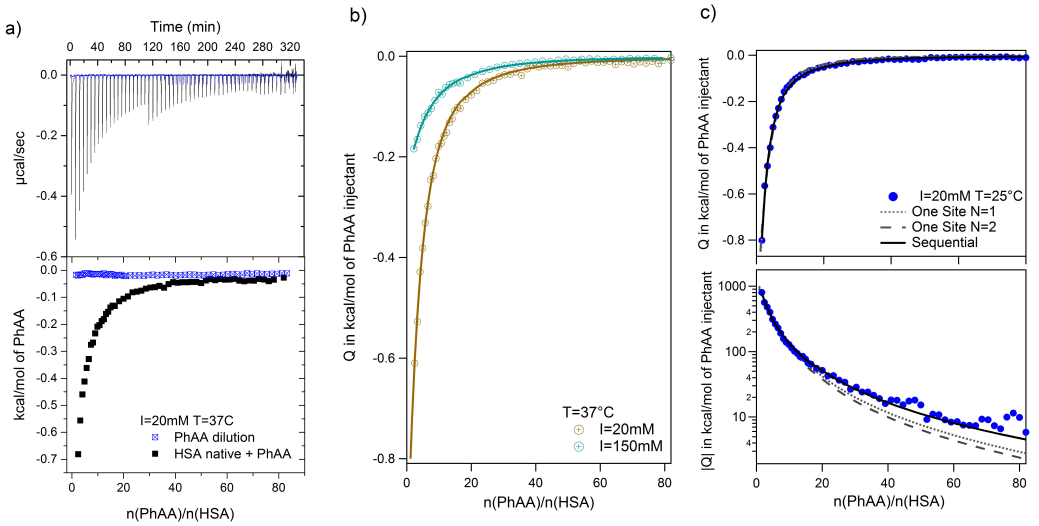

Figure 6.1: PhAA adsorption to native HSA. (a) Calorimetric titration curves are shown for adsorption (black line and symbols) and the corresponding heats of dilution (blue line and symbols) at I = 20 mM and T = 37 °C. (b) Dilution corrected isotherms with corresponding fits are shown and the data for 150 mM is compared to 20 mM at 37 °C. (c) The quality of different fit models are demonstrated on the example of 20 mM and 37 °C data in a typical ITC plot (top) and a semi-logarithmic plot of |Q| (bottom). Reprinted with permission from [181]. Copyright 2017 RSC Advances.

with the SSIS model are compared to the SBS model for two sites. As the curves can hardly be discriminated in the common ITC diagram (as shown in the top of Figure 6.1c), an alternative plot of the absolute value of ITC heats |Q| on a logarithmic axis (bottom figure) is introduced. At low molar ratio, all fitted curves coincide with the data. However, at higher PhAA concentrations, deviations between the different fits become more obvious and the importance of the high molar ratio data is evident. For the given case, data points are clearly best described by the SBS model, pointing towards the existence of two different binding sites of the HSA for PhAA. In the following this semi-logarithmic plot is used to determine the best fit available.

A few more examples are shown in Figure 6.2. Comparing the different binding isotherms and their fitting, it becomes evident that binding behavior is different for different temperatures and ionic strengths. At high temperature, both models converge towards each other (see Figure 6.2b) and c). The affinity K_{b2} to bind a second PhAA molecule to HSA becomes very weak for 20 mM salt and 37°C and vanishes for higher ionic strength at the same temperature (see Figure 6.2c) and Table 6.1 and Table 6.3). In this case, the data can be well described with the SSIS model with $N = 1$. For other cases, where two binding sites are present, the SSIS model permanently underestimates binding affinity and enthalpy and produce a rather large error as seen in χ^2. A comparison of the results of the fits is given in Table 6.1.

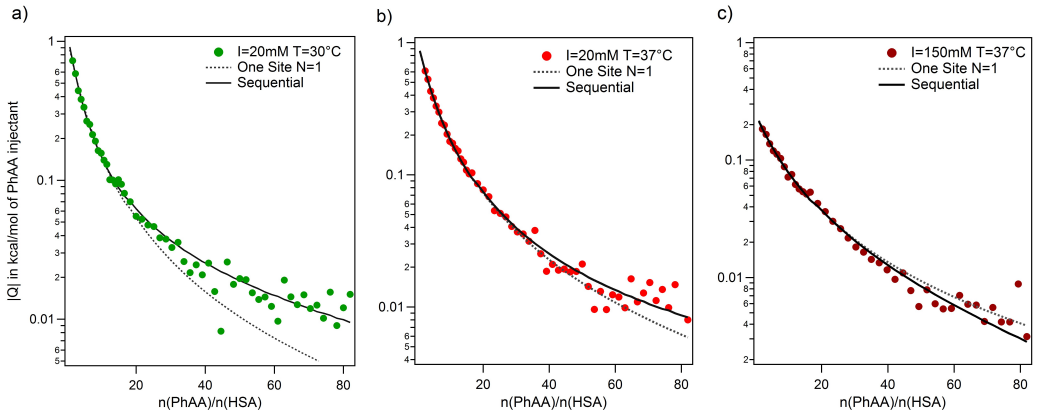

Figure 6.2: Binding model analysis of PhAA adsorption to native HSA. Logarithmic plots as shown before to discriminate the quality of two binding models SSIS (solid line) and SBS (dotted line). Three representative binding cases are shown for I = 20 mM at (a) 30°C and (b) 37°C and for (c) I = 150 mM and 37°C. Reprinted with permission from [181]. Copyright 2017 RSC Advances.

6.1.1.2 Influence of temperature on the strength of binding

The dependence of the adsorption of PhAA onto HSA on ionic strength and temperature were studied to conduct a full thermodynamic analysis. Measurements at different temperatures are depicted exemplarily in Figure 6.3 for I = 20 mM and 150 mM ionic strength. The best fits determined as explained before are depicted as lines. In contrast to the adsorption of polyelectrolytes (PE) to HSA that has been investigated in earlier studies, [149] the present binding curves do not exhibit a strong dependence on temperature for either 20 mM or 150 mM ionic strength. Nevertheless, a consistent change in the curvature of the isotherms is obvious and also reflected in the binding parameters listed in Table 6.2.

In general, the binding affinity decrease with increasing temperature as has been observed in several cases of adsorption of small molecules to HSA. [24, 31, 33, 85] For example, Zaidi et al. have studied interaction between hippuric acid (HA) and HSA and their dependence on temperature using steady state fluorescence quenching measurements and ITC. The ITC data was analyzed using the SBS model likewise and reveal common trends for the dependence of the binding constant on temperature.

In a direct comparison of the literature data with the present results, binding affinity of the first binding site very much coincides in trend and magnitude as shown in Figure 6.4 (brown triangle and spheres). [31] For the second binding site, a minor dependence on temperature was observed in the case of PhAA adsorption to HSA. The dependence on temperature can be analyzed according to van't Hoff's law (see Equation (3.25)).

Van't Hoff plots of the first and second ligand binding process are displayed in Figure 6.4 and the results summarized in Table 6.2. The analysis of the van't Hoff enthalpy done here is

Table 6.1: Thermodynamic parameters obtained with different fit models for the different experimental conditions in Section 3.1.

I (mM)	T ($^\circ C$)	Model	N_{total}	ΔH_1 (kJ/mol)	$K_{b1} \cdot 10^3$ (M^{-1})	ΔH_2 (kJ/mol)	$K_{b2} \cdot 10^3$ (M^{-1})	χ^{2*}
20	25	One Site	1	-23.0±0.2	17.3±0.4	-	-	80
			2	-11.0±0.1	21.1±0.8	-	-	144
		Sequential Binding	2	-20.1±0.6	21.8±1	-8±1	0.95±0.3	50
20	30	One Site	1	-24.9±0.3	12.9±0.4	-	-	109
		Sequential Binding	2	-20.7±0.7	17.4±0.9	-12±1	0.9±0.2	50
20	37	One Site	1	-29.4±0.6	10.3±0.2	-	-	37
		Sequential Binding	2	-26.8±0.6	11.5±0.5	-0.7±0.3	0.84±0.3	27
150	37	One Site	1	-12.6±0.2	5.6±0.1	-	-	8
		Sequential Binding	2	-12.7±0.3	5.5±0.2	5±3	0.14±0.05	8

χ^2 is the error of the fit obtained by the implemented ITC Data analysis software by MicroCal.

only semi-quantitative since a fully quantitative determination would require measurements at far more temperatures than done here. For the toxin IDS, the enthalpy as measured directly by ITC and van't Hoff enthalpy coincide quite well and ΔH_{ITC} is in the present study a good measure for the enthalpy of the binding. In the following, the focus lays on the analysis of the binding free energy ΔG_b calculated using Equation (3.20).

Another interesting feature is observed for I = 150 mM, where a decrease of a second ligand binding with temperature is measured. At high ionic strength and temperature both binding enthalpy and binding constant almost vanishes pointing towards an increased Coulombic screening and thus a weakening of the interaction. This is a plausible explanation for the results obtained recently by Jankowski et al. who measured almost a doubling of released PhAA during hypertonic predilution hemodiafiltration. [30] Furthermore, it was shown in the previous Section 5.1 that ionic strength does contribute significantly towards charge-charge interaction between protein and the polyelectrolyte.

6.1.1.3 Influence of ionic strength on binding

To gain more detailed insight into the effect of ionic strength, three additional measurements were performed at 37°C and I = 50 mM, 70 mM and 100 mM (with ITC parameters listed in Table 1). Exemplary isotherms are presented in Figure 6.5, while in the inset binding constant K_{b1} is plotted against ionic strength. The binding energy ΔG_{b1} is found to be lowered only by 1.5 kJ/mol when adding salt in a wide range from 20 to 150 mM concentration. This small effect due to ionic screening demonstrates that the net electrostatic

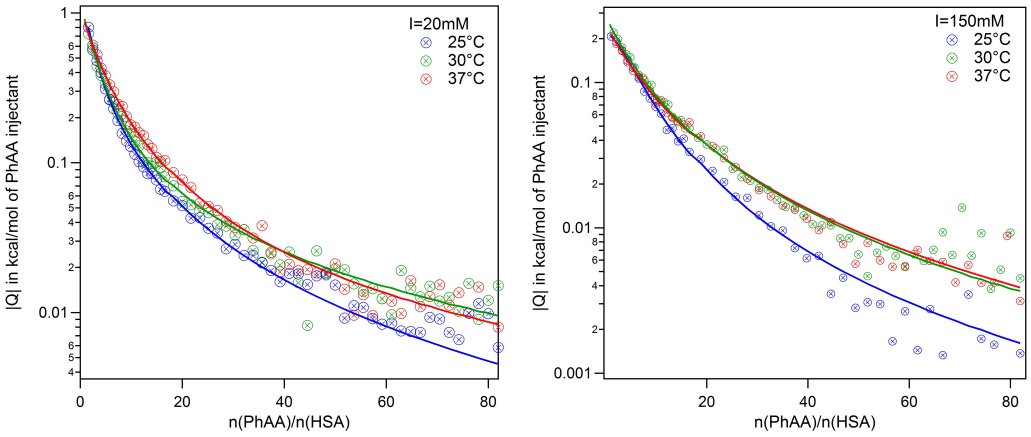

Figure 6.3: PhAA adsorption to native HSA. Absolute heats |Q| are shown for ionic strength I = 20 mM and 150 mM at different temperatures and respective fits are displayed. Reprinted with permission from [181]. Copyright 2017 RSC Advances.

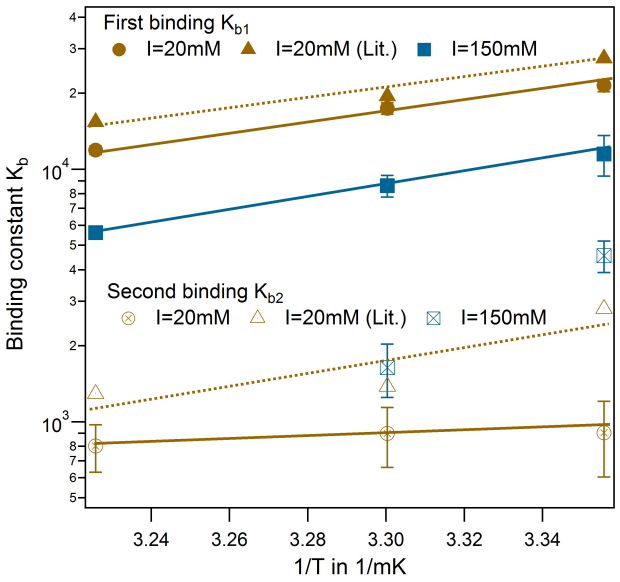

Figure 6.4: Effect of temperature for PhAA binding to native HSA. Binding affinities for first (filled symbols) and second binding process (open symbols) are shown in a van't Hoff plot for I = 20 mM (brown) and I = 150 mM (blue) with corresponding fits according to Equation (3.25). Literature data for HA-HSA binding with 20 mM sodium phosphate buffer (pH 7.4) are included as triangles with dotted lines as guideline for the eye. [31] Reprinted with permission from [181]. Copyright 2017 RSC Advances.

contribution to binding is rather weak when compared, for instance, to the interaction of a PE chain to HSA. [149] Hence, it can be tentatively concluded that hydrophobic binding plays the dominant role.

A simple Debye-Hückel (DH) perspective for screened electrostatic interactions sketched in the following supports this conclusion. For this, consider the DH interaction between two spherical molecules i and j of valence z_i and z_j and radii R_i and R_j, respectively, at a binding distance $r_{\text{bind}} = R_i + R_j$, which reads: [118, 182–184]

$$\Delta G_{DH}^{ij}/k_BT = \frac{z_i z_j \lambda_B}{(R_i + R_j)(1 + \kappa R_i)(1 + \kappa R_j)}. \tag{6.1}$$

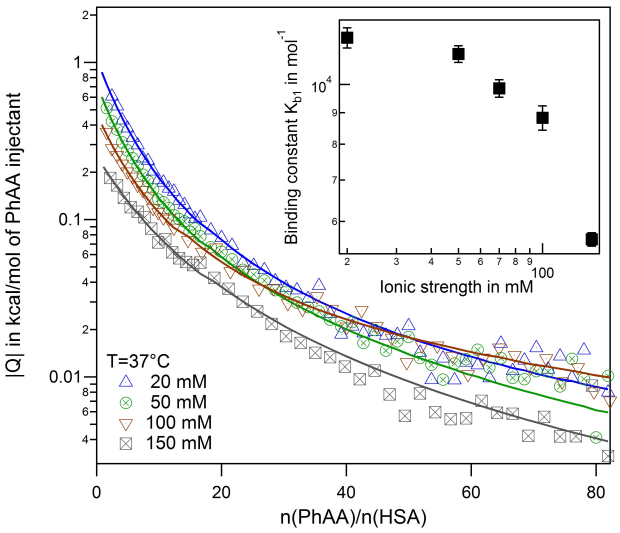

Figure 6.5: Effect of ionic strength at 37°C. Binding isotherms and corresponding fits for a series of ionic strengths from I = 20 mM - 150 mM are shown. The inset displays the binding affinity in dependence of ionic strength. Reprinted with permission from [181]. Copyright 2017 RSC Advances.

Here, $\kappa = \sqrt{8\pi\lambda_B c_{\text{salt}}}$ is the inverse Debye screening length and $\lambda_B \approx 0.7$ nm is the relevant Bjerrum length.

Furthermore, two competing, leading order electrostatic contributions are assumed: first, the local attraction of the negatively charged ligand to the binding site at which a few positively charged amino acids are clustered together. The study on binding between PAA and HSA in the previous Chapter, for instance, suggests about 2-3 positive charges involved in binding near the Sudlow II site. Second, the overall repulsion of the ligand is the sum of all the other negative charges on HSA.

For the attractive term the size of the charged groups at the binding site is assumed to be on atomistic scales and the same as the ligand, i.e., $R_{PhAA} = R_{site} \approx 0.2$ nm, such that the binding distance is $R_{site} + R_{PhAA} \approx 0.4$ nm. The ligand valency is $z_{PhAA} = -1$, and with presumably two positives charges, $z_{site} = +2$. According to Equation (6.1) then the attractive term contributes approximately -7 kJ/mol to the binding energy, decreasing in absolute magnitude with increasing ionic strength to about -5.5 kJ/mol.

For the repulsive contribution, the protein is modeled as a charged sphere of radius $R_{HSA} \approx 3.25$ nm [185, 186] and a net charge of -14 e. [2] Thus, to compensate for the positive site, a remaining net valency of $z_{HSA} = -16$ is obtained which is assumed to be located in the HSA center of the protein for simplicity. An illustration of the model is shown in Figure 6.6.

Due to the relatively large size of HSA, the electrostatic coupling [187] is weak and within the validity of the DH treatment. The distance between the bound ligand and the protein center-of-charge is $R_{HSA} + R_{PhAA} \approx 3.45$ nm. According to Equation (6.1) this leads to a repulsive contribution of $\approx +3$ kJ/mol at the lowest, and decreasing rapidly to only $\approx +1.5$ kJ/mol at the highest salt concentration. Hence, the net electrostatic interaction $\Delta G_{el} = \Delta G_{DH}^{HSA-PhAA} + \Delta G_{DH}^{site-PhAA} \simeq -4 \pm 1$ kJ/mol is attractive and small compared to

[2] The number of charges of the protein can be calculated from the crystal structure.

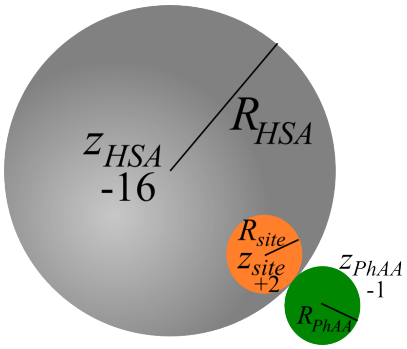

Figure 6.6: Schematic illustration of the model assumed to calculate the Coulombic contribution. The grey sphere represent HSA with −16 charges located at its center, orange sphere marks positive binding site on the protein and the green sphere represents the PhAA toxin bearing two negative charges.

the total experimental binding energies that are in the range between −25 and −23 kJ/mol (see Table 6.2), decreasing with increasing salt concentration.

Clearly, these numbers are highly approximative as, for instance, HSA is non-spherical and detailed charge asymmetry and excluded-volume effects on screening [188] have been neglected. However, the estimates exemplify at least some order of magnitude and trends. The estimated attractive electrostatic contribution (between PhAA-site) to the binding is actually similar to monovalent ion pairing affinities found in explicit-water computer simulations. [189] While the salt concentration dependence should be qualitatively correct, quantitative details are expected to be more complex than in the simple DH perspective due to very local hydration and polarization effects. [189–191]

It can be concluded that the electrostatic interaction is small and thus the major contribution must be of hydrophobic nature, stemming from interactions of the aromatic compound of PhAA with the binding site. The total binding free energy can then be formally expressed as:

$$\Delta G_b = \Delta G_{phob} + \Delta G_{el} \tag{6.2}$$

where ΔG_{phob} is the attractive hydrophobic contribution and ΔG_{el} the net electrostatic interaction. Using the ΔG_{b1} values in Table 6.2 and subtracting the approximated values for ΔG_{el} mentioned above, a hydrophobic contribution of the order of about -19 ± 1 kJ/mol is obtained. The latter has comparable magnitude than the binding free energy calculated in explicit-water computer simulations of hydrophobic pocket-ligand binding at 298 K in pure water and with similar ligand size as in the present study. [192] It is also of comparable magnitude than the transfer free energy of a single benzene molecule from liquid water into its own liquid phase. [193] Interestingly, the enthalpy calculated in the explicit-water simulations [192] is $\Delta H = -29 \pm 17$ kJ/mol and thus has the same sign and order of magnitude than $\Delta H_{\mathrm{ITC}} = -20.3 \pm 0.6$ kJ/mol measured in experiments with 20 mM salt (see Table 6.2). This enthalpic signature is the reason for the inverse temperature dependency of ΔG_b where the effect of hydrophobic attraction weakens with increasing temperature. Note that this is actually in contrast to what is typically known for hydrophobic association of simpler systems, which are entropy-driven [194] and is argued to be due to the concave geometry of typical hydrophobic binding pockets. [192, 195–198]

Table 6.2: Thermodynamic parameters for the binding of PhAA to native and urea modified HSA at temperatures 25°C, 30°C and 37°C and ionic strengths from 20 mM to 150 mM.

Ionic strength (mM)	T (°C)	ΔH_1^{ITC} (kJ/mol)	$K_{b1} \cdot 10^3$ (mol^{-1})	ΔG_{b1} (in k_BT) (kJ/mol)	ΔH_{b1} (kJ/mol)	ΔS_{b1} (J/mol/K)	ΔH_2^{ITC} (kJ/mol)	$K_{b2} \cdot 10^3$ (mol^{-1})	ΔG_{b2} (in k_BT) (kJ/mol)	ΔH_{b1} (kJ/mol)	ΔS_{b2} (J/mol/K)
Native HSA											
	25	−20.3±0.6	22±1	−24.7±0.1			−8±1	0.9±0.3	−16.9±0.8		
20	30	−20.7±0.7	17.4±0.9	−24.6±0.1	−37±4	−46±14	−12±1	0.9±0.2	−17.1±0.7	−9±22	27±78
	37	−26.5±0.6	11.9±0.5	−24.2±0.1			−6±1	0.8±0.2	−17.2±0.4		
50	37	−19.2±0.4	11.2±0.4	−24.0±0.1	-	-	−3±1	0.7±0.1	−17.1±0.4	-	-
70	37	−18.9±0.4	9.9±0.3	−23.7±0.1	-	-	−15±4	0.2±0.7	−14±8	-	-
100	37	−15.5±0.5	8.8±0.4	−23.4±0.1	-	-	−15±4	0.3±0.1	−14.6±0.9	-	-
	25	−6±1	12±1	−23.2±0.5			−3±1	4.6±0.7	−20.9±0.4		
150	30	−9.3±0.8	8.6±0.9	−22.8±0.3	−47±8	−79±27	−3±1	1.6±0.4	−18.7±0.6	-	-
	37*	−11.6±0.2	5.6±0.1	−22.3±0.1			-	-	-		
Urea modified HSA											
	25	−19.2±0.6	22±1	−24.8±0.1			−9.2±0.5	1.9±0.3	−18.8±0.4		
20	30	−24.4±0.5	21.0±0.7	−25.1±0.1	−16±4	29±14	−15.9±0.6	1.1±0.2	−17.5±0.4	−22±16	−14±52
	37	−20±1	17±2	−25.2±0.2			−18±1	1.5±0.3	−18.8±0.5		
	25	−10.6±0.6	9.3±0.7	−22.63±0.02			−11±2	0.5±0.2	−15.4±0.9		
150	30	−11.9±0.4	7.6±0.4	−22.50±0.01	−42±7	−65±24	−9±1	0.6±0.1	−16.0±0.4	−10±15	20±53
	37	−9.3±0.7	4.8±0.4	−21.84±0.02			−4±1	0.4±0.2	−15.6±1.3		

* Data is fitted with SSIS as explained in Section 3.2.1 (see also Table 6.1).

6.1.1.4 Binding of Phenylacetic acid to modified HSA

In the following, the effect of carbamylation of HSA through urea [39] on the binding affinity to PhAA under the same conditions as in the previous section is studied. This *in vitro* modification of HSA is known to be found in patients suffering from chronic renal failure conditions, where the urea plasma concentration is chronically elevated. [39] To study the urea-modification on the binding behavior of PhAA to HSA, experiments are performed again at I = 20 mM and I = 150 mM at the same three temperatures as before. Binding isotherms and corresponding fits are displayed in Figure 6.7. Results from the fits are summarized in Table 6.2.

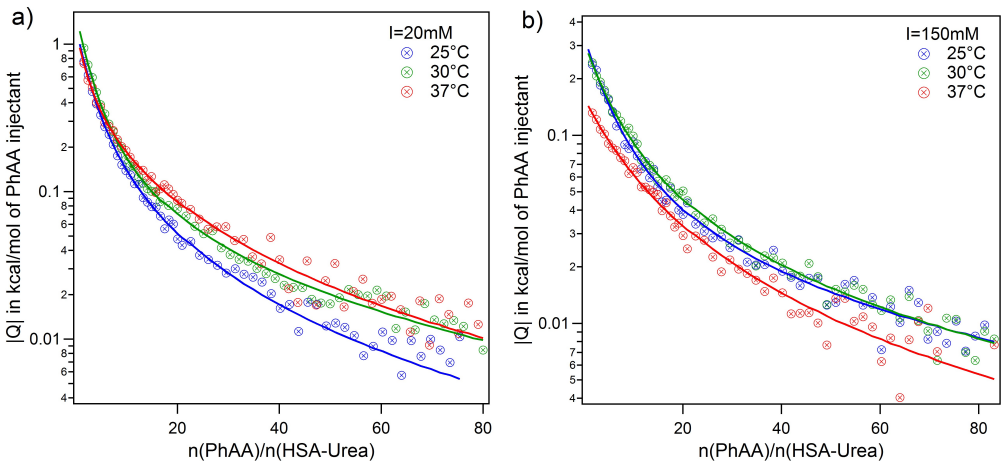

Figure 6.7: Effect of HSA urea modification on PhAA adsorption. Isotherms for adsorption of PhAA upon urea modified HSA for (a) I = 20 mM and (b) I = 150 mM at different temperature is shown. Reprinted with permission from [181]. Copyright 2017 RSC Advances.

For low ionic strength, only weak dependence of binding on temperature is observed for PhAA interaction to urea modified HSA, while the strength of binding is principally unchanged. At high ionic strength and physiological condition, binding is even more weakened compared to I = 20 mM for the modified system. Binding isotherms are equally exothermic and exhibit similar curve shapes as in Figure 6.3. The binding affinity of the urea modified system to the native HSA system is compared for the first binding process and represented in a van't Hoff plot in Figure 6.8.

For the binding of the second ligand at 20 mM salt, no pronounced temperature dependence is observed in both of the systems (see Table 6.2). In both cases, binding of the second ligand is associated with a rather small affinity compared to the error of fitting. As a result, it is difficult to resolve a difference in binding affinities in the modified or native system or a corresponding temperature dependence.

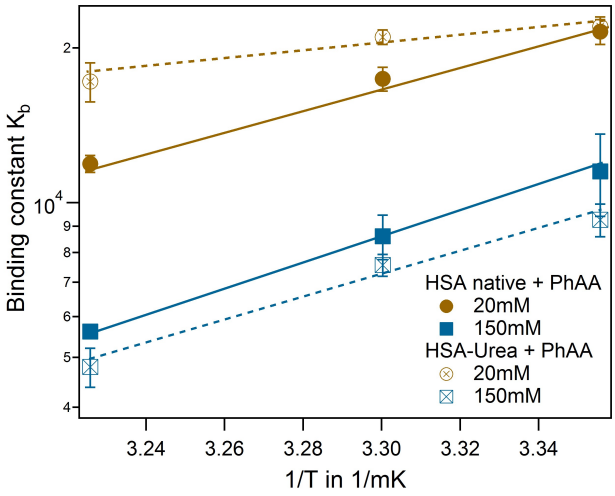

Figure 6.8: Effect of HSA urea modification on PhAA adsorption. Van't Hoff plot of the first binding process for native (filled symbols) and urea modified HSA (open symbols) with according fits. Reprinted with permission from [181]. Copyright 2017 RSC Advances.

6.1.2 Binding of Indoxyl sulfate (IDS) to native and modified HSA.

The adsorption of IDS to native and modified HSA was systematically studied at two ionic strengths I = 20 mM and 150 mM and at three temperatures using ITC. Raw titration peaks and integrated heats for the adsorption of IDS to native HSA are depicted in Figure 6.9.

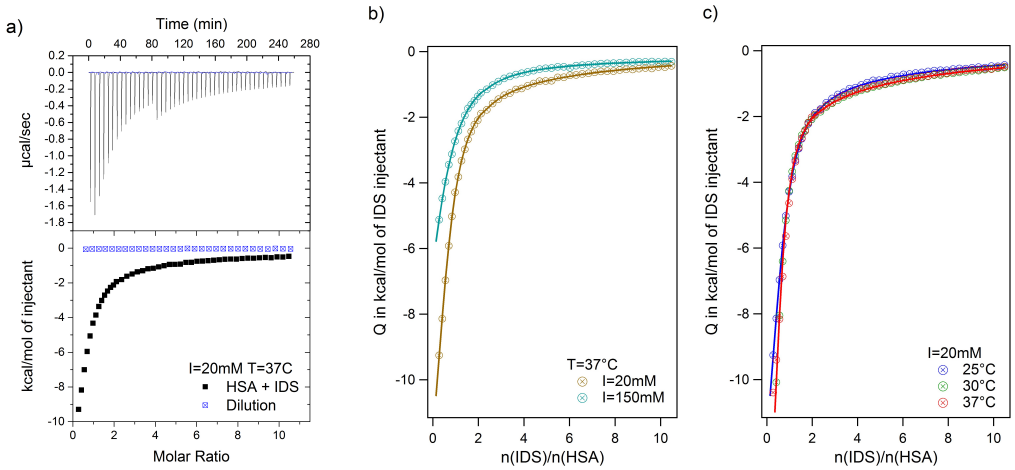

Figure 6.9: Interaction of IDS with native HSA. (a) Titration peaks and integrated heats for I = 20 mM at 37°C. (b) Dilution corrected isotherms with corresponding fits at 37°C and 20 mM and 150 mM. (c) Temperature series of adsorption for I = 20 mM. Reprinted with permission from [181]. Copyright 2017 RSC Advances.

Using the logarithmic representation, exemplary adsorption isotherms and according best fits for adsorption to native and modified HSA are depicted in Figure 6.10. Again all adsorption processes show similar exothermic isotherms as observed for PhAA adsorption in the section above. An increase in ionic strength from 20 mM to 150 mM show the same effect but overall weaker as observed before as shown in Figure 6.9b). However, in the

standard ITC plot in Figure 6.9c), temperature differences between different isotherms are not clearly visible. Therefore logarithmic plots of isotherms and corresponding fits are shown exemplarily for I = 150 mM and the two HSA types in Figure 6.10. Further isotherms of adsorption at 20 mM salt are very similar and can be found in Figure 8.11 of the Appendix.

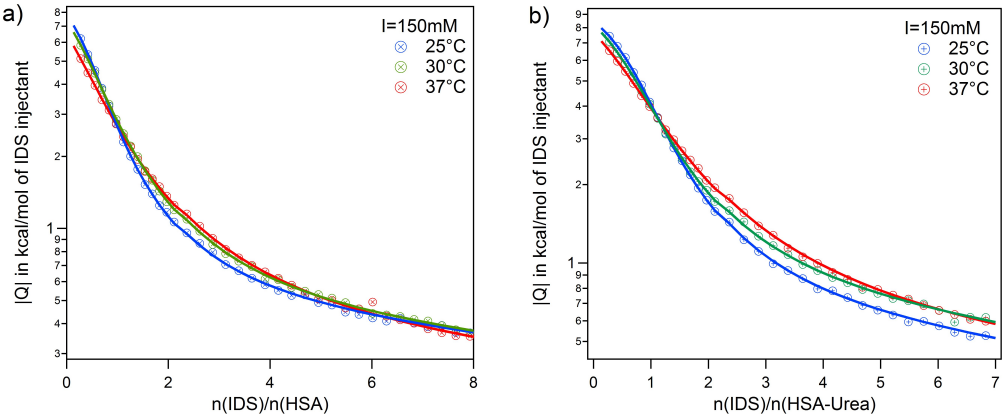

Figure 6.10: Adsorption of IDS to HSA at I = 150 mM. Temperature series and corresponding fits using the TSIS model are shown exemplarily in the logarithmic plot binding to (a) native and (b) modified HSA. Reprinted with permission from [181]. Copyright 2017 RSC Advances.

Here the necessity to use a two site adsorption model is clear. As demonstrated in the case of IDS adsorption to native and modified HSA at 37°C and I = 150 mM in Figure 6.11, the data can neither be described by the SSIS (dotted line) nor the SBS (dashed line) model. There are clearly two binding sites present for IDS with different binding stoichiometry. Using the *Two set of independent sites* TSIS model (solid line), ITC isotherms can be very well described at all measuring conditions. However, the number of IDS molecules adsorbed at the second site N_2 cannot be well determined by a fit of the ITC data. Residual errors for fits with different fixed parameter N_2 (ranging from one to three) show no significant change. It is however not surprising that fitting a monotonic curve with six parameters implies the risk of fitting too many free parameters.

Several studies on the adsorption of IDS to HSA confirm the existence of two binding sites with different binding affinity. [24, 85] Crystallographic analysis of IDS complexed with HSA suggests that one IDS molecule binds to subdomain III-A while two molecules bind to subdomain II-A of HSA. [84] Sakai et al. measured IDS adsorption on HSA at 25°C and 67 mM phosphate buffer at pH 7.4 using equilibrium dialysis. They found two binding sites with $N_1 = 1$ and $N_2 = 3$ for high and low affinity binding site, respectively. [24] A more recent study from Watanabe et al. using ultrafiltration found at same pH and temperature but different buffer, a slightly lower $N_2 = 1.6$. [85] Based on these findings, it appears reasonable to fix N_2 between one and three and average the results. As the residuals between each fits are small (see Figure 6.11b), the standard deviation was used as error for each averaged parameter. Thus, even with an uncertainty of $N_2 = 2 \pm 1$, the

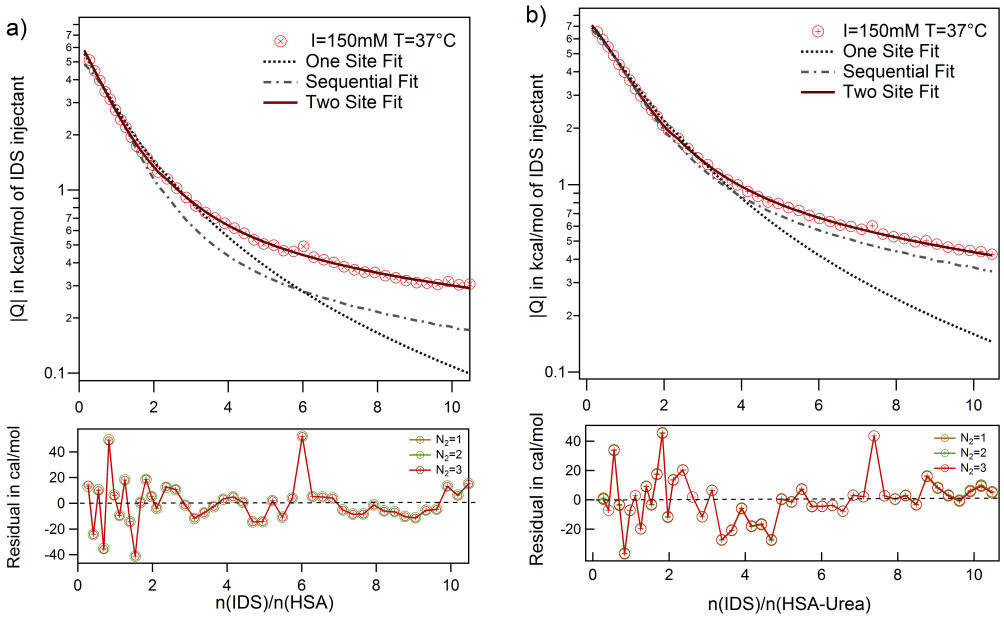

Figure 6.11: Best fit evaluation to analyze IDS binding to HSA. Quality of different fit models and parameters are demonstrated by comparing three models SSIS (dotted line), SBS (dashed line) and TSIS (solid line) for I = 150 mM and 37°C. Beneath the graph is depicted the residual errors for TSIS fits with different fixed N_2 values. Reprinted with permission from [181]. Copyright 2017 RSC Advances.

binding constants k_{b2} obtained are robust and reliable. However, the binding enthalpy ΔH_2 is strongly correlated with the fit parameter N_2 and errors for ΔH_2^{ITC} and consequently ΔS_2 are accordingly large. All results obtained from the fits are summarized in Table 6.3.

Binding of IDS to HSA is generally an order of magnitude stronger than PhAA to HSA in all measured cases. However, caution is required when comparing a macroscopic binding constant K_b to a microscopic binding constant k_b. The microscopic constant k_1 for example describes explicitly the binding process of N_1 ligands to Site 1 while the macroscopic constant K_{b1} assumes binding of either one of the two potential ligands to any of the two sites.

The effect of urea modification is rather small. The van't Hoff analysis comparing native to urea modified HSA reveal temperature dependence of binding for both binding sites, while the dependency is more pronounced for the high affinity site rather than the low affinity site (Figure 6.12). The binding enthalpies for the high affinity site ΔH_1^{ITC} measured directly by ITC agree well with the binding enthalpies derived from the van't Hoff plot (see Table 6.3).

A plot of all results comparing the effect of urea modification on the adsorption of PhAA and IDS is shown in Figure 6.13. Additionally, the present results are put into context to earlier investigations on the interaction between a multiply charged "middle molecule", namely a polyvalent polyacrylic acid (PAA) chain with HSA, to gain a deeper insight into

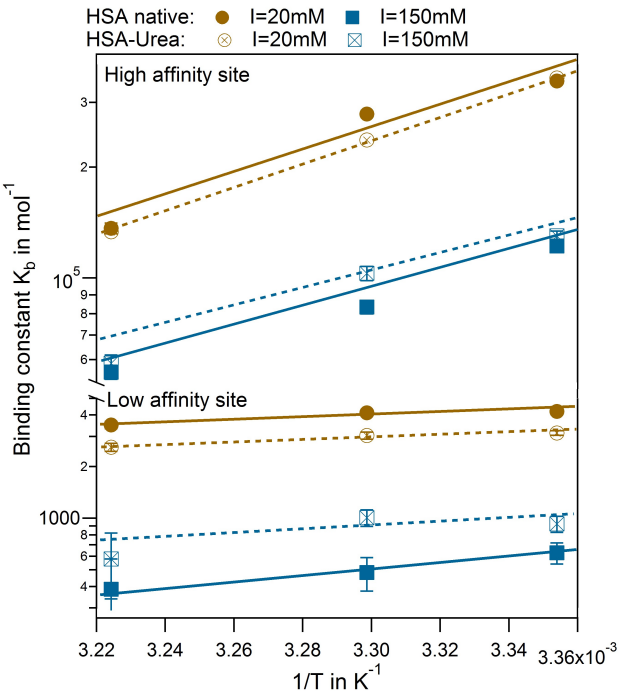

Figure 6.12: Van't Hoff plots for IDS interaction to HSA. High and low affinity binding sites comparing native (filled symbols) and modified (open symbols) HSA are shown for I = 20 mM (brown) and 150 mM (blue) with corresponding fits. Reprinted with permission from [181]. Copyright 2017 RSC Advances.

different contributions to binding. [149] In Figure 6.13 the binding affinity of the small toxins IDS and PhAA to HSA exhibit in all cases moderate decreasing binding affinities to both native and modified HSA while binding of PAA is strongly weakened due to a decreasing counterion-release entropy with rising salt concentration (see Section 5.1). [149] For the present ligands, the hydrophobic interaction plays a dominant role in the binding process as expected.

A characteristic effect for the adsorption of monovalent ligands to proteins is the so called enthalpy-entropy compensation (EEC), which is revealed when measuring temperature dependence of the interaction (see Figure 6.13 b). Here the slope of the entropy contribution $T\Delta S_b$ plotted *versus* the enthalpy ΔH_{ITC} for the first binding process is near unity as indicated by the broken line, which is often interpreted as complete EEC compensation. This effect is commonly involved in interactions between small ligands and proteins and has thus gained more attention recently by several authors. [33, 180, 199, 200] Even though controversies exist for the specific contributions to the EEC effect, it is generally recognized that strong but noncovalent ligand binding to a protein gives rise to a higher enthalpic contribution and is at the same time associated with less flexibility and therefore lowers entropy. In particular, the dissociation of water molecules from the ligand into bulk upon binding of the ligand in a hydrophobic cavity leads to favorable enthalpy contributions with an opposing entropic contibution. It is remarkable that this effect is well observed in the simulations of a ligand-cavity model system by Setny et al. [192] For the present ligands, it is not surprising that hydrophobic interaction plays an eminent role in the binding interactions. Furthermore, EEC is clearly reflected in the free energy of binding ΔG_b which

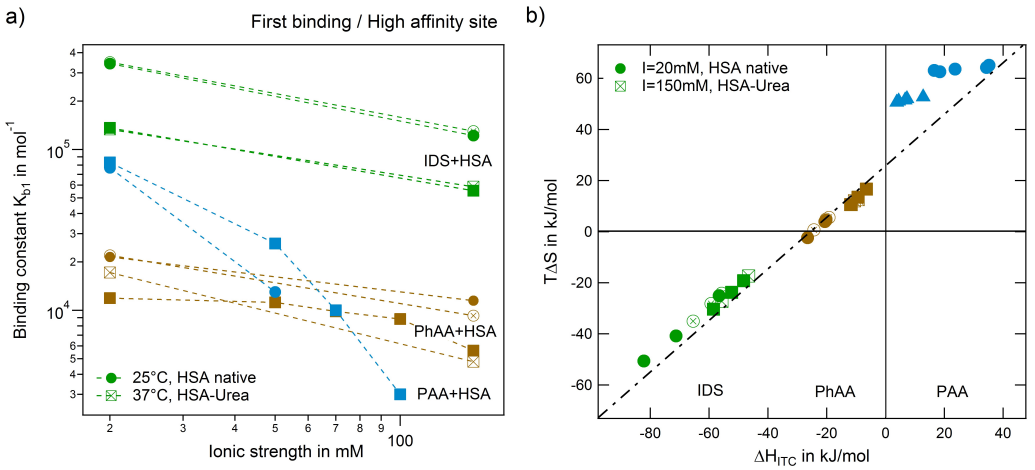

Figure 6.13: Binding parameter overview for the first binding process and high affinity site. (a) Ionic strength dependence and (b) enthalpy-entropy compensation for adsorption of PhAA (brown), IDS (green) and PE (blue) to HSA. Full and empty symbols are native and modified HSA. Spheres and rectangles represent in (a) 25°C and 37°C and in (b) I = 20 mM and I = 150 mM respectively. The dotted lines are guidelines for the eye and have a slope of unity in (b). Reprinted with permission from [181]. Copyright 2017 RSC Advances.

is almost invariant with temperature in all measured cases (see Table 6.2 and Table 6.3). For the polyelectrolyte however (blue symbols in Figure 6.13b)), the EEC effect cannot be observed. Here charge-charge interaction and the resulting release of counterions are the leading terms rather than hydrophobic interaction.

Table 6.3: Thermodynamic parameters for the binding of IDS to native and urea modified HSA at 25°C, 30°C and 37°C and ionic strengths 20 mM and 150 mM. An average N_2 of 2 is assumed for all binding processes.

I (mM)	T (°C)	N_1	ΔH_1^{ITC} (kJ/mol)	$k_{b1} \cdot 10^3$ (mol^{-1})	ΔG_{b1} (kJ/mol)	ΔH_{b1} (kJ/mol)	ΔS_{b1} (J/mol/K)
First binding site							
Native HSA							
	25	0.68±0.01	−56.6±0.5	343±6	−31.59±0.06		
20	30	0.48±0.01	−82.2±0.5	279±3	−31.60±0.05	−50±2	−61±7
	37	0.57±0.01	−71±1	136±5	−30.49±0.09		
	25	0.59±0.01	−48±1	122±2	−29.04±0.05		
150	30	0.60±0.01	−52±2	83±4	−28.6±0.1	−51±3	−75±10
	37	0.55±0.02	−59±2	55±2	−28.1±0.1		
Urea modified HSA							
	25	0.91±0.01	-55.7±0.3	349±8	-31.64±0.06		
20	30	0.89±0.01	−59.3±0.5	237±8	−31.20±0.08	−62±2	−100±8
	37	0.89±0.01	−65.4±0.6	134±4	−30.44±0.07		
	25	0.87±0.01	−46.5±0.5	130±4	−29.19±0.08		
150	30	0.84±0.01	−48.3±0.8	103±5	−29.1±0.1	−49±4	−68±13
	37	0.83±0.01	−55.6±2	59±3	−28.3±0.1		

I (mM)	T (°C)	ΔH_2^{ITC} (kJ/mol)	$k_{b2} \cdot 10^3$ (mol^{-1})	ΔG_{b2} (kJ/mol)	ΔH_{b2} (kJ/mol)	ΔS_{b2} (J/mol/K)
Second binding site						
Native HSA						
	25	−82.3±0.8	4.2±0.08	−20.68±0.05		
20	30	−42.0±0.6	4.1±0.2	−20.98±0.09	−10±3	35±10
	37	−34.2±0.8	3.5±0.2	−21.0±0.1		
	25	−68±54	0.63±0.09	−16.0±0.3		
150	30	−78±16	0.5±0.1	−15.6±0.6	−35±27	−63±90
	37	−82±39	0.4±0.2	−15.4±1		
Urea modified HSA						
	25	−60±1	3.1±0.1	−19.96±0.08		
20	30	−56±2	3.0±0.1	−20.2±0.1	−12±4	28±13
	37	−56±2	2.6±0.1	−20.3±0.1		
	25	−60±9	0.9±0.1	−16.9±0.3		
150	30	−61±10	1.0±0.1	−17.4±0.3	−4±19	42±63
	37	−81±18	0.6±0.2	−16±1		

6.2 Characterization of protein-toxin complexes in solution

The question addressed in the following Section is whether uptake of drugs influences the structure of the protein or the protein-protein interaction. The interparticle interaction is extracted by measuring the structure factor of high concentrated HSA-toxin solutions. Crystallographic studies of HSA-IDS complexes revealed no significant conformational changes associated with the binding. [84] However, these studies cannot be performed in solution and consequently not under physiological conditions.

All neutron scattering experiments were performed at 37 °C and at pH 7.2. Two ionic strengths, 10 mM and 150 mM, were adjusted using 10 mM MOPS as buffer solution and NaCl as salt. A stock solution of 40 g/L HSA in 10 mM buffer was prepared and the toxin concentrations were chosen to achieve full saturation of binding as determined by ITC. For urea modified HSA solutions, samples were dialyzed after 18 h incubation and the concentration was determined afterwards to be approximately 25 g/L. [3] These HSA-toxin samples were subsequently diluted by buffer solution to 22 g/L and 19 g/L. An overview of the experiments is given in Table 6.4.

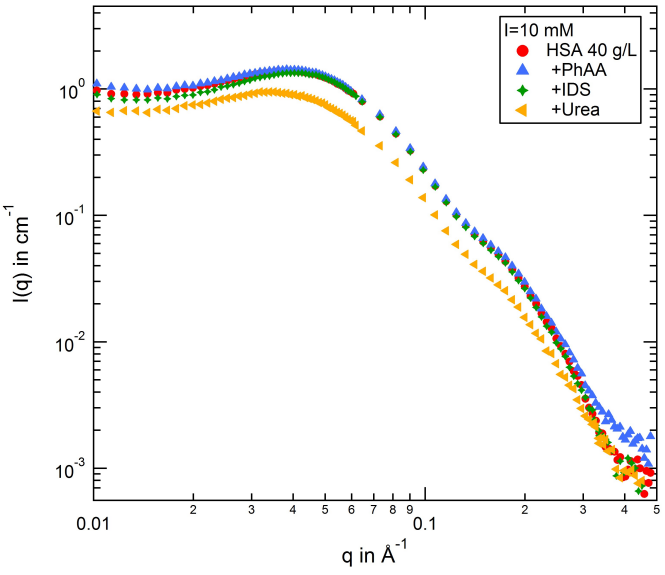

Figure 6.14: Structure of native HSA, HSA complexed with uremic toxins and urea modified HSA at low salt concentration. The concentration of HSA is 40 g/L in all samples except in the urea modified sample, the concentration is approximately 25 g/L. Scattering data are taken at 37 °C and I = 10 mM.

Representative scattering intensities of samples with a HSA concentration of 40 g/L and 10 mM ionic strength are shown in Figure 6.14. The scattering intensities are similar at first sight and small differences are only seen in the low q range, where the effect of structure factor is observed as a decrease of intensity.

The fitting procedure of the data is explained on a representative example and demonstrated in a plot in Figure 6.15. The analysis was carried out in three steps:

[3] Details of sample preparation are given in Section 8.1 of the Appendix.

Table 6.4: Overview of neutron experiments of HSA complexation with three additives: PhAA, IDS and urea at two ionic strengths 10 mM and 150 mM. All experiments were carried out at 37 °C with 10 mM MOPS as buffer solution.

Sample name	c(HSA)±0.1 in g/L	Additive	c(add.)±0.1 in g/L	Molar ratio HSA:add.	Ionic strength in mM
H30	30	-	-		
H35	35	-	-	none	10
H40	40	-	-		
HP30	30		0.26		
HP35	35		0.33	1:5	10
HP40	40		0.35		
HPI40†	12	PhAA	1	1:41	
HPI200†	12		5	1:203	150
HPI400†	12		10	1:406	
HS30	30		0.7	1:6	
HS35	35	IDS	0.7	1:5	10
HS40	40		0.8	1:5	
HU19	18.9		1.8		
HU22	22.2	Urea	1.6	1:50	10
HU25	25.2		1.4		
HI	40	none	-	-	
HPI	40	PhAA	0.35	1:5	150
HSI	40	IDS	0.7	1:5	
HUI	25.2	Urea	1.8	1:50	

† Experiments were performed at the TOF instrument V16.
All other experiments were performed at the monochromatic instrument V4.

1. To obtain the particle scattering $P(q)$ without the influence of the structure factor in low q range, only the high q-range of the scattering curve was used, with $q > 0.05$ (as indicated by the arrow in the top panel of Figure 6.15). The software Gnom was used to fit the data and a curve is obtained which very well describes the intermediate and high q-range of the scattering data (dashed black line). This fit performed by Gnom includes a scaling factor, which accounts for the concentration and the contrast of the scattering particles. The thus obtained and scaled $P(q)$ is then extrapolated to the lowest measured q values. I_0 and R_g are the two parameters derived from the Gnom fit.

2. The total scattering intensity $I(q)$ is proportional to the product of $P(q)$ and the structure factor $S(q)$ [4] (see Equation (3.39)), [127] therefore $S(q)$ is calculated by dividing $I(q)$ by $P(q)$ (blue circles in the bottom panel of Figure 6.15). $S(q)$ is most prominent in the low q region and was fitted using the range as indicated in the plot ($0.015 < q < 0.13$). A model describing the interaction of charged particles screened by salt ions in solution, is the Hayter-Penfold Mean-Sphere approximation (HPMSA) (see Section 3.3.2). [130] Here, the volume fraction ϕ, the temperature (T = 37 °C), the ionic strength in the solution (I = 10 & 150 mM) and the dielectric constant $\epsilon_{H_2O} = 81$ are known parameters and fixed in the fitting procedure. This leaves only two free fit parameters: the effective charge valency $|Z|$ and the diameter of the particles d. These two parameters are not correlated, as demonstrated in Section 3.3.2.1 (see Figure 3.8), and can thus be fitted simultaneously.

3. Finally, the total fit (blue line) is obtained by simply multiplying $S(q)$ and $P(q)$. No additional fitting is performed in this step. However, the experimental data is well described by the resulting fit as seen in Figure 6.15.

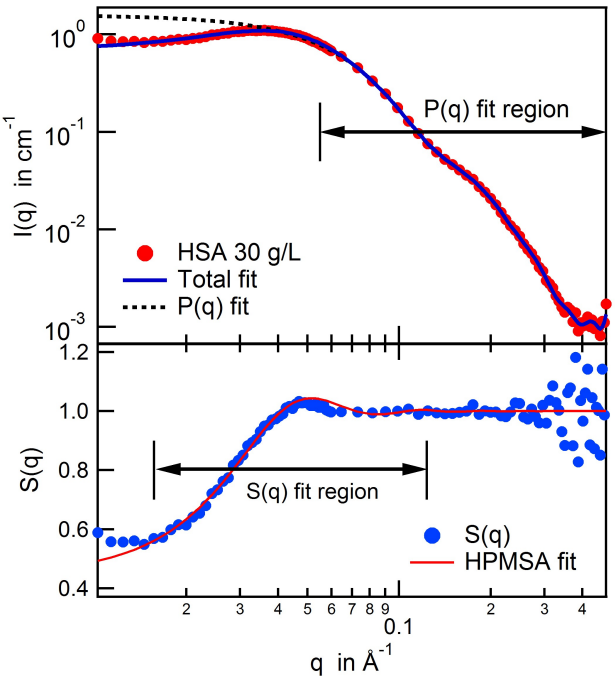

Figure 6.15: Demonstration of the details of the fitting procedures on the example of 30 g/L pure HSA in solution (H30). Top panel: different parts of the scattering profile (red circles) is used to fit the particle scattering ($P(q)$) and the structure factor ($S(q)$), respectively, as indicated by the arrows in the plot. $P(q)$ is obtained using Gnom [171] (dashed black line). The total fit (blue line) is obtained by multiplication of the two single fits. Bottom panel: experimental structure factor $S(q)$ (blue circles) are fitted using the Hayter-Penfold Mean-Sphere approximation (HPMSA).

[4] Additional parameters contributing to scattering as given in Equation (3.39) are included in the fit of P(q).

For each type of system, three different concentrations were measured (see Table 6.4) and fitted according to the procedure explained above. Representative series of measurements for solutions of native HSA and HSA complexed with PhAA are shown in Figure 6.16a) and b), respectively. While the top panel depicts $P(q)$ (black line) and resulting total fit (green line) to the scattering data (red circles), the bottom panel shows the structure factor contribution towards scattering (blue circles) and corresponding fits (red lines). As demonstrated in the case of HSA, the interaction between proteins in the solution are well described by the HPMSA structure factor for charged macromolecules screened by salt ions in the solution (see Section 3.3.2 for details). The effect of structure factor decreases with decreasing concentration in the solution as expected. An overview of results obtained is given in Table 6.5.

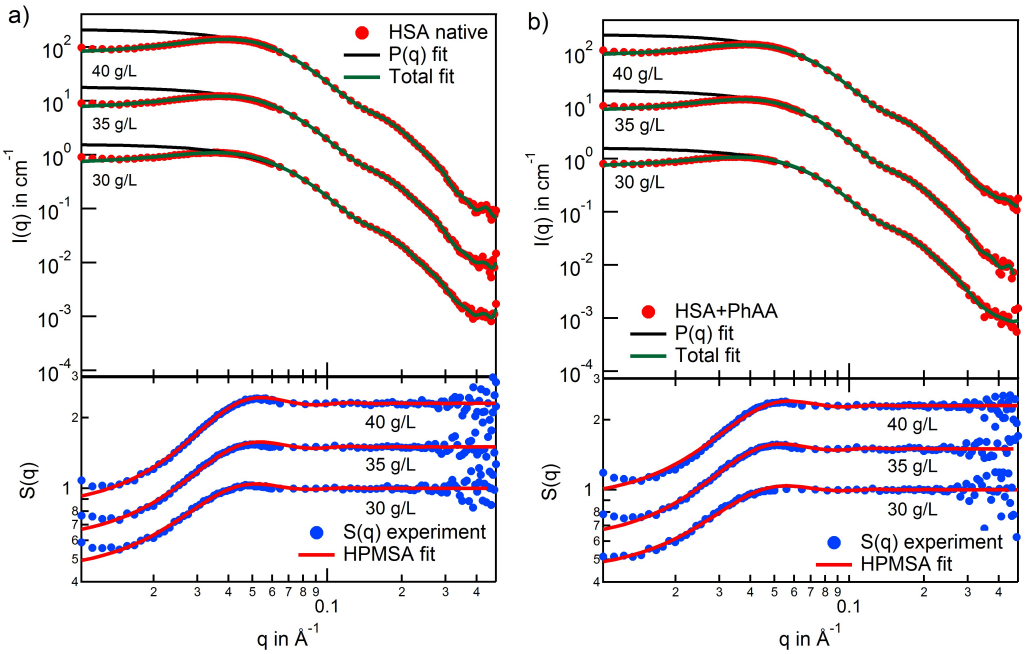

Figure 6.16: Series of dilution of (a) pure HSA solution and (b) HSA+PhAA complex and corresponding fits. Top panels depict the fit for $P(q)$ (black line) and the total fit (green line). Bottom panels show experimental (blue circles) and fitted structure factor (red line) after dividing the scattering profiles by $P(q)$. For clarity, the two scattering intensities in the top panels are shifted by a factor of 10 and 100, respectively, with respect to the scattering intensity of 30 g/L. $S(q)$ of the 40 g/L and 35 g/L in the bottom panels are shifted by a factor of 1.5 and 2.5, respectively.

A series of concentrations for native and pure HSA solution with corresponding fits and the experimental structure factor is shown in Figure 6.16a). The results summarized in Table 6.5 reveal that an effective charge valency $|Z|$ of approximately 13 ± 1 was found for all concentrations, which is very close to the net charge of HSA of 14 at pH 7.2. [149] The radius of gyration was determined by Gnom and yields (26.4 ± 0.5) Å, which is the same value found within the limits of error in the diluted condition of approximately (27 ± 0.5) Å as

demonstrated in Section 5.2.2. The diameters obtained for the protein from the structure factor fits are in average $d \approx 72 \pm 2$ Å and are comparable to crystallographic dimensions of 89 Å x 77 Å x 15 Å [5]. In general, these results validate the fitting procedure described above.

The scattering results obtained for HSA-PhAA complex in Figure 6.16b) are in fact very similar to measurements of pure HSA solutions. The charge valency $|Z|$ is approximately 13 ± 1 and no significant difference to the charge of pure HSA is observed within the range of error. With only two PhAA molecules adsorbed onto HSA as seen by ITC, their influence on the interaction between the proteins is apparently not observable by SANS. The diameters found for the HSA-PhAA complex are in average $d = 69 \pm 2$ Å which is almost equal to the values for pure HSA solutions of $d \approx 72$ Å. For HSA-IDS complexes, a small increase in charge is found compared to pure HSA, with $|Z| = 15 \pm 1$ ($|Z|$(pure HSA) $= 14 \pm 1$). A possible explanation is that three IDS molecules adsorb to HSA as revealed by ITC in the previous Section. [84] Furthermore, a similar value for the diameter d as for pure HSA samples is found with an average of $d \approx 68 \pm 2$ Å (see Table 6.5). Experimental data and corresponding fits of HSA-IDS complex are given in Figure 8.13 of the Appendix.

In general, no prominent effect of toxin adsorption on the size or effective charge of HSA is observed by SANS. This is validated by comparing different structure factors of the HSA-toxin complexes (40 g/L HSA) in Figure 8.14 of the Appendix. The typical structure factor peak at $q \sim 0.04$ Å^{-1} remains invariant with HSA-toxin complexation compared to pure HSA data and thus the deduced value for the diameter d is constant in all samples. Furthermore, the results of the $S(q)$ fits for various concentrations give reliable values for both the diameter and charge of the systems which are constant over concentration as clarified in Figure 6.17. A small difference is observed for the urea modified HSA measurement, where a shift of the maximum of the structure factor to lower q values is observed. Here, concentrations are lower and a more detailed analysis is performed in the following.

Scattering data of a series of urea modified HSA solutions are depicted in Figure 6.18. The concentrations measured here are lower and thus the fitting of the structure factor at lowest concentrations is associated with higher uncertainties. For the lower HSA concentrations of 22.2 g/L and 18.9 g/L, very weak interparticle scattering is observed in the scattering data and the fit for $P(q)$ (black line) and the total fit (green line) almost overlap. Thus results of the fitting of $S(q)$ obtained for these measurements are associated with high uncertainties and will not be considered in the interpretation. The HPMSA fit results indicate that in contrast to the native HSA series, a significantly increased charge is found for the highest concentration, where the best fit result is achieved. An effective charge of approximately 19 ± 1 is obtained here. The diameter $d = 73 \pm 1$ Å is comparable to the results obtained for native HSA.

[5] The crystal data with PDB-ID: 1AO6 was analyzed in terms of size and structure using the software VMD.

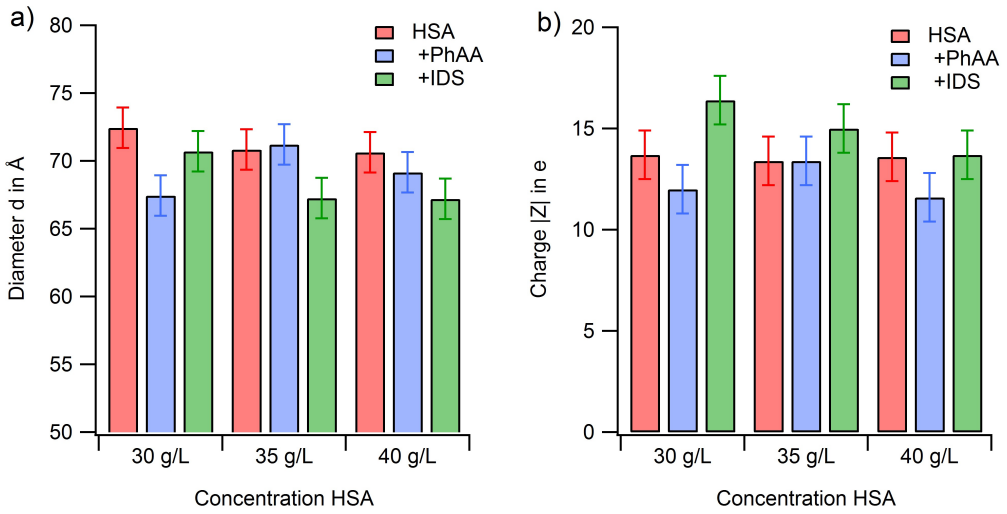

Figure 6.17: Overview of fit results for pure HSA and HSA-toxin solutions. The two parameters derived from the $S(q)$ fits (a) diameter d and (b) charge valency |Z| are constant over the concentration range measured.

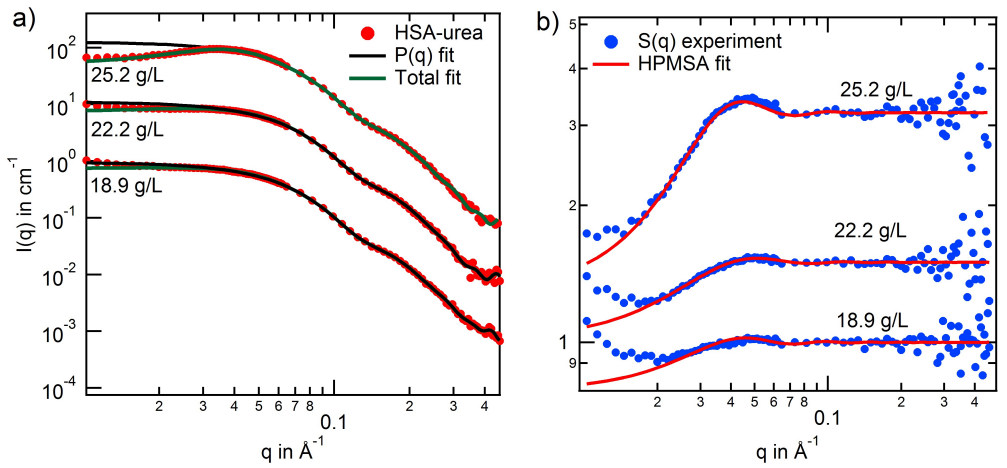

Figure 6.18: Series of dilution of HSA-Urea complex and corresponding fits. (a) Particle scattering fit $P(q)$ (black line) and the total fit (green line) are drawn on top of experimental data (red circles). (b) Experimental (blue circles) and fitted structure factor (red line) after dividing the scattering profiles by $P(q)$. Scattering profiles are scaled with the same factors as in Figure 6.16.

The effect of ionic strength (I = 150 mM) on the interaction between HSA-toxin complexes was investigated. Experiments were performed with a HSA concentration of 40 g/L for pure HSA and HSA-toxin complexes. The concentration for the urea modified HSA sample was 25.2 g/L as in Figure 6.18. The impact of salt in solution is evident in Figure 6.19 when comparing to Figure 6.14, as interactions between proteins are almost completely screened with $S(q) \approx 1$. In general, scattering intensities of all measured samples are very similar. The results of the form factor fit are listed in Table 6.5, where a smaller R_g is observed in

Table 6.5: Summery of results obtained by the combined $P(q)$ and $S(q)$ fit. While I_0 and R_g values are obtained by Gnom, the diameter d and charge valency $|Z|$ are results of the HPMSA fit.

Sample name	c(HSA) in g/L	$I_0 \pm 0.01$ in cm^{-1}	MW ± 5 in kDa	$R_g \pm 0.5$ in Å	$d \pm 2$ in Å	$\|Z\| \pm 1$
I = 10 mM						
	40	2.13	50	26.5	71	14
pure HSA	35	1.93	52	26.4	72	13
	30	1.58	49	26.4	72	14
	40	2.19	51	26.1	70	13
HSA + PhAA	35	1.95	52	26.4	71	13
	30	1.6	50	26.0	67	12
	40	2.08	49	26.3	67	15
HSA + IDS	35	1.85	42	26.5	67	15
	30	1.58	49	26.1	71	16
	25.2	1.26	47	26.3	73	19
HSA-urea	22.2	1.11	47	26.5	(86)*	(13)*
	18.9	0.95	47	26.4	(99)*	(9)*
I = 150 mM†						
pure HSA		1.89	44	25.2	-	-
HSA + PhAA	40	2.12	50	25.8	-	-
HSA + IDS		2.02	47	25.8	-	-
HSA-urea	25.2	1.03	38	25.3	-	-

† A diameter d and a charge valency $|Z|$ cannot be determined, as structure factor is considerably screened by the high concentration of salt in the solution.

* Due to the high uncertainties of these values, they are not taken into consideration in the interpretation of the data.

comparison to very stable values of R_g at 10 mM salt.

An impact of urea modification or toxin uptake on the structure of HSA is not reflected in the results of the fits. This finding is confirmed when looking at the Kratky plot in Figure 6.20. No significant difference between pure HSA samples, HSA complexed with toxins or urea modified HSA samples are observed. This result allows the interpretation of ITC measurements in the previous Sections as the heat signals consequently originate only from the binding process.

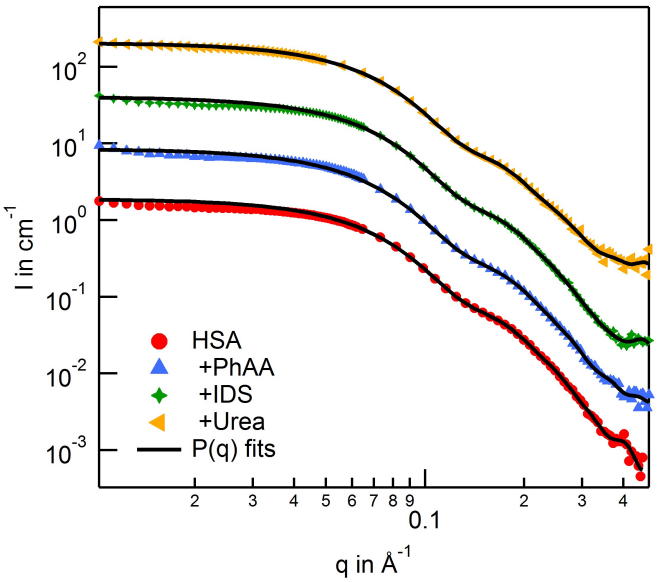

Figure 6.19: Scattering data of 40 g/L HSA with different additives at I = 150 mM. Native HSA (red circles) are compared to HSA sample with different additives: PhAA (blue triangles), IDS (green crosses), and urea modified samples (yellow triangles). A pure form factor fit is shown as black line. The concentration of urea modified HSA is 25.2 g/L.

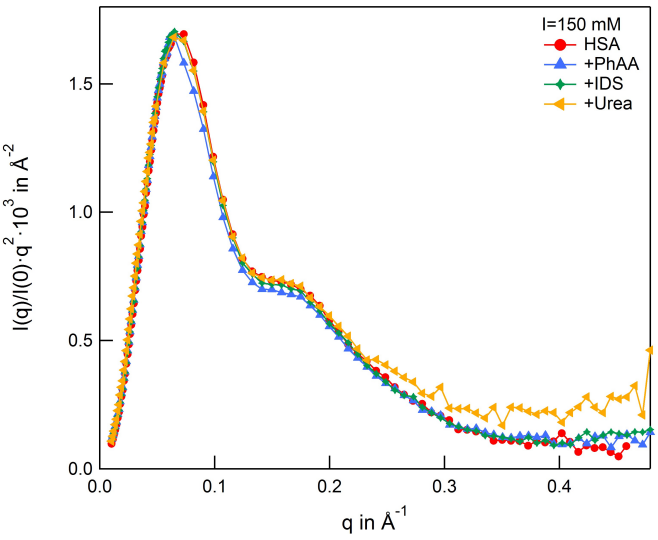

Figure 6.20: Kratky plot of the scattering data shown in Figure 6.19. The scattering profiles were normalized to I_0 prior to enable a comparison between the different concentrations.

The interaction between proteins in solution can be well characterized by SANS by analyzing the structure factor of the scattering intensities. While the structure of HSA remains insensitive to toxin adsorption or urea modification, small differences in the interaction potential between the urea modified HSA sample to all other measured samples were detected by SANS. In the present study this effect is seen in a change of the parameter $|Z|$ from 14 to 19 upon urea modification. It is known from literature that urea will induce carbamylation of certain residues [39, 201] and thus a possible influence on the interaction between the proteins cannot be excluded. Furthermore, the results in the present Section indicate that such an influence is not distinctly observed by the uptake of the other two toxins.

7 Summary

The studies presented in this thesis are aimed at understanding binding mechanisms and underlying driving forces for the interaction of ligands to the most abundant blood protein human serum albumin (HSA). The combination of a calorimetric with a scattering technique allows comprehensive insight into the binding process combining thermodynamic with structural information. Two different types of ligands were presented, both of them representing different important binding mechanisms and driving forces:

- The first model ligand is a short and weak acidic polyelectrolyte (PE) with 25 repeating monomers, each containing a carboxyl group, to explore charge-charge interactions. At physiological pH both interacting partners are negatively charged and form a soluble PE-protein complex as presented in the first part of the present thesis. Systematic ITC experiments exploring both effects of changing temperature and salinity gave clear evidence of an one-to-one binding of the polyelectrolyte PAA to HSA. A significant increase of binding affinity K_b with increasing temperature was found. On the dependency on salinity, a decrease of ΔG_b with increasing ionic strength was observed and the interaction vanishes for as high salinity as approximately 600 mM. The analysis of the binding affinity and its dependency on salt concentration reveal that three ions are released upon binding. This finding together with the measured endothermic enthalpy of reaction and a favorable change of entropy gave clear evidence that the strong binding is driven by the counterion release effect. Theoretical computational simulations support these results, counting in average 2.5 ions released upon binding which contribute significantly to the overall binding free energies. Finally, the total binding free energies deduced by simulations ΔG_b^{sim} are in good agreement with experimental results.
- To investigate possible structural modifications of native HSA after complexation with PAA, neutron scattering experiments were conducted first on pure HSA solutions under different ionic strength conditions. These reference experiments revealed minor changes of the tertiary structure when increasing salt concentration in the solution. Furthermore, the average scattering length $\bar{\rho}$ and radius of gyration at infinity contrast $R_{g,\infty}$ were determined from contrast variation experiments. $R_{g,\infty}$ was found to be slightly larger than the values at maximum contrast. Additionally, studies comparing HSA isolated from healthy individuals and patients suffering from CKD give evidence that pathologically modified HSA possibly lead to an altered protein surface charge and thus induce aggregation. With the structure of native HSA clarified, the effect of PAA adsorption on the protein was studied under high and low ionic strength conditions. The obtained results reveal a preserved protein structure upon adsorption of PAA.

- The second part of the thesis is devoted to the adsorption of uremic toxins to HSA. Unlike the polyeletrolyte, the two toxins studied bear only one charged moiety and a hydrophobic benzene group. The thermodynamic analysis of the binding reveals that there are two binding sites for both the the toxins with different binding affinities and stoichiometry. For phenylacetic acid (PhAA) the ionic strength dependence was analyzed using a Debye-Hückel approach. [182] The analysis demonstrated that binding is driven by a favorable hydrophobic interaction that yield constant binding free energies ΔG_b over the investigated range of temperature and ionic strength. This in turn indicates that enthalpy-entropy compensation (EEC) occurs, where the binding of a ligand in a cavity leads to an unfavorable change of entropy but is compensated by a favorable enthalpy contribution due to the release of water moleculs. [202, 203] Finally, in vitro modifications of HSA by urea do not alter the interaction between protein and toxin and has only minor influence on the binding affinities.

- Neutron scattering results again confirm a stable protein structure upon adsorption. Investigation of high concentrated solutions of HSA-ligand complexes reveal no significant change in interaction between the loaded proteins upon adsorption of the toxins. The urea modified proteins however, exhibit an increase of effective charge from -14 e to -19 e.

In conclusion, the present thesis has contributed to an in-depth understanding of the interaction between ligands/polyelectrolytes with proteins and identified the different driving contributions that leads to binding. These insights help to elucidate the nephrological relevant problem of toxin adsorption to HSA and thus cleared the path to improve renal dialysis techniques. In particular, combining computer simulations with calorimetry provide an accurate picture of binding mechanisms and driving forces. These insights can form the basis for more general predictions to address biochemical challenges such as drug targeting and delivering problems.

8 Appendix

8.1 Sample preparation and protein characterization

Materials. All materials were purchased Sigma-Aldrich® (Schnelldorf, Germany). The buffer morpholin-N-oxide (MOPS) and the uremic toxins phenylacetic acid (PhAA) and indoxyl sulfate potassium salt (IDS) were used as received. The polyelectrolyte polyacrylic acid (PAA) with MW = 1800 g/mol was dialysed for several weeks to match pH without changing ionic strength in the system. Human serum albumin (HSA) (lyophilized powder, fatty acid free, globulin free, 99%) with molecular weights of approximately MW = 66,200 - 66,400 g/mol according to Sigma-Aldrich, was also dialyzed prior to its use and the concentration afterwards determined by UV-vis spectroscopy as shown in Figure 8.2. The density of the protein was determined to 1.3 g/L using the density meter DMA 602 by Anton Paar (Graz, Austria).

In vitro urea modification of albumin. *In vitro* modification of HSA was carried out in a 10 mM MOPS buffer solution with 15 g/l HSA and 10 mM urea at 37°C and pH 7.2 for 18 h. After incubation, the mixture was dialyzed against buffer using centrifugation dialysis several times. Concentrations were then determined by UV-vis.

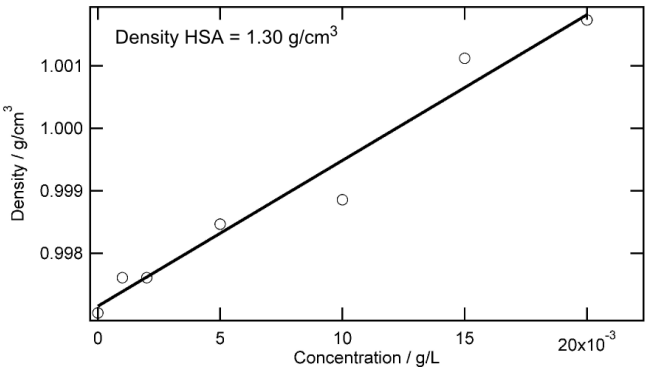

Figure 8.1: Density of HSA was determined by measuring a series of HSA solutions at 37°C and pH 7.2 using a density meter.

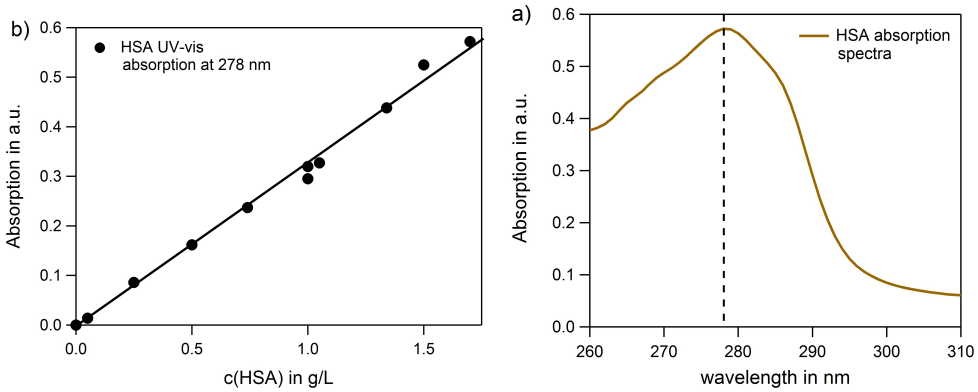

Figure 8.2: UV-vis measurement of a series of HSA concentrations. (a) A representative HSA (1.7 g/L) absorption spectra with an characteristic peak at 278 nm. (b) The absorption value at 278 nm was measured for different HSA concentrations and fitted with a line. These reference measurements were the basis to determine HSA concentrations.

8.2 Small-angle neutron scattering

To elucidate the limits in performance of the programs, the following theoretical experiments were conducted and depicted in Figure 8.3:
Based on the known crystallographic data of HSA[1], Cryson was used to calculate theoretical scattering intensities (yellow circles) for q values in the range of $0 < q < 1$ Å^{-1} (see Figure 8.3). Different q-ranges of these intensities were then used as input for Gnom to evaluate the effect of different boundary conditions for D_{max}. The impact of two different input values for q on the fitting results of Gnom, specifically a short $0 < q < 0.2$ Å^{-1} (blue lines) and a long $0 < q < 1$ Å^{-1} (green lines) q-range is demonstrated in Figure 8.3. Furthermore, these two ranges were analyzed in combination with the choice of two typical values for $D_{max} = 70$ Å (solid line) and 85 Å (broken line). The boundary condition $P(r = 0) = 0$ was set for all calculations.
The most significant deviation of the Gnom fit from the calculated intensities is observed in the high q-range beyond approximately 0.3 Å, where the full q-range is used as input to Gnom. This range is magnified in the inset of Figure 8.3a) and it is here, where the effect of different D_{max} comes into play. While the choice of D_{max} (with the border condition $p(D_{max}) = 0$) does not affect the quality of the fit for short q-ranges, its impact on the high q-range clearly evolves (green dashed and solid lines). For HSA as seen by crystallography, D_{max}=85 Å is a good approximation, which is also reflected in the $P(r)$ profiles (Figure 8.3b)). Here, the dashed lines show an overall more smooth profile than the solid lines, where $D_{max} = 70$ Å is an apparently too small estimate.

As mentioned before, Gnom uses the Equation (5.5) to calculate $I(0)$ and R_g. The according values for the four fits are listed in Table 8.1 below. Apparently, both radii and forward scattering intensities are robust results, not very sensitive to the available q-range and D_{max}.

[1]PDB-ID: 1AO6 taken from [169]

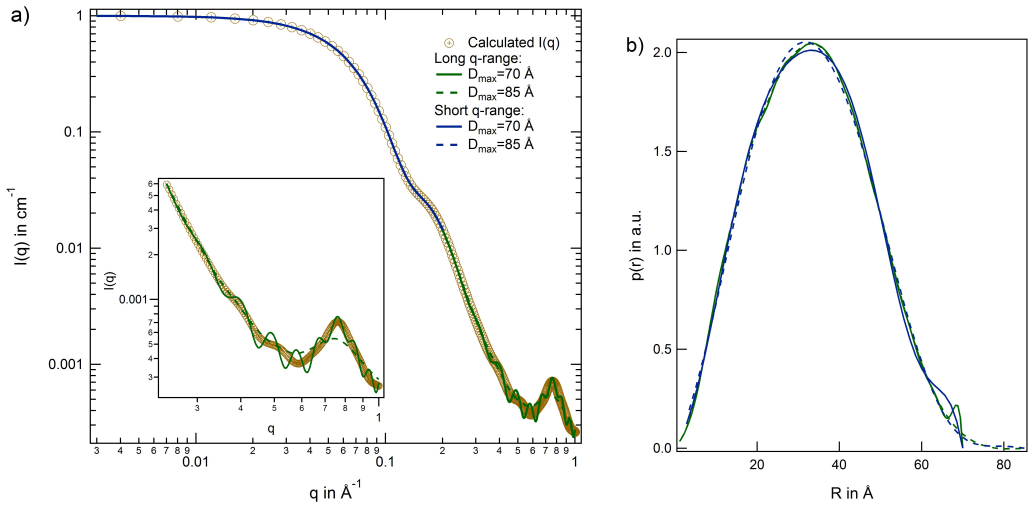

Figure 8.3: Effect of different input data on the result of Gnom data evaluation. Different fits for a calculated scattering intensity are compared in a standard log-log plot in (a), where the inset shows a magnified view of the high q range. PDDF profiles calculated by Gnom for the different profiles are displayed in (b).

This finding is not surprising, as the region contributing to the analysis $q < 0.041 < D_{max}/\pi$ is an order of magnitude below the short q-range data.

Table 8.1: Effect of q-range input and the choice of D_{max} on the evaluation by Gnom. Fit results $I(0)$ and R_g are summarized in dependence on different q-ranges and D_{max}.

q range in Å^{-1}	D_{max} in Å	R_g in Å	$I(0)$ in cm^{-1}
0 - 0.2	70	25.51	0.9998
	85	25.53	1
0 - 1	70	25.5	0.9998
	85	25.52	1

The difference in scattering at each instrument is reviewed in the following. HSA solution prepared in MOPS buffer and ionic strength 150 mM were measured at three instruments: V16, D11 and KSW II. As elucidated in Section 4.2.1, two of these instruments use monochromatic sources, while one (V16 @ HZB) use a spectrum of neutron wavelengths. The subtle difference in scattering profiles measured using different techniques is made visible in the Kratky plot in Figure 8.4. Intensities at the monochromatic instruments D11 and KSW II coincide very well, while deviation is seen in the HSA profile measured at V16. This can be explained by the effect of wavelength smearing that is described by $\Delta\lambda/\lambda$. However, a quantification of this value is experimentally very difficult. The effect is reflected in the second shoulder, which is less pronounced and more "smeared" in the data measured at V16, compared to the other two and the theoretical profile. A further observation correlated to the different smearing of the instruments is made for the fitted R_g values. While R_g is very similar for the two monochromatic instruments, the value obtained from the profile of

the TOF instrument is slightly smaller. However, the difference is subtle and at the edge of resolution of the technique in general.

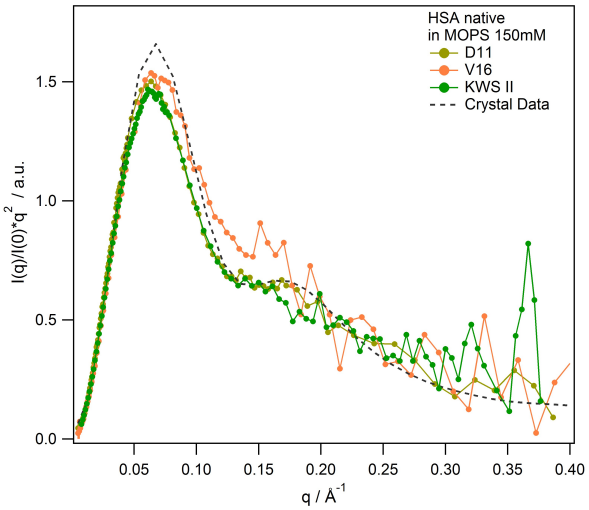

Figure 8.4: Native HSA in 150 mM salt and buffer solution at 37°C. A Kratky plot reveals subtle differences in scattering data obtained at different instruments.

The forward scattering intensities I_0 obtained at different concentration and instruments are evaluated and plotted against concentration in Figure 8.5. The dashed line is a fit with $I(q = 0) = 0$ and confirm a linear relationship as expected from Equation (3.52). However, the error bars are relatively large (see Table 5.3) and deviation at higher concentration (at a volume fraction of about 1%) may be explained by the presence of contributing structure factor that will influence the determination of I_0.

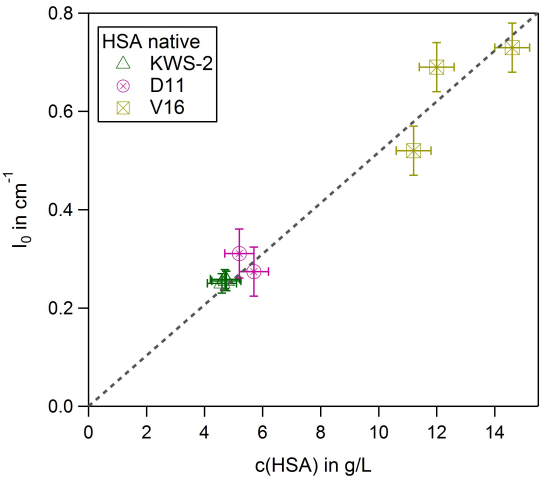

Figure 8.5: Fitted primary intensity I_0 of HSA in different buffer solution. Measurements were performed at different facilities.

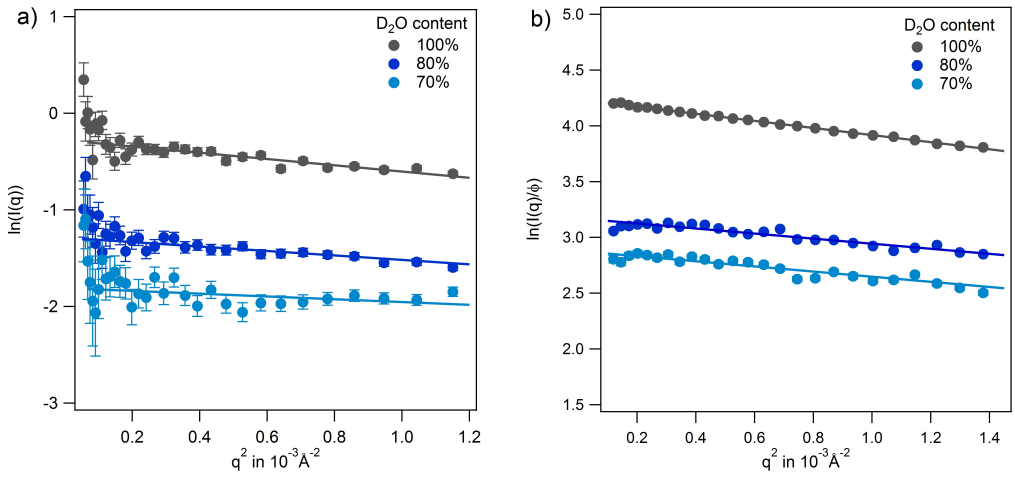

Figure 8.6: Guinier fits (lines) of scattering data shown in Figure 5.14 for the low q range with (a) I = 25 mM and (b) I = 150 mM. The derived values for $I(0)$ and R_g are listed in Table 5.4.

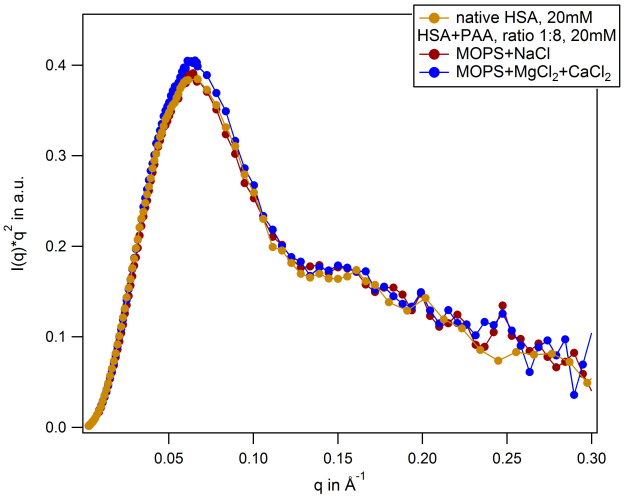

Figure 8.7: Kratky plot of HSA-PAA complexes in comparison to native HSA. The molar ratio of the complexes are 1:8 HSA to PAA. While MOPS was used as buffer, ionic strength was adjusted with two types of salt, which are monovalent NaCl (red) and divalent $MgCl_2$+$CaCl_2$ (blue).

8.3 Polyelectrolyte binding to HSA

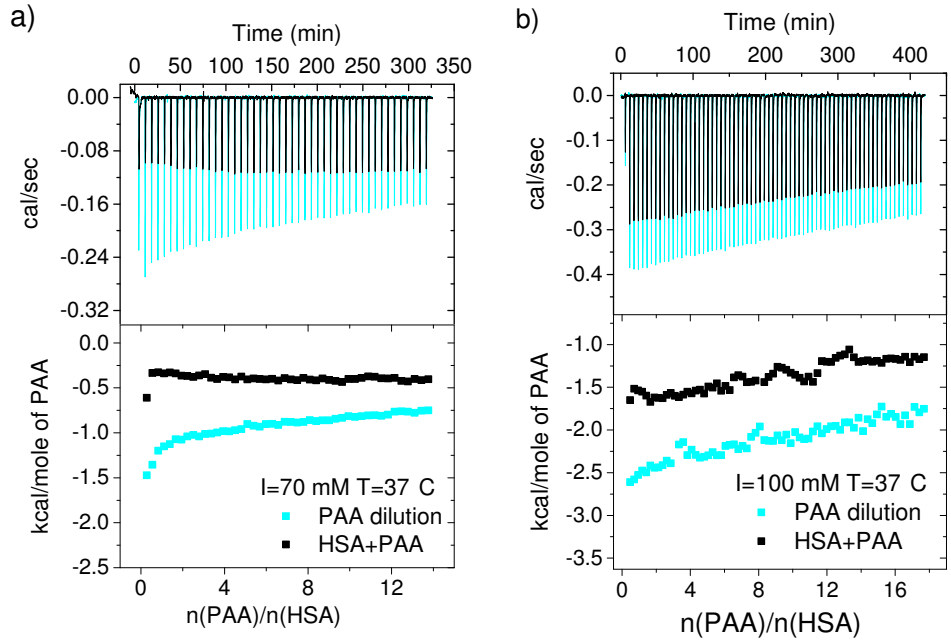

Figure 8.8: Raw ITC data and integrated heats are shown for a) I = 70 mM and b) 100 mM at T = 37°C.

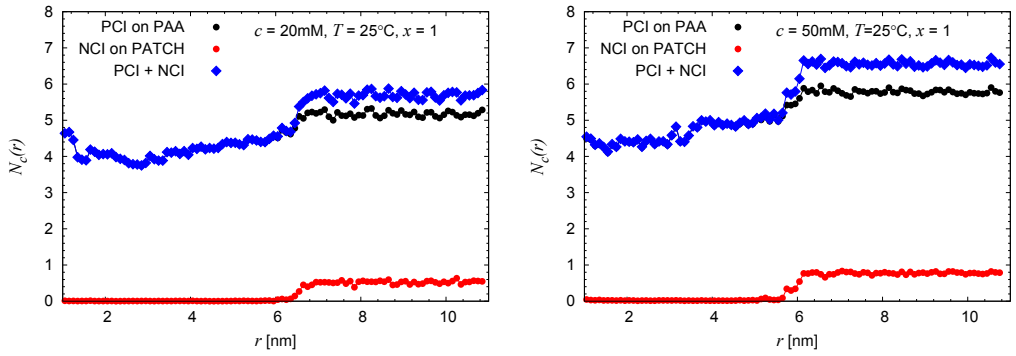

Figure 8.9: Number of positive condensed ions (PCI) and negative condensed ions (NCI) versus distance for ionic strength I = 20 mM (left) and 50 mM at a temperature of 25°C.

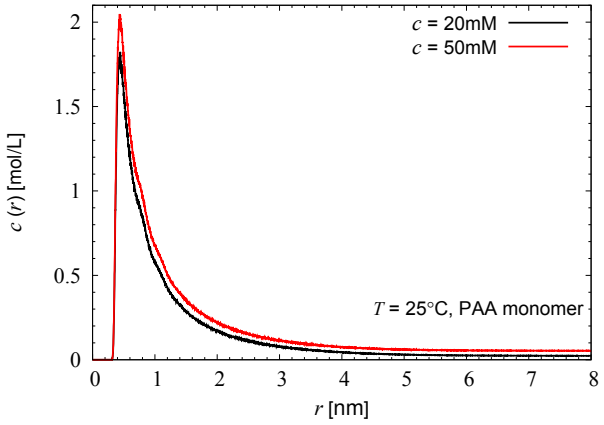

Figure 8.10: Density profiles of positive salt ions around the PAA monomers at 20 and 50 mM salt concentration. In the binding layer of condensed ions $r < 0.5$ nm the ion concentration is about 1.5 M.

8.4 Interaction of uremic toxins with HSA

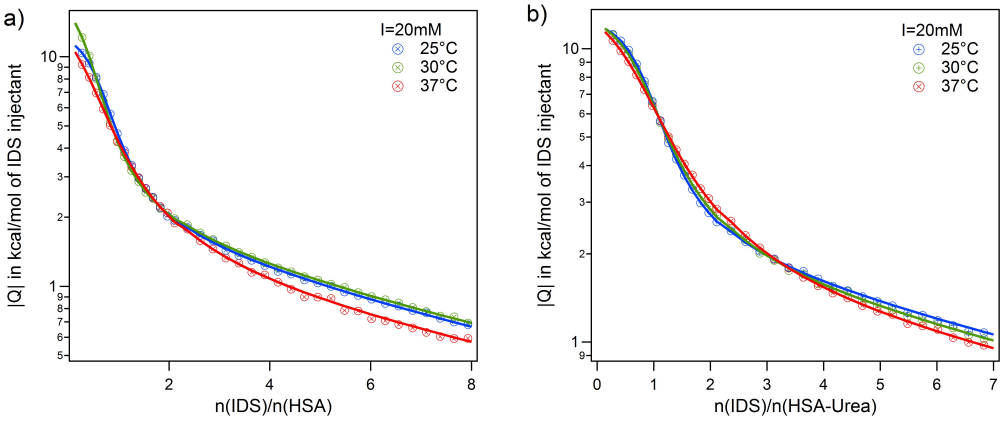

Figure 8.11: Adsorption of IDS to native and modified HSA. Temperature series measured at I = 20 mM and according fits using the TSIS model are shown for (a) native HSA (b) urea modified HSA.

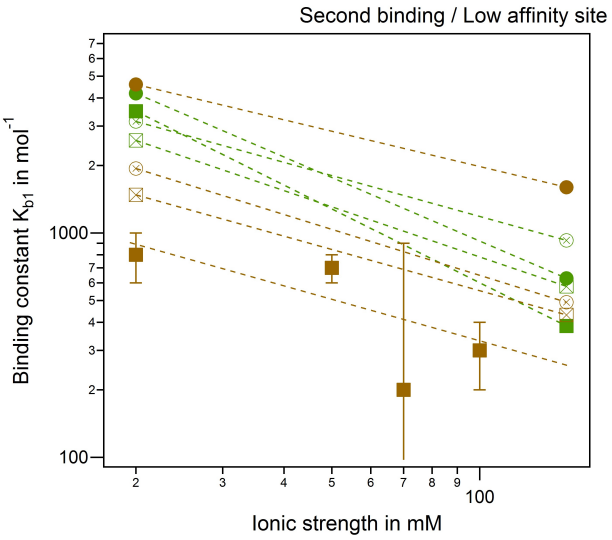

Figure 8.12: Ionic strength dependence of the second binding process and low affinity site. Adsorption of of PhAA (brown) and IDS (green) to native (full symbols) and modified HSA (empty symbols) are shown. Spheres and rectangles represent 25°C and 37°C.

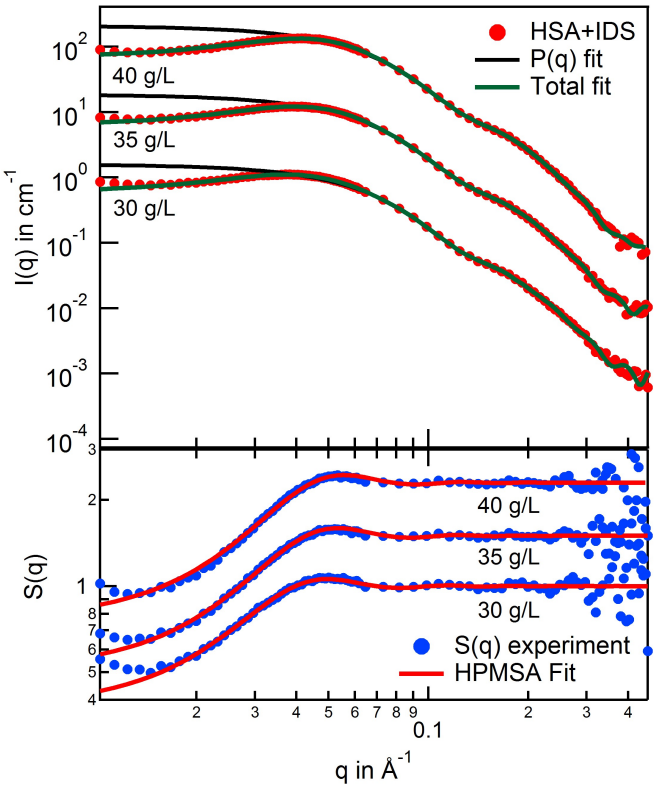

Figure 8.13: Scattering intensities of the HSA-IDS complex at different concentrations. Top panel depict measured experimental data (red points) with corresponding $P(q)$ (black line) and total fits (green line) plotted on top. Bottom panel shows experimental (blue circles) and fitted structure factor (red line). Data are scaled for better comparison.

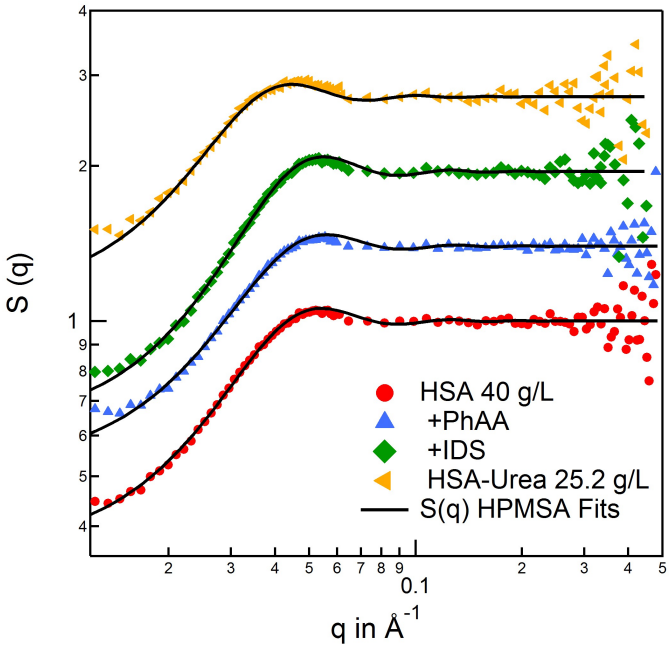

Figure 8.14: Structure factor fits for all samples measured at highest concentration 40 g/L and 25.2 g/L for urea modified HSA. The data are shifted relative to native HSA data by constant offsets of 0.5, 1 and 1.5 respectively.

Table 8.2: Table comparing different methods to study binding between proteins P and ligands L.

	ITC	FS	ED	UF	UC	SPR	CE
Sample manipulation	none	labelling	none	none	immob.	none	
Multiple binding sites	yes	yes	yes	yes	yes	no	yes
Kinetics	none	yes	none	none	none	yes	yes
Sample volume	P:1-1.4 mL L:250-300 μL	0.5 mL 0.5 mL	0.5-1 mL	0.5-1 mL	0.5-1 mL	30-500 μL	nL
Sample conc.	P: 5-100 μM L: mM	P:mM-μM	μM	μM-mM	mM	L:μM P:50-100μg	μM
Affinity range k_b in mol^{-1}	10^3-10^9	10^3-10^{10}	10^2-10^{12}	10^2-10^8	10^3-10^8	10^6-10^{11}	10^2-10^7
Information	K_b, n, ΔH ΔG_b, ΔS_b, ΔC_p	K_b, n	K_b, binding site	K_b, n	K_b, n	K_b, n,$k_{\text{on}}/k_{\text{off}}$	K_b, n
Advantages	• full thermodyn. information • no sample manipulation • precision, robust	• kinetic data • low sample conc. • can measure high affinities	• simple • inexpensive	• simple • fast	• simple • no membrane involved	• kinetic data • small sample amount • reproducibility	• small sample amount • rapid & simple • high efficiency
Drawbacks	• exp. setup depends on interest • complicated analysis • all processes contribute	• labelling • uncertain n • indirect method	• volume shifts • NSB* • Donnan effect • NPC*	• volume shift • NSB* • disturbed equilibrium • NPC*	• sedimentation • back diffusion • viscosity • low throughput • NPC*	• immobilization • stoichometry not directly measured	• protein adsorp. on walls • low sensitivity of UV signal

ITC: Isothermal titration calorimetry; FS: Fluorescence spectroscopy; ED: Equilibrium dialysis; UF: Ultrafiltration; UC: Ultracentrifugation; SPR: Surface plasmon resonance-based assays; CE: Capillary electrophoresis

* NSB: nonspecific binding, NPC: no physiological condition

List of Tables

Bibliography

[1] F. Kratz. “Albumin as a drug carrier: Design of prodrugs, drug conjugates and nanoparticles”. *J. Controlled Release* 132 (2008), pp. 171–183.

[2] A. L. Hopkins et al. “The role of ligand efficiency metrics in drug discovery”. *Nat. Rev. Drug Discovery* 13 (2014), pp. 105–121.

[3] Q. Wei et al. “Protein Interactions with polymer coatings and biomaterials”. *Angewandte Chemie - International Edition* 53.31 (2014), pp. 8004–8031.

[4] S. Geschwindner, J. Ulander, and P. Johansson. “Ligand Binding Thermodynamics in Drug Discovery: Still a Hot Tip?” *J. Med. Chem.* 58.16 (2015), pp. 6321–6335.

[5] S. Liabeuf, T. B. Drüeke, and Z. a. Massy. “Protein-bound uremic toxins: New insight from clinical studies”. *Toxins* 3.7 (2011), pp. 911–919.

[6] M. A. Williams. “Protein–Ligand Interactions: Fundamentals”. 2013, pp. 3–34.

[7] Y. Zhang, H. F. Chan, and K. W. Leong. “Advanced materials and processing for drug delivery: The past and the future”. *Adv. Drug Delivery Rev.* 65.1 (2013), pp. 104–120.

[8] L. B. Peppas. “Recent advances on the use of biodegradable microparticles and nanoparticles in controlled drug-delivery”. *Int. J. Pharm.* 116.1 (1995), pp. 1–9.

[9] K. S. Soppimath et al. “Biodegradable polymeric nanoparticles as drug delivery devices”. *J. Controlled Release* 70.1-2 (2001), pp. 1–20.

[10] Y. Xu et al. “Protein purification by polyelectrolyte coacervation: influence of protein charge anisotropy on selectivity.” *Biomacromolecules* 12.5 (2011), pp. 1512–22.

[11] X. Guo and M. Ballauff. “Spherical polyelectrolyte brushes: Comparison between annealed and quenched brushes”. *Physical Review E* 64.5 (2001), p. 051406.

[12] R. A. Petros and J. M. DeSimone. “Strategies in the design of nanoparticles for therapeutic applications”. *Nat. Rev. Drug Discovery* 9.8 (2010), pp. 615–627.

[13] T. Cedervall et al. “Understanding the nanoparticle – protein corona using methods to quantify exchange rates and affinities of proteins for nanoparticles”. *Proc. Natl. Acad. Sci.* 104.7 (2007), pp. 2050–1055.

[14] M. Lundqvist et al. “Nanoparticle size and surface properties determine the protein corona with possible implications for biological impacts”. *Proc. Natl. Acad. Sci.* 105.38 (2008), pp. 14265–14270.

[15] C. Chen et al. “Advanced nuclear analytical and related techniques for the growing challenges in nanotoxicology”. *Chemical Society Reviews* 42.21 (2013), p. 8266.

[16] A. B. Kayitmazer et al. “Protein-polyelectrolyte interactions”. *Soft Matter* 9.9 (2013), pp. 2553–2583.

[17] A. L. Becker et al. “Proteins and polyelectrolytes: A charged relationship”. *Curr. Opin. Colloid Interface Sci.* 17.2 (2012), pp. 90–96.

[18] S Curry et al. “Crystal structure of human serum albumin complexed with fatty acid reveals an asymmetric distribution of binding sites.” *Nat. Struct. Mol. Biol.* 5.9 (1998), pp. 827–35.

[19] M. Fasano et al. “The extraordinary ligand binding properties of human serum albumin.” *IUBMB Life* 57.12 (2005), pp. 787–96.

[20] S. Barbosa, P. Taboada, and V. Mosquera. “Analysis of the interactions between human serum albumin/amphiphilic penicillin in different aqueous media: an isothermal titration calorimetry and dynamic light scattering study”. *Chem. Phys.* 310.1-3 (2005), pp. 51–58.

[21] J Jankowski et al. “Increased plasma phenylacetic acid in patients with end-stage renal failure inhibits iNOS expression”. *J. Clin. Invest.* 112 (2003), pp. 256–264.

[22] Y. Itoh et al. “Protein-bound uremic toxins in hemodialysis patients measured by liquid chromatography/tandem mass spectrometry and their effects on endothelial ROS production”. *Anal. Bioanal.Chem.* 403.7 (2012), pp. 1841–1850.

[23] E. Devine et al. “Binding affinity and capacity for the uremic toxin indoxyl sulfate”. *Toxins* 6 (2014), pp. 416–430.

[24] T. Sakai et al. “Interaction mechanism between indoxyl sulfate, a typical uremic toxin bound to site II, and ligands bound to site I of human serum albumin”. *Pharm. Res.* 18.4 (2001), pp. 520–524.

[25] L. Viaene et al. “Albumin is the main plasma binding protein for indoxyl sulfate and p-cresyl sulfate.” *Biopharm. Drug Dispos.* 34.3 (2013), pp. 165–75.

[26] R. Vanholder et al. “Review on uremic toxins : Classification , concentration , and interindividual variability”. *Kidney Int.* 63 (2003), pp. 1934–1943.

[27] T. Sakai, A. Takadate, and M. Otagiri. “Characterization of Binding Site of Uremic Toxins on Human Serum Albumin”. *Biol. Pharm. Bull.* 18 (1998), pp. 1755–1761.

[28] P. Gulyassy and T. Depner. “Impaired binding of drugs and endogenous ligands in renal diseases.” *Am. J. Kidney Dis.* 2 (1983), pp. 578–601.

[29] F. Brettschneider et al. “Removal of protein-bound, hydrophobic uremic toxins by a combined fractionated plasma separation and adsorption technique.” *Artif. Organs* 37.4 (2013), pp. 409–16.

[30] F. Boehringer, V. Jankowski, and P. R. Gajjala. “Release of Uremic Retention Solutes from Protein Binding by Hypertonic Predilution Hemodiafiltration”. *ASAIO J.* 61.1 (2015), pp. 55–60.

[31] N. Zaidi et al. “A comprehensive insight into binding of hippuric acid to human serum albumin: a study to uncover its impaired elimination through hemodialysis.” *PLoS One* 8.8 (2013), e71422.

[32] X. Li and Z. Yang. “Interaction of oridonin with human serum albumin by isothermal titration calorimetry and spectroscopic techniques”. *Chem. Biol. Interact.* 232 (2015), pp. 77–84.

[33] B. K. Paul, N. Ghosh, and S. Mukherjee. “Interplay of Multiple Interaction Forces: Binding of Norfloxacin to Human Serum Albumin”. *J. Phys. Chem. B* 119.41 (2015), pp. 13093–13102.

[34] M. Ishtikhar, G. Rabbani, and R. H. Khan. “Interaction of 5-fluoro-5’-deoxyuridine with human serum albumin under physiological and non-physiological condition: a biophysical investigation.” *Colloids Surf. B, Biointerfaces* 123 (2014), pp. 469–77.

[35] N. Keswani, S. Choudhary, and N. Kishore. “Interaction of weakly bound antibiotics neomycin and lincomycin with bovine and human serum albumin: biophysical approach.” *J. Biochem.* 148.1 (2010), pp. 71–84.

[36] J. Jankowski et al. “Method of dialysis for removing protein-bound toxins from the blood of patients using high-frequency electromagnetic fields”. Pat. 19. 2014.

[37] T. J. Dengler, G. M. Rohertz-Vaupel, and H. J. Dengler. “Albumin binding in uraemia: quantitative assessment of inhibition by endogenous ligands and carbamylation of albumin”. *European Journal of Clinical Pharmacology* 43.5 (1992), pp. 491–499.

[38] M. Rossi et al. “Protein-bound uremic toxins, inflammation and oxidative stress: A cross-sectional study in stage 3-4 chronic kidney disease”. *Arch. Med. Res.* 45.4 (2014), pp. 309–317.

[39] A. H. Berg et al. “Carbamylation of Serum Albumin as a Risk Factor for Mortality in Patients with Kidney Failure”. *Sci. Transl. Med.* 5.175 (2013).

[40] C. G. de Kruif, F. Weinbreck, and R. de Vries. “Complex coacervation of proteins and anionic polysaccharides”. *Current Opinion in Colloid & Interface Science* 9.5 (2004), pp. 340–349.

[41] E. Kizilay, A. B. Kayitmazer, and P. L. Dubin. “Complexation and coacervation of polyelectrolytes with oppositely charged colloids”. *Advances in Colloid and Interface Science* 167.1 (2011), pp. 24–37.

[42] C. Cooper et al. “Polyelectrolyte–protein complexes”. *Current Opinion in Colloid & Interface Science* 10.1-2 (2005), pp. 52–78.

[43] B. K. Nfor et al. “Design strategies for integrated protein purification processes: Challenges, progress and outlook”. *J Chem. Technol. Biotechnol.* 83.2 (2008), pp. 124–132.

[44] R. a. Silva et al. “Protein adsorption onto polyelectrolyte layers: effects of protein hydrophobicity and charge anisotropy.” *Langmuir* 26.17 (2010), pp. 14032–8.

[45] X. Du et al. “Protein-selective coacervation with hyaluronic acid.” *Biomacromolecules* 15.3 (2014), pp. 726–34.

[46] S. Zeng et al. “Protein binding for detection of small changes on a nanoparticle surface.” *The Analyst* 139.6 (2014), pp. 1364–71.

[47] V. K. Mudhivarthi et al. “Ultra-stable hemoglobin–poly(acrylic acid) conjugates”. *J. Mater. Chem.* 22.38 (2012), p. 20423.

[48] Y. Lu and M. Ballauff. “Thermosensitive core–shell microgels: From colloidal model systems to nanoreactors”. *Prog. Polym. Sci.* 36.6 (2011), pp. 767–792.

[49] K. Vuignier et al. “Drug-protein binding: a critical review of analytical tools”. *Anal. Bioanal. Chem* 398 (2010), pp. 53–66.

[50] V. Ball and C. Maechling. “Isothermal microcalorimetry to investigate non specific interactions in biophysical chemistry.” *Int. J. Mol. Sci.* 10.8 (2009), pp. 3283–315.

[51] E. Omanovic-Miklicanin, I. Manfield, and T. Wilkins. “Application of isothermal titration calorimetry in evaluation of protein–nanoparticle interactions”. *J. Therm. Anal. Calorim.* 127 (2017), pp. 605–613.

[52] F. Biedermann and H.-J. Schneider. “Experimental Binding Energies in Supramolecular Complexes”. *Chem. Rev.* (2016), acs.chemrev.5b00583.

[53] V Ball et al. “Complexation Mechanism of Bovine Serum Albumin and Poly (allylamine hydrochloride)”. *J. Phys. Chem. B* 106 (2002), pp. 2357–2364.

[54] K. Henzler et al. “Adsorption of -Lactoglobulin on Spherical Polyelectrolyte Brushes: Direct Proof of Counterion Release by Isothermal Titration Calorimetry”. *J. Am. Chem. Soc.* 132.19 (2010), pp. 3159–3163.

[55] E. Seyrek et al. “Ionic strength dependence of protein-polyelectrolyte interactions.” *Biomacromolecules* 4.2 (2003), pp. 273–82.

[56] N. Welsch et al. “Adsorption of proteins to functional polymeric nanoparticles”. *Polymer* 54.12 (2013), pp. 2835–2849.

[57] X. Du et al. “Insights into Protein–Ligand Interactions: Mechanisms, Models, and Methods”. *Int. J. Mol. Sci.* 17.2 (2016), p. 144.

[58] R. Matsuda et al. “Studies of metabolite-protein interactions: a review.” *Journal of Chromatography. B* 966 (2014), pp. 48–58.

[59] a. a. Bhattacharya, T Grüne, and S Curry. “Crystallographic analysis reveals common modes of binding of medium and long-chain fatty acids to human serum albumin.” *J. Mol. Biol.* 303.5 (2000), pp. 721–32.

[60] S. Chodankar et al. “Structural study of coacervation in protein-polyelectrolyte complexes”. *Physical Review E* 78.3 (2008), p. 031913.

[61] M Kornreich, R Avinery, and R Beck. “Modern X-ray scattering studies of complex biological systems.” *Curr. Opin. Biotechnol.* 24.4 (2013), pp. 716–23.

[62] J. Gummel, F. Cousin, and F. Boué. “Structure Transition in PSS/Lysozyme Complexes: A Chain-Conformation-Driven Process, as Directly Seen by Small Angle Neutron Scattering”. *Macromolecules* 41.8 (2008), pp. 2898–2907.

[63] K. Henzler et al. "Adsorption of bovine hemoglobin onto spherical polyelectrolyte brushes monitored by small-angle X-ray scattering and Fourier transform infrared spectroscopy." *Biomacromolecules* 8.11 (2007), pp. 3674–81.

[64] D. a. Jacques and J. Trewhella. "Small-angle scattering for structural biology–expanding the frontier while avoiding the pitfalls." *Protein Sci* 19.4 (2010), pp. 642–57.

[65] J. Lipfert and S. Doniach. "Small-angle X-ray scattering from RNA, proteins, and protein complexes." *Annu. Rev. Biophys. Biomol. Struct.* 36 (2007), pp. 307–27.

[66] M. H. J. Koch, P. Vachette, and D. I. Svergun. *Small-angle scattering: a view on the properties, structures and structural changes of biological macromolecules in solution*. Vol. 36. 2. 2003, pp. 147–227.

[67] K. Henzler et al. "Directed Motion of Proteins along Tethered Polyelectrolytes". *Phys. Rev. Lett.* 100.15 (2008), p. 158301.

[68] K. Henzler et al. "Interaction strength between proteins and polyelectrolyte brushes: a small angle X-ray scattering study". *Physical Chemistry Chemical Physics* 13.39 (2011), p. 17599.

[69] S. Rosenfeldt et al. "Interaction of proteins with spherical polyelectrolyte brushes in solution as studied by small-angle x-ray scattering". *Physical Review E* 70.6 (2004), p. 061403.

[70] D. I. Svergun and M. V. Petoukhov. "Analysis of X-ray and neutron scattering from biomacromolecular solutions". *Current Opinion in Strucutral Biology* 17 (2007), pp. 562–571.

[71] a. B. Kayitmazer et al. "Mesophase separation and probe dynamics in protein?polyelectrolyte coacervates". *Soft Matter* 3.8 (2007), p. 1064.

[72] M. B. Jackson. *Molecular and Cellular Biophysics*. Cambridge University Press, 2006.

[73] S. H. Strogatz. "Exploring complex networks". *Nature* 410.6825 (2001), pp. 268–276.

[74] T. J. Peters. *All about Albumin Biochemistry, Genetics, and Medical Application*. Academic Press, 1996.

[75] S Sugio et al. "Crystal structure of human serum albumin at 2.5 Å resolution". *Protein Eng.* 12.6 (1999), pp. 439–446.

[76] X. He and D. C. Carter. "Atomic structure and chemistry of HSA". *Nature* 358 (1992), pp. 209–214.

[77] K. J. Fehske, W. E. Müller, and U Wollert. "The location of drug binding sites in human serum albumin." *Biochem. Pharmacol.* 30.7 (1981), pp. 687–92.

[78] T. Peters. "Serum Albumin". *Adv. Protein Chem.* 37 (1985), pp. 161–245.

[79] G. Fanali et al. "Human serum albumin: From bench to bedside". *Mol. Aspects Med.* 33 (2012), pp. 209–290.

[80] O. K. Abou-Zied and N. Al-Lawatia. "Exploring the Drug-Binding Site Sudlow I of Human Serum Albumin: The Role of Water and Trp214 in Molecular Recognition and Ligand Binding". *Chem Phys Chem* 12 (2011), pp. 270–274.

[81] M. J. N. Junk, H. W. Spiess, and D. Hinderberger. "The distribution of fatty acids reveals the functional structure of human serum albumin." *Angew Chem Int Edit* 49 (2010), pp. 8755–8759.

[82] G Sudlow, D. Birkett, and D. Wade. "The characterization of two specific drug binding sites on human serum albumin." *Mol.Pharmacol.* 11.6 (1975), pp. 824–832.

[83] M. Dockal, D. C. Carter, and F. Ruecker. "The Three Recombinant Domains of Human Serum Albumin : Structural Characterization and Ligand Binding Properties". *J. Biol. Chem.* 274.41 (1999), pp. 29303–29310.

[84] J. Ghuman et al. "Structural basis of the drug-binding specificity of human serum albumin". *J. Mol. Biol.* 353.1 (2005), pp. 38–52.

[85] H. Watanabe et al. "Interaction between Two Sulfate-Conjugated Uremic Toxins, p -Cresyl Sulfate and Indoxyl Sulfate, during Binding with Human Serum Albumin". *Drug Metab. Dispos.* 40 (2012), pp. 1423–1428.

[86] J. T. Pedersen et al. "Affinity capillary electrophoresis for identification and investigation of human Gc-globulin (vitamin D-binding protein) and its isoforms interacting with G-actin." *Electrophoresis* 29 (2008), pp. 1723–33.

[87] T. Chatterjee et al. "Interaction of virstatin with human serum albumin: spectroscopic analysis and molecular modeling." *PLoS One* 7.5 (2012), e37468.

[88] C. Ràfols, S. Zarza, and E. Bosch. "Molecular interactions between some non-steroidal anti-inflammatory drugs (NSAID's) and bovine (BSA) or human (HSA) serum albumin estimated by means of isothermal titration calorimetry (ITC) and frontal analysis capillary electrophoresis (FA/CE)." *Talanta* 130 (2014), pp. 241–50.

[89] M. Howard et al. "Plasma Protein Binding in Drug Discovery and Development". *Comb. Chem. High Throughput Sceen.* 13.2 (2010), pp. 170–187.

[90] R Zini. *Methods in drug protein binding analysis. Human Pharmacology.* Ed. by T. J. P. Kuemmerle H Shibuya T. Elsevier Science Publishers, 1991, pp. 235–282.

[91] L. Fielding, S. Rutherford, and D. Fletcher. "Determination of protein-ligand binding affinity by NMR: Observations from serum albumin model systems". *Magn. Reson. Chem.* 43.6 (2005), pp. 463–470.

[92] P. Sun, A. Hoops, and R. A. Hartwick. "Enhanced albumin protein separations and protein—drug binding constant measurements using anti-inflammatory drugs as run buffer additives in affinity capillary electrophoresis". *J Chromatogr B: Biomed. Sci. Appl.* 661.2 (1994), pp. 335–340.

[93] G. Ascoli, C. Bertucci, and P. Salvadori. "Stereospecific and Competitive Binding of Drugs to Human Serum Albumin: A Difference Circular Dichroism Approach". *J Pharm. Sci.* 84.6 (1995), pp. 737–741.

[94] C. Dufour and O. Dangles. "Flavonoid–serum albumin complexation: determination of binding constants and binding sites by fluorescence spectroscopy". *Biochimica et Biophysica Acta* 1721.1 (2005), pp. 164–173.

[95] J. Østergaard et al. "Evalution of capillary electrophoresis-frontal analysis for the study of low molecular weight drug-human serum albumin interactions". *Electrophoresis* 23.17 (2002), pp. 2842–2853.

[96] B. Honore and R. Broersen. "Albumin binding of anti-inflammatory drugs. Utility of site-oriented versus a stoichiometric analysis". *Mol. Pharmacol.* 25 (1984), pp. 137–150.

[97] M. Montero, J. Estelrich, and O. Valls. "Binding of non-steroidal anti-inflammatory drugs to human serum albumin". *Int. J. Pharm.* 62.1 (1990), pp. 21–25.

[98] M Rueth et al. "Guanidinylations of albumin decreased binding capacity of hydrophobic metabolites". *Acta Physiol.* 215 (2015), pp. 13–23.

[99] M. Calderón et al. "Dendritic polyglycerols for biomedical applications." *Adv. Mater. (Deerfield Beach, Fla.)* 22.2 (2010), pp. 190–218.

[100] S Anandhakumar, V Nagaraja, and A. M. Raichur. "Reversible polyelectrolyte capsules as carriers for protein delivery." *Colloids Surf. B Biointerfaces* 78.2 (2010), pp. 266–74.

[101] I. Lee. "Molecular self-assembly: smart design of surface and interface via secondary molecular interactions." *Langmuir* 29.8 (2013), pp. 2476–89.

[102] G. R. Hendrickson and L. Andrew Lyon. "Bioresponsive hydrogels for sensing applications". *Soft Matter* 5.1 (2009), p. 29.

[103] M. Record, W. Zhang, and C. Anderson. "Analysis of effects of salts and uncharged solutes on protein and nucleic acid equilibria and processes: A practical guide to recognizing and interpreting polyelectrolyte effects, Hofmeister effects, and osmotic effects of salts". *Adv. Protein Chem.* 51 (1998), pp. 281–353.

[104] F. L. B. da Silva and B. Jönsson. "Polyelectrolyte–protein complexation driven by charge regulation". *Soft Matter* 5.15 (2009), p. 2862.

[105] K. W. Mattison, I. J. Brittain, and P. L. Dubin. "Protein-Polyelectrolyte Phase Boundaries". *Biotechnol. Prog.* 11.6 (1995), pp. 632–637.

[106] K. W. Mattison, P. L. Dubin, and I. J. Brittain. "Complex Formation between Bovine Serum Albumin and Strong Polyelectrolytes : Effect of Polymer Charge Density". *J. Phys. Chem. B* 102 (1998), pp. 3830–3836.

[107] C. G. D. Kruif, F. Weinbreck, and R. D. Vries. "Complex coacervation of proteins and anionic polysaccharides". *Curr Opin Colloid Interface Sci* 9 (2004), pp. 340–349.

[108] D. Guzey and D. J. McClements. "Characterization of beta-lactoglobulin-chitosan interactions in aqueous solutions: A calorimetry, light scattering, electrophoretic mobility and solubility study". *Food Hydrocolloids* 20 (2006), pp. 124–131.

[109] K. Giger et al. "Suppression of insulin aggregation by heparin". *Biomacromolecules* 9 (2008), pp. 2338–2344.

[110] B. B. Minsky, B. Zheng, and P. L. Dubin. "Inhibition of antithrombin and bovine serum albumin native state aggregation by heparin." *Langmuir : the ACS journal of surfaces and colloids* 30.1 (2014), pp. 278–87.

[111] P. L. Dubin, J. Gao, and K. Mattison. "Protein Purification by Selective Phase Separation with Polyelectrolytes". *Separation & Purification Reviews* 23.1 (1994), pp. 1–16.

[112] J. M. Park et al. "Effects of Protein Charge Heterogeneity in Protein-Polyelectrolyte Complexation". *Macromolecules1* 25 (1992), pp. 290–295.

[113] F. Roosen-Runge et al. "Interplay of pH and binding of multivalent metal ions: charge inversion and reentrant condensation in protein solutions." *J. Phys. Chem. B* 117.18 (2013), pp. 5777–87.

[114] W. M. de Vos et al. "Adsorption of the protein bovine serum albumin in a planar poly(acrylic acid) brush layer as measured by optical reflectometry." *Langmuir* 24.13 (2008), pp. 6575–84.

[115] A. L. Becker et al. "Adsorption of RNase A on cationic polyelectrolyte brushes: a study by isothermal titration calorimetry." *Biomacromolecules* 12.11 (2011), pp. 3936–44.

[116] P. van Rijn. "Polymer Directed Protein Assemblies". *Polymers* 5.2 (2013), pp. 576–599.

[117] M. T. Record, C. F. Anderson, and T. M. Lohman. "Thermodynamic analysis of ion effects on the binding and conformational equilibria of proteins and nucleic acids: the roles of ion association or release, screening, and ion effects on water activity". *Q. Rev. Biophys.* 11.02 (1973), p. 103.

[118] C. Yigit et al. "Like-charged protein-polyelectrolyte complexation driven by charge patches". *J Chem Phys* 143 (2015), p. 0649005.

[119] R. de Vries, F. Weinbreck, and C. G. de Kruif. "Theory of polyelectrolyte adsorption on heterogeneously charged surfaces applied to soluble protein–polyelectrolyte complexes". *J. Chem. Phys.* 118.10 (2003), p. 4649.

[120] S. J. de Carvalho, R. Metzler, and A. G. Cherstvy. "Critical adsorption of polyelectrolytes onto charged Janus nanospheres". *Phys. Chem. Chem. Phys.* 16 (29 2014), pp. 15539–15550.

[121] G. G. Hammes. *Thermodynamics and kinetics for the biological sciences*. Wiley-Interscience, John Wiley & Sons Inc, 2000.

[122] D. T. Haynie. *Biological Thermodynamics*. Cambridge University Press, 2001.

[123] J. Martinez and J Murciano-Calles. *Isothermal Titration Calorimetry: Thermodynamic Analysis of the Binding Thermograms of Molecular Recognition Events by Using Equilibrium Models*. 2013. Chap. 4.

[124] D. J. Winzor and C. M. Jackson. "Interpretation of the temperature dependence of equilibrium and rate constants". *J. Mol. Regocnit.* 19 (2006), pp. 299–304.

[125] I. Herrera and M. a. Winnik. "Differential binding models for isothermal titration calorimetry: Moving beyond the Wiseman isotherm". *J. Phys. Chem. B* 117 (2013), pp. 8659–8672.

[126] L. MicroCal. *ITC Data Analysis in Origin. Tutorial Guide*. 7.0. 2004.

[127] B. Hammouda. *Probing Nanoscale Structures – The SANS Toolbox*. National Institute of Standards and Technology Center for Neutron Research. 2010. URL: `http://www.ncnr.nist.gov/staff/hammouda/the_SANS_toolbox.pdf` (visited on 05/24/2014).

[128] J. Als-Nielsen and D. McMorrow. *Elements of Modern X-Ray Physics*. John Wiley & Sons Ltd, 2008.

[129] R.-J. Roe. *Methods of X-Ray and Neutron Scattering in Polymer Science*. Ed. by K. Binder et al. Oxford University Press, 2000.

[130] J. B. Hayter and J. Penfold. "An analytic structure factor for macroion solutions". *Mol. Phys.* 42 (1981), pp. 109–188.

[131] J. L. Lebowitz and J. K. Percus. "Mean Spherical Model for Lattice Gases with Extended Hard Cores and Continuum Fluids". *Phys. Rev.* 144 (1 1966), pp. 251–258.

[132] H. B. Stuhrmann and R. G. Kirste. "Elimination der intrapartikulären Untergrundstreuung bei der Röntgenkleinwinkelstreuung an kompakten Teilchen (Proteinen)". *Z. Phys. Chem.* 46 (1965), pp. 247–250.

[133] H. B. Stuhrmann. "Neutronenstreuung an Biopolymeren". *Chem. unserer Zeit* 13.1 (1979), pp. 11–22.

[134] P. Hickl and M. Ballauff. "Interpretation of the structural parameters derived from the analysis of polymer colloids by small-angle X-ray and neutron scattering". *Physica A* 235.1-2 (1997), pp. 238–247.

[135] D Pötschke et al. "Analysis of the structure of dendrimers in solution by small-angle neutron scatteing using contrast variation". *J. Appl. Cryst.* 33 (2000), pp. 605–608.

[136] C Sardet, a Tardieu, and V Luzzati. "Shape and size of bovine rhodopsin: a small-angle x-ray scattering study of a rhodopsin-detergent complex." *J. Mol. Biol.* 105.3 (1976), pp. 383–407.

[137] W. B. Turnbull and A. H. Daranas. "On the Value of c: Can Low Affinity Systems Be Studied by Isothermal Titration Calorimetry?" *J. Am. Chem. Soc.* 125.12 (2003), pp. 14859–14866.

[138] D. Lide. *CRC Handbook of Chemistry and Physics*. 90th. Taylor & Francis Ltd., 2009.

[139] K. Vogtt et al. "A new time-of-flight small-angle scattering instrument at the Helmholtz-Zentrum Berlin: V16/VSANS". *J. Appl. Crystallogr.* 47.1 (2014), pp. 237–244.

[140] P. Lindner and R. Schweins. "The D11 Small-Angle Scattering Instrument: A New Benchmark for SANS". *Neutron News* 21.2 (2010), pp. 15–18.

[141] A. Radulescu. *KWS2*. URL: `http://www.mlz-garching.de/instrumente-und-labore.html` (visited on 02/24/2014).

[142] P. Lindner and R. Schweins. *D11*. URL: `https://www.ill.eu/instruments-support/instruments-groups/?MH=1` (visited on 10/11/2013).

[143] K. Clemens Daniel; Vogtt. *V16*. URL: `http://www.helmholtz-berlin.de/quellen/ber/instruments-neutrons/index{\_}en.html` (visited on 08/15/2013).

[144] A.-J. Dianoux et al. *Neutron Data Booklet*. Ed. by A.-J. Dianoux and G. Lander. 2nd ed. 12. Institute Laue-Langevin, 2003, S1–S19.

[145] U. Keiderling and A. Wiedenmann. "New SANS instrument at the BER II reactor in Berlin, Germany". *Physica B: Physics of Condensed Matter* 213-214.C (1995), pp. 895–897.

[146] R. E. Ghosh, S. U. Egelhaaf, and A. R. Rennie. *A computing guide for small-angle scattering experiments*. 1989.

[147] A. Brûlet et al. "Improvement of data treatment in small-angle neutron scattering". *J. Appl. Crystallogr.* 40.1 (2007), pp. 165–177.

[148] O. Arnold et al. "Mantid—Data analysis and visualization package for neutron scattering and μ SR experiments". *Nuclear Instruments and Methods in Physics Research Section A: Accelerators, Spectrometers, Detectors and Associated Equipment* 764 (2014), pp. 156–166.

[149] S. Yu et al. "Interaction of human serum albumin with short polyelectrolytes: a study by calorimetry and computer simulations". *Soft Matter* 11.23 (2015), pp. 4630–4639. License Open Access CC-BY.

[150] B. Hess et al. "GROMACS 4: Algorithms for Highly Efficient, Load-Balanced, and Scalable Molecular Simulation". *J. Chem. Theory Comput.* 4.3 (2008), pp. 435–447.

[151] H. Lammert, A. Schug, and J. N. Onuchic. "Robustness and generalization of structure-based models for protein folding and function". *Proteins: Struct., Funct., Bioinf.* 77 (2009), pp. 881–891.

[152] M. Lund and P. Jungwirth. "Patchy proteins, anions and the Hofmeister series". *J. Phys.: Condensed Matter* 20 (2008), p. 494218.

[153] M. Wardell et al. "The atomic structure of human methemalbumin at 1.9 A." *Biochem. Biophys. Res. Commun.* 291.4 (2002), pp. 813–9.

[154] J. K. Noel et al. "SMOG@ctbp: simplified deployment of structure-based models in GROMACS". *Nucleic Acid Res.* 38 (2010), W657–661.

[155] C. Clement, H. Nymeyer, and J. N. Onuchic. "Topological and energetic factors: what determines the structural details of the transition state ensemble and "en-route" intermediates for protein folding? an investigation for small globular proteins". *J. Mol. Biol.* 298.5 (2000), pp. 937–953.

[156] D. L. Ermak and J. A. McCammon. "Brownian Dynamics with Hydrodynamic Interactions". *J. Chem. Phys.* 69 (1978), pp. 1352–1360.

[157] B. Isralewitz et al. "Steered molecular dynamics investigations of protein function". *J. Mol. Graph. Model.* 19.1 (2001), pp. 13–25.

[158] M. K. Gilson and H.-X. Zhou. "Calculation of protein-ligand binding affinities". *Annu. Rev. Biophys. Biomol. Struct.* 36 (2007), pp. 21–42.

[159] N. Welsch et al. "Core–shell microgels as "smart" carriers for enzymes". *Soft Matter* 8.5 (2012), p. 1428.

[160] J. E. Ladbury and B. Z. Chowdhry. "Thermodynamics of Protein-ligand interactions: History, Presence, and Future Aspects". *Chemistry & Biology* 3.10 (1996), pp. 791–801.

[161] L. S. Mizoue and J. Tellinghuisen. "Calorimetric vs . van' t Hoff binding enthalpies from Isothermal Titration Calorimetry : : Ba^{2+}-crown ether complexation". *Biophys. Chem.* 110.615 (2004), pp. 15–24.

[162] J. B. Chaires. "Calorimetry and thermodynamics in drug design". *Annu. Rev. Biophys.* 37 (2008), pp. 135–151.

[163] J. R. Horn et al. "Van't Hoff and calorimetric enthalpies from isothermal titration calorimetry: Are there significant discrepancies?" *Biochemistry (Mosc.)* 40.6 (2001), pp. 1774–1778.

[164] J. R. Horn, J. F. Brandts, and K. P. Murphy. "Van't Hoff and calorimetric enthalpies II: Effects of linked equilibria". *Biochemistry (Mosc.)* 41.23 (2002), pp. 7501–7507.

[165] S. G. Krimmer and G. Klebe. "Thermodynamics of protein-ligand interactions as a reference for computational analysis: How to assess accuracy, reliability and relevance of experimental data". *J. Comput.-Aided Mol. Des.* 29.9 (2015), pp. 867–883.

[166] A. Niedzwiecka et al. "Positive heat capacity change upon specific binding of translation initiation factor eIF4E to mRNA 5' cap". *Biochemistry (Mosc.)* 41.40 (2002), pp. 12140–12148.

[167] M. V. Petoukhov. *ATSAS*. EMBL. URL: `https://www.embl-hamburg.de/biosaxs/software.html` (visited on 09/22/2013).

[168] F Zhang et al. "Hydration and interactions in protein solutions containing concentrated electrolytes studied by small-angle scattering." *PCCP* 14.7 (2012), pp. 2483–93.

[169] *PDB Databank*. URL: `http://www.rcsb.org/pdb/home/home.do` (visited on 01/22/2014).

[170] M. V. Petoukhov et al. "New developments in the ATSAS program package for small-angle scattering data analysis". *J. Appl. Crystallogr.* 45.2 (2012), pp. 342–350.

[171] D. I. Svergun. "Determination of the regularization parameter in indirect-transform methods using perceptual criteria". *J. Appl. Crystallogr.* 25.4 (1992), pp. 495–503.

[172] D. I. Svergun. "Restoring low resolution structure of biological macromolecules from solution scattering using simulated annealing." *Biophys. J.* 76.6 (1999), pp. 2879–86.

[173] D. I. Svergun et al. "Protein hydration in solution: experimental observation by x-ray and neutron scattering." *Proc. Natl. Acad. Sci. U.S.A.* 95.5 (1998), pp. 2267–2272.

[174] J. Rescic et al. "Osmotic Pressure, Small-Angle X-Ray, and Dynamic Light Scattering Studies of Human Serum Albumin in Aqueous Solutions." *J. Colloid Interface Sci.* 239.1 (2001), pp. 49–57.

[175] J. R. Lu. "Neutron reflection study of globular protein adsorption at planar interfaces". *Ann. Reports C (Phys. Chem.)* 95 (1999), p. 3.

[176] D. Myatt and L. Clifton. *Protein Scattering Length Density Calculator v1.0*. Science and Technology Facilities Council. URL: `http://psldc.isis.rl.ac.uk/Psldc/licence.html` (visited on 02/11/2014).

[177] D. Kienzle Paul; Brown. NIST. 2013. URL: `https://www.ncnr.nist.gov/resources/activation/`.

[178] P. Lee and X. Wu. "Review: Modifications of Human Serum Albumin and Their Binding Effect". *Curr. Pharm. Des.* 21 (2015), pp. 1862–1865.

[179] H Matsuoka, D Schwahn, and N Ise. "Observation of cluster formation in polyelectrolyte solutions by small-angle neutron scattering. 1. A steep upturn of the scattering curves from solutions of sodium poly(styrenesulfonate) at scattering vectors below 0.01 .ANG.-1". *Macromolecules* 24.14 (1991), pp. 4227–4228.

[180] E. Ahmad et al. "Stereo-selectivity of human serum albumin to enantiomeric and isoelectronic pollutants dissected by spectroscopy, calorimetry and bioinformatics". *PLoS One* 6.11 (2011).

[181] S. Yu et al. "Interaction of human serum albumin with uremic toxins: A thermodynamic study". *RSC Advances* 7.45 (2017), pp. 27913–27922. License Open Access CC-BY.

[182] P. Debye and E. Hückel. "Thermodynamics and kinetics for the biological sciences". *Phys. Z.* 24 (1923), pp. 185–206.

[183] M. B. Jackson. *Molecular and Cellular Biophysics*. Cambridge University Press, 2006.

[184] G. G. Hammes. *Thermodynamics and kinetics for the biological sciences*. Wiley-Interscience, John Wiley & Sons. Inc., 2000.

[185] A. Luik et al. "Study of human serum albumin structure by dynamic light scattering: two types of reactions under different pH and interaction with physiologically active compounds". *Spectrochim. Acta. A. Mol. Biomol. Spectrosc.* 54.10 (1998), pp. 1503–1507.

[186] M. A. Kiselev et al. "Size of a human serum albumin molecule in solution." *Biofizika* 46 (2001), pp. 423–427.

[187] H. Boroudjerdi et al. *Phys. Rep.* 416 (2015), p. 129.

[188] N. Hoffmann, C. N. Likos, and J.-P. Hansen. "Linear screening of the electrostatic potential around spherical particles with non-spherical charge patterns". *Mol. Phys.* 102 (2004), pp. 857–867.

[189] I. Kalcher and J. Dzubiella. "Structure - thermodynamics relation of electrolyte solutions ". *J. Chem. Phys.* 130 (2009), p. 134507.

[190] J. Dzubiella. "Salt-specific stability and denaturation of a short salt-bridge forming alpha-helix". *J. Am. Chem. Soc,* 130 (2008), p. 14000.

[191] J. M. Scholtz et al. "The energetics of ion-pair and hydrogen-bonding interactions in a helical peptide". *Biochemistry (Mosc.)* 32 (1993), pp. 9668–9676.

[192] P. Setny, R. Baron, and J. A. Mccammon. "How can hydrophobic association be enthalpy-driven?" *J. Chem. Theory Comput.* 6 (2010), pp. 2866–2871.

[193] R. S. Spolar, J. H. Ha, and M. T. Record. "Hydrophobic effect in protein folding and other noncovalent processes involving proteins". *Proc. Natl. Acad. Sci. (USA)* 86 (1989), p. 8382.

[194] C. Tanford. *The hydrophobic effect: formation of micelles and biological membranes*. Wiley, 1973.

[195] G. Hummer. "Molecular binding: Under water's influence". *Nat. Chem.* 2 (2010), p. 906.

[196] J. Dzubiella. "How Interface Geometry Dictates Water's Thermodynamic Signature in Hydrophobic Association". *J. Stat. Phys.* 145 (2011), p. 227.

[197] F. Biedermann, W. M. Nau, and H.-J. Schneider. "The Hydrophobic Effect Revisited - Studies with Supramolecular Complexes Imply High-Energy Water as a Noncovalent Driving Force". *Angew Chem (Int Ed)* 53 (2014), pp. 11158–11171.

[198] B. Breiten et al. "Water Networks Contribute to Enthalpy/Entropy Compensation in Protein–Ligand Binding". *J. Am. Chem. Soc.* 135 (2013), pp. 15579–15584.

[199] L. Movileanu and E. A. Schiff. "Entropy-enthalpy Compensation of Biomolecular Systems in Aqueous Phase: a Dry Perspective". *NIH Public Access* 144.1 (2013), pp. 59–65.

[200] M. Kabiri and L. D. Unsworth. "Application of Isothermal Titration Calorimetry for Characterizing Thermodynamic Parameters of Biomolecular Interactions: Peptide Self-Assembly and Protein Adsorption Case Studies". *Biomacromolecules* 15 (2014), pp. 3463–3473.

[201] L. Kollipara and R. P. Zahedi. "Protein carbamylation: In vivo modification or in vitro artefact?" *Proteomics* 13.6 (2013), pp. 941–944.

[202] H. Qian. "Entropy-enthalpy compensation: Conformational fluctuation and induced-fit". *The Journal of Chemical Physics* 109.22 (1998), p. 10015.

[203] V. Lafont et al. "Compensating Enthalpic and Entropic Changes Hinder Binding Affinity Optimization". *Chemical Biology & Drug Design* 69.6 (2007), pp. 413–422.

Acknowledgments

To begin with, I would like to thank my supervisor Prof. Dr. Matthias Ballauff for giving me the opportunity to work on an interesting and challenging topic, for his continuous guidance, constant support, professionalism and fruitful discussions throughout the years of my PhD work. I am thankful for the freedom he gave me to pursue different aspects of my research and the possibility to attend interesting national and international conferences.
I owe special thanks to Prof. Joachim Dzubiella and Xiao Xu for the great collaboration on the theoretical part of my subject and for the time they spend on fruitful discussions which led to the successful publication of our joint study.
I am also grateful to our collaborators at the Charité, Prof. Dr. Walter Zidek, Prof. Dr. Joachim Jankowski, Prof. Dr. Markus van der Giet, Dr. Mirjam Schuchardt and Dr. Markus Tölle for the interesting ideas and fruitful project discussions. I am especially grateful for the patience Mijram showed me in explaining medical backgrounds.
I am truly grateful to Dr. Albrecht Petzold for his valuable support during my neutron beam-times and for sharing his expertise and wisdom on small-angle scattering with me. I am also thankful for the great discussions on this area with Dr. Günter Görigk, Dr. Daniel Clemens, who supported my experiments at the V16 at HZB, Dr. Annegret Günther and Dr. Miriam Siebenbürger for inspiring discussions on SANS and the instrumentation.
I am also indebted to the financial support from the Helmholtz-Zentrum Berlin and the Helmholtz Virtual Institute (HVI).
I would like to thank my (former) colleagues Qidi, Gregor, Andreas, Karol, and Katja, not only for the interesting scientific discussions but also for their friendship and the joyful time we spend during these past years. Of course I owe thanks to all other colleagues at the Institute of Soft Matter and Functional Materials for a great working environment and support beyond professional matters.
Last but not least, I sincerely thank my parents for their support, trust, love and faith in me, who gave me strength and motivation in times needed throughout the last years. Thank you Ben for being supportive, patient and loving when I felt stressed, always comforting and encouraging me. Thank you Evelyn and Annegret for being very dear friends to me in any situations of the last few years.

Selbstständigkeitserklärung

Hiermit versichere ich, dass ich die vorliegende Dissertation selbstständig verfasst und keine anderen als die angegebenen Quellen und Hilfsmittel verwendet habe.

Ferner erkläre ich, dass ich nicht anderweitig mit oder ohne Erfolg versucht habe, eine Dissertation einzureichen oder mich einer Doktorprüfung zu unterziehen.

Datum, Ort	Shun Yu